NUMERICAL MODELING OF OXY-COMBUSTION OF LIQUID FUEL IN THE FURNACE OF A WATER-TUBE BOILER

BY

BINASH IMTEYAZ

A Thesis Presented to the

DEANSHIP OF GRADUATE STUDIES

KING FAHD UNIVERSITY OF PETROLEUM & MINERALS

DHAHRAN, SAUDI ARABIA

In Partial Fulfillment of the
Requirements for the Degree of

MASTER OF SCIENCE

In

MECHANICAL ENGINEERING

NOVEMBER 2014

KING FAHD UNIVERSITY OF PETROLEUM & MINERALS

DHAHRAN- 31261, SAUDI ARABIA

DEANSHIP OF GRADUATE STUDIES

This thesis, written by **BINASH IMTEYAZ** under the direction his thesis advisor and approved by his thesis committee, has been presented and accepted by the Dean of Graduate Studies, in partial fulfillment of the requirements for the degree of **MASTER OF SCIENCE IN MECHANICAL ENGINEERING.**

Dr. M. A. HABIB
(Advisor)

Dr. Z. M. GASEM
Department Chairman

Dr. H. M. BADR
(Member)

Dr. Salam A. Zummo
Dean of Graduate Studies

Dr. ABDUL KHALIQ
(Member)

8/1/15
Date

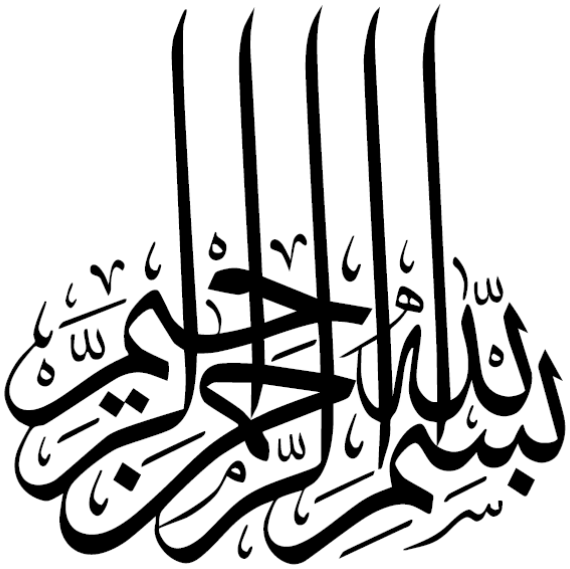

Dedicated to

My beloved mother and father, whose love, support and constant prayer brought to me all the success in my life.

ACKNOWLEDGMENTS

"In the name of Allah, the Beneficent, the Merciful"

All praise belongs to Almighty Allah (s.w.t.) for bestowing me with courage and perseverance to carry out this work sincerely. I thank Almighty Allah for giving me chance to do my M.S. successfully at King Fahd University of Petroleum and Minerals, Dhahran. I am happy to have had a chance to glorify His name in the sincerest way through this small accomplishment and ask Him to accept my efforts and facilitate me to serve His people with that which He has conferred on me.

My great thanks to King Fahd University of Petroleum and Minerals for providing me good academic platform and financial support during my M.S. Special thanks is also due to the KACST-TIC on CCS at KFUPM.

My deep gratitude and appreciation goes to my thesis advisor and mentor Dr. M.A. Habib for his constant guidance, motivation and support during the course of my studies. His valuable and priceless suggestions made this work interesting and challenging for me. I also wish to express my deep appreciation to Dr. Hassan M. Badr and Dr. Abdul Khaliq for their help, guidance, and constant encouragement during my M.S. I am greatly indebted to Dr. Rached Ben Mansour for the valuable time he spent throughout my thesis work and also for always being supportive and helping me during difficult times.

I am very grateful to Yasir Jamil, Furqan Tahir, Ahmer Ali and Maimoon Atif for their help and encouragement during my Masters. Also special thanks to Dr. Medhat A. Nemitallah for his support. I would also like to acknowledge all the Mechanical

Engineering faculty members with whom I took courses during my M.S., who helped me a lot during my coursework. I also owe thanks to all the students and faculty with whom I interacted during my Master's program.

TABLE OF CONTENTS

ACKNOWLEDGMENTS iv

TABLE OF CONTENTS vi

LIST OF TABLES ix

LIST OF FIGURES x

ABSTRACT xvii

ABSTRACT (ARABIC) xix

CHAPTER 1 INTRODUCTION 1

1.1 Research Background 1

1.2 Carbon Capture and Sequestration (CCS) Technologies 4

1.2.1 Pre-combustion 4

1.2.2 Oxy-fuel Combustion 5

1.2.3 Post Combustion 6

1.3 Problem Statement 7

1.4 Objectives 9

1.5 Thesis Outline 9

CHAPTER 2 LITERATURE REVIEW 12

2.1 Experimental Work on Evaporation of Liquid Fuel 12

2.2 Numerical Studies on Evaporation 13

2.3 Experimental Works on Combustion of Fuel-droplets 14
2.4 Numerical Studies on Combustion of Fuel droplets 17
2.5 Oxy-combustion 19
CHAPTER 3 MATHEMATICAL MODELING 23
3.1 Model Development 23
3.1.1 Reactor Design, Boundary and Inlet Conditions 23
3.1.2 General Conservation Equations 24
3.1.3 Turbulence-chemistry Interaction 25
3.1.4 Discrete Phase Model 31
3.1.5 Radiation Model 34
3.1.6 Soot Model 35
3.2 Numerical Study 37
3.2.1 Problem Definition & Solution Procedure 37
3.2.2 Validation of the Numerical Model with Experimental Data 39
CHAPTER 4 RESULTS AND DISCUSSION 43
4.1 Ethanol Combustion in a Vertical Reactor 43
4.1.1 Choice of Turbulence Model 43
4.1.2 Effect of Dilution of Oxidizer Stream with Carbon Dioxide 48
4.1.3 Effect of Soot on Radiation 55
4.2 Heavy Fuel Oil Combustion in the Boiler 58

4.2.1 Effect of Dilution of the Oxidizer with Carbon dioxide 58

4.2.2 Effect of Droplet Size on the Combustion Characteristics 107

4.2.3 Effect of Swirl Number on the Combustion Characteristics..... 110

CHAPTER 5 CONCLUSIONS AND RECOMMENDATIONS 117

5.1 Oxy-combustion of Ethanol in a Vertical Reactor 117

5.2 Liquid Fuel Oxy-combustion in the Furnace of a Water Tube Boiler 118

5.3 Recommendations 119

NOMENCLATURE..... 121

REFERENCES..... 123

VITAE..... 135

LIST OF TABLES

Table 1. Composition of the liquid fuel **8**

Table 2. Injector Characteristics **40**

LIST OF FIGURES

Figure 1. Average Global Temperature has risen more than 1.4 ^{o}F (0.8^{o}C) over the last century [2]..... 1

Figure 2. Global Average Absolute Sea level has risen by an alarming magnitude of 9 inches from 1870-2008 [3] 2

Figure 3. Relative percentage of greenhouse gases [4]..... 2

Figure 4. Schematic of Pre-combustion technique [10]..... 4

Figure 5. Schematic of Oxy-combustion technique [10] 5

Figure 6. Schematic of Oxy-combustion technique [10] 6

Figure 7. Geometry of the water tube boiler 8

Figure 8. Graphical representation of Probability Density Function 30

Figure 9. Schematic view of Experimental setup used by Francois et.al. 38

Figure 10. Schematic diagram of the vertical reactor and the injector 38

Figure 11. Comparison between the experimental [29] flame shapes captured at steady state conditions (A, B, C, D and E) and the corresponding calculated flame shapes using the temperature (K) contours (a, b, c, d, and e) under different mass fractions of oxygen in the oxidzer mixture..... 41

Figure 12. Comparison between experimental [29] and numerical radial temperature profiles at different heights inside the reactor including (a) 32 cm, (b) 47 cm and (c) 62 cm under pure oxy-combustion conditions (100% O_2). 42

Figure 13. Comparison of radial temperature profile using RKE model and RSM model with the experimental data at the height of 32 cm..... 44

Figure 14. Comparison between the RKE and the RSM models in terms of (a) axial temperature profile, and (b) axial oxygen mass fraction distribution, calculated through the reactor centreline for the case of OF29. 45

Figure 15. Comparison between the RKE and the RSM models in terms of (a) axial turbulent intensity profile, and (b) axial specific thermal capacity distribution, calculated through the reactor centreline for the case of OF29. 47

Figure 16. Comparison between the temperature (K) contours for the three cases including air, OF21, and OF29. 49

Figure 17. Comparison between the total velocity (m/s) contours for the three cases including air, OF21, and OF29. 50

Figure 18. Comparison between the combustion characteristics in terms of (a) combustion temperature through the reactor centreline, and (b) absorbed radiant heat by the reactor wall through the reactor height, for the three cases including air, OF21, and OF29. 52

Figure 19. Comparison between the mass fractions distribution through the reactor centreline of (a) ethanol, and (b) oxygen, for the three cases including air, OF21, and OF29. 53

Figure 20. Distributions of (a) turbulence intensity, and (b) specific thermal capacity along the reactor centreline for different combustion cases including air, OF21, and OF29. 54

Figure 21. Comparison between the combustion characteristics in terms of (a) combustion temperature through the reactor centreline, and (b) absorbed

radiant heat by the reactor wall through the reactor height, for OF29 with soot model and without soot model 56

Figure 22. Comparison of soot mass fraction along centreline of the reactor for air case, OF 21 case and OF 29 case. 57

Figure 23. Temperature distribution along the axis of burner 1 (z=2.198 m)..... 61

Figure 24. Temperature distribution along the axis of burner 2 (z=4.662 m)..... 61

Figure 25. Temperature (K) contours for horizontal plane at z=2.198 m 62

Figure 26. Temperature (K) contours for horizontal plane at z=4.662 m 63

Figure 27. Temperature (K) contours for vertical plane at y=-2.24 m..... 64

Figure 28. Temperature (K) contours for vertical plane at x=2.24 m 65

Figure 29. Trajectory of droplets with diameter (in m) 66

Figure 30. Velocity along the axis of burner 1 (z=2.198 m)..... 68

Figure 31. Velocity along the axis of burner 2 (z=4.662 m)..... 68

Figure 32. Velocity (m/s) contours for vertical plane at y=-2.24 m 69

Figure 33. Turbulent Intensity along the axis of burner 1 (z=2.198 m)..... 71

Figure 34. Turbulent Intensity along the axis of burner 2 (z=4.662 m)..... 71

Figure 35. Turbulent intensity (%) contours for vertical plane at y=-2.24 m 72

Figure 36. Turbulent Viscosity along the axis of burner 1 (z=2.198 m)..... 74

Figure 37. Turbulent Viscosity along the axis of burner 2 (z=4.662 m)..... 74

Figure 38. Turbulent viscosity (kg/m-s) contours for vertical plane at y=-2.24 m..... 75

Figure 39. Specific thermal capacity along the axis of burner 1 (z=2.198 m)..... 77

Figure 40. Specific thermal capacity along the axis of burner 2 (z=4.662 m)..... 77

Figure 41. Mass fraction of C_6H_6 along the axis of burner 1 (z=2.198 m) 79

Figure 42. Mass fraction of C_6H_6 along the axis of burner 2 (z=4.662 m) 79

Figure 43. Mass fraction of C_6H_6 for vertical plane at y=-2.24 m 80

Figure 44. Mass fraction of CH_4 along the axis of burner 1 (z=2.198 m) 81

Figure 45. Mass fraction of CH_4 along the axis of burner 2 (z=4.662 m) 81

Figure 46. Mass fraction of CH_4 for vertical plane at y=-2.24 m 82

Figure 47. Mass fraction of C_2H_4 along the axis of burner 1 (z=2.198 m) 83

Figure 48. Mass fraction of C_2H_4 along the axis of burner 2 (z=4.662 m) 83

Figure 49. Mass fraction of C_2H_4 for vertical plane at y=-2.24 m 84

Figure 50. Mass fraction of CO along the axis of burner 1 (z=2.198 m) 86

Figure 51. Mass fraction of CO along the axis of burner 2 (z=4.662 m) 86

Figure 52. Mass fraction of CO for vertical plane at y=-2.24 m 87

Figure 53. Mass fraction of hydrogen along the axis of burner 1 (z=2.198 m) 88

Figure 54. Mass fraction of hydrogen along the axis of burner 2 (z=4.662 m) 88

Figure 55. Mass fraction of hydrogen for vertical plane at y=-2.24 m 89

Figure 56. Mass fraction of H_2O along the axis of burner 1 (z=2.198 m) 92

Figure 57. Mass fraction of H_2O along the axis of burner 2 (z=4.662 m) 92

Figure 58. Mass fraction of H_2O for vertical plane at y=-2.24 m 93

Figure 59. Mass fraction of OH along the axis of burner 1 (z=2.198 m) 94

Figure 60. Mass fraction of OH along the axis of burner 2 (z=4.662 m) 94

Figure 61. Mass fraction of OH for vertical plane at y=-2.24 m 95

Figure 62. Mass fraction of oxygen along the axis of burner 1 (z=2.198 m) 96

Figure 63. Mass fraction of oxygen along the axis of burner 2 (z=4.662 m) 96

Figure 64. Mass fraction of oxygen for vertical plane at y=-2.24 m 97

Figure 65. Mole fraction of soot along the axis of burner 1 (z=2.198 m)..... 99

Figure 66. Mole fraction of soot along the axis of burner 2 (z=4.662 m)..... 99

Figure 67. Mole fraction of soot for vertical plane at y=-2.24 m 100

Figure 68. Distribution of total heat transfer rate (kW) along the furnace top 103

Figure 69. Distribution of radiation heat transfer rate (kW) along the furnace top 103

Figure 70. Distribution of total heat transfer rate (kW) along the side wall (left) 104

Figure 71. Distribution of radiation heat transfer rate (kW) along the side wall (right). 104

Figure 72. Distribution of total heat transfer rate (kW) along the side wall (left) 105

Figure 73. Distribution of radiation heat transfer rate (kW) along the side wall (right). 105

Figure 74. Distribution of total heat transfer rate (kW) along the boiler tube bank 106

Figure 75. Distribution of radiation heat transfer rate (kW) along the boiler tube bank 106

Figure 76. Temperature (K) contours for the vertical pane at y=-2.24 m..... 108

Figure 77. Temperature distribution along the axis of burner 1 (z=2.198 m)..... 109

Figure 78. Temperature distribution along the axis of burner 2 (z=4.662 m)..... 109

Figure 79. Temperature (K) contours for vertical pane at y=-2.24 m..... 112

Figure 80. Temperature distribution along the axis of burner 1 (z=2.198 m)..... 113

Figure 81. Temperature distribution along the axis of burner 2 (z=4.662 m)..... 113

Figure 82. Temperature (K) contours for horizontal plane at z=4.662 m..... 114

Figure 83. Turbulent viscosity (kg/m-s) contours for the vertical plane at y = 2.24 m .. 115

Figure 84. Distribution of total heat transfer rate (kW) along the boiler tube bank 116

Figure 85. Distribution of radiation heat transfer rate (kW) along the boiler tube bank 116

LIST OF ABBREVIATIONS

ANN	Artificial Neural Network
CCS	Carbon Capture and Sequestration
CTM	Continuous Thermodynamics
DM	Discrete Multicomponent
DO	Discreet Ordinates
EDM	Eddy Dissipation Model
EGR	Exhaust Gas Recirculation
ER	Equivalence Ratio
FSM	Full Second-order moment
GA	Genetic Algorithm
IGCC	Integrated Gasification Combined Cycle
MEA	Monoethanolamine
MILD	Moderate or Intense Low-oxygen Dilution
MOF	Metal Organic Framework
OF21	Mixture of 21% O_2 and 79% CO_2 by volume
OF29	Mixture of 29% O_2 and 71% CO_2 by volume
PDF	Probability Density Function
PPF	Partially Premixed Flame
RKE	Realizable k-ε model
RNG	Renormalization Group k-ε model

RSM	Reynolds Stress model
RTE	Radiative transfer equation
SIMPLE	Semi-Implicit Method for Pressure-Linked Equations
SKE	Standard k-ε model
SOFC	Solid Oxide Fuel Cell
TRI	Turbulence Radiation Interaction
WSGGM	Weighted Sum of Gray Gas Model

ABSTRACT

Full Name : Binash Imteyaz

Thesis Title : Numerical Modeling of Oxy-Combustion of Liquid Fuel in the Furnace of a Water-Tube Boiler

Major Field : Mechanical Engineering

Date of Degree : May 2014

With the ever rising concern of global warming, carbon capture is gaining the reputation of one of the most challenging fields of research. A very promising technology to capture CO_2 is oxy-combustion. Oxy-combustion offers several advantages over conventional combustion technologies, such as flue gas volume reduction, high combustion efficiency, low fuel consumption and significant reduction in NOx emissions. Liquid fuel is available and it is the most widely used source of energy in the world. Easy handling and transportation, less storage volume and higher flame temperature are some of the features of liquid fuels which give it an upper hand over other sources.

In this study, a computational fluid dynamics model (CFD) for liquid fuel combustion has been developed and validation of the model is performed through comparison with the available experimental data. Then, oxy-combustion of liquid fuel (C5-C6 mixture) in a typical water tube boiler is modelled numerically. Non-premixed model using Probability Density Function is incorporated to simulate the combustion of the liquid fuel droplets. Three cases with different oxidizer compositions have been modelled: (i) Air case (21 % of O_2 and 79 % of N_2 by volume), (ii) OF21 case (21 % of O_2 and 79 % of CO_2 by volume) (iii) OF29 (29 % of O_2 and 71 % of CO_2 ¬by volume). Influence of dilutions

with carbon dioxide, droplet size, soot formation and swirl number on the combustion characteristics has been studied. It was found that increase in the percentage of carbon dioxide in the combustion environment results in a reduction in the flame size and temperature. Heat transfer through the walls was also reduced because of non-uniform heat distribution and poor convection heat transfer in the carbon dioxide environment. However, soot formation is greatly reduced in carbon dioxide case in comparison to the air case. Size of the droplets was not of much importance for the case studied, however, swirl in the oxidizer stream enhances mixing and results in better combustion of the liquid fuel.

ملخص الرسالة

الاسم الكامل: بينش امتياز

عنوان الرسالة: نموذج حسابي لحرق الاكسجين للوقود السائل في افران الغلايات البخاريه

التخصص: هندسه ميكانيكيه

تاريخ الدرجة العلمية: نوفمبر 2014

تكتسب تكنولوجيا إلتقاط الكربون سمعة كواحدة من الحقول الأكثر تحديا من البحث وذلك بسبب الإهتمام المتزايد بظاهرة الاحتباس الحرارى. توجد هناك تكنولوجيا واعدة جدا لالتقاط ثانى أوكسيد الكربون وهي تكنولوجيا الحرق بالأوكسوجين. تقدم تكنولوجيا الحرق بالأوكسوجين العديد من المزايا على تقنيات الاحتراق التقليدية، مثل تخفيض حجم غاز العادم، وإرتفاع كفاءة الاحتراق، وانخفاض استهلاك الوقود وخفض كبير في انبعاثات أكاسيد النيتروجين. الوقود السائل متاح ويعتبر مصدر الطاقة الأكثر استخداما في العالم. يتميز الوقود السائل عن المصادر الأخرى للطاقة بسهولة التعامل والنقل، وقلة حجم التخزين وإرتفاع درجة حرارة اللهب.

في هذه الدراسة، تم تطوير نموذج حسابي (CFD) لإحتراق الوقود السائل وتم تنفيذ عملية المصادقة على النموذج من خلال المقارنة مع البيانات التجريبية المتوفرة. تم كذلك تعديل النموذج الحسابى ليكون صالح للإستخدام فى العملية الحسابية لعملية حرق وقود السائل يحتوى على 5 إلى 6 ذرات كربون بإستخدام الأوكسوجين فى الغلايات البخارية. تم إدراج نموذج للحرق على أساس عدم الخلط بين الأوكسوجين والوقود باستخدام دالة الكثافة الاحتمالية وذلك لمحاكاة عملية إحتراق قطرات الوقود السائل. تم عمل الحسابات الكودية لثلاث حالات مختلفة من حيث نسبة الأوكسوجين فى الغاز المؤكسد: (1) حالة الهواء، ويحتوى الغاز المؤكسد فى تلك الحالة على 21٪ أوكسوجين و 79٪ نيتروجين من حيث الحجم، (2) الحالة OF21 ، ويحتوى الغاز المؤكسد فى تلك الحالة على 21٪ أوكسوجين و 79٪ ثانى أوكسيد كربون من حيث الحجم (3) الحالةOF29 ، ويحتوى الغاز المؤكسد فى تلك الحالة على 29٪ أوكسوجين و 71٪ ثانى أوكسيد كربون من حيث الحجم. تمت دراسة آثار كل من التخفيفات مع ثاني أكسيد الكربون، وحجم القطرات، وتراكم الهباب على انتقال الحرارة وكذلك تم دراسة تأثير الدوامات على خصائص الاحتراق. وقد وجد أن الزيادة في نسبة ثاني أكسيد الكربون في بيئة الإحتراق يقلل من حجم اللهب والحرارة. حدث إنخفاض فى

كمية الحرارة المنتقلة عبر الجدران عند الحرق فى بيئة من ثاني أكسيد الكربون بسبب وجود عشوائية فى توزيع الحرارة وضعف عملية نقل الحرارة بالحمل. بالرغم من ذلك، انخفضت فرص تشكل الهباب إلى حد كبير في حالة الحرق فى بيئة من ثاني أكسيد الكربون بالمقارنة مع حالة الحرق فى بيئة من الهواء الجوى. لم يكن حجم القطرات ذا أهمية كبيرة فى الحالة تحت الدراسة، ومع ذلك، فإنه قد وجد تأثير كبير لدوامات الغاز المؤكسد على خلط واحتراق الوقود السائل.

CHAPTER 1

INTRODUCTION

1.1 Research Background

Our Earth is warming up. Over the past century increase in Earth's average temperature has been recorded as 1.40 F and is projected to rise further over the next hundred years. This small rise in average temperature of our earth is obvious and has detrimental effects on climate. Signs are appearing all over and we can observe melting of ice worldwide, especially in polar regions subsequently increasing sea level over the last century. Scientists predict that with melting of ice sheets of Greenland and Antarctica, sea level rise could be more than 20 feet by 2100 compared to the sea level of today [1]. With this

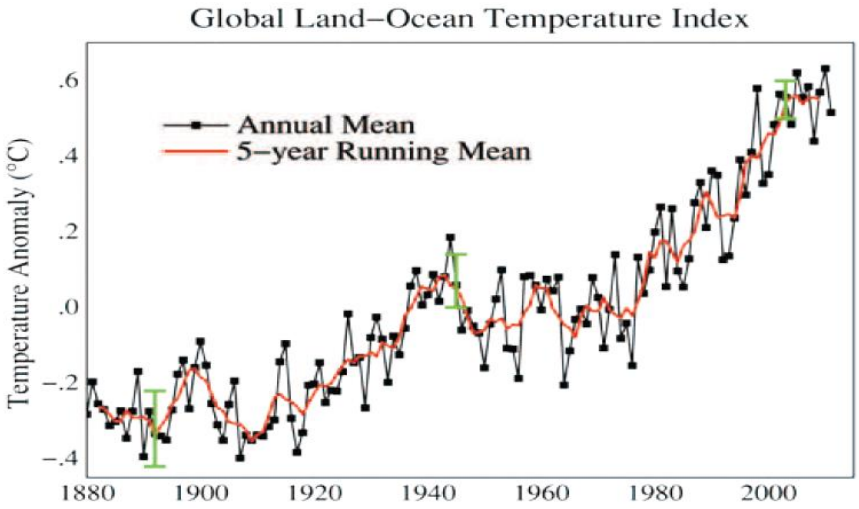

Figure 1. Average Global Temperature has risen more than 1.4 ^{o}F (0.8^{o}C) over the last century [2]

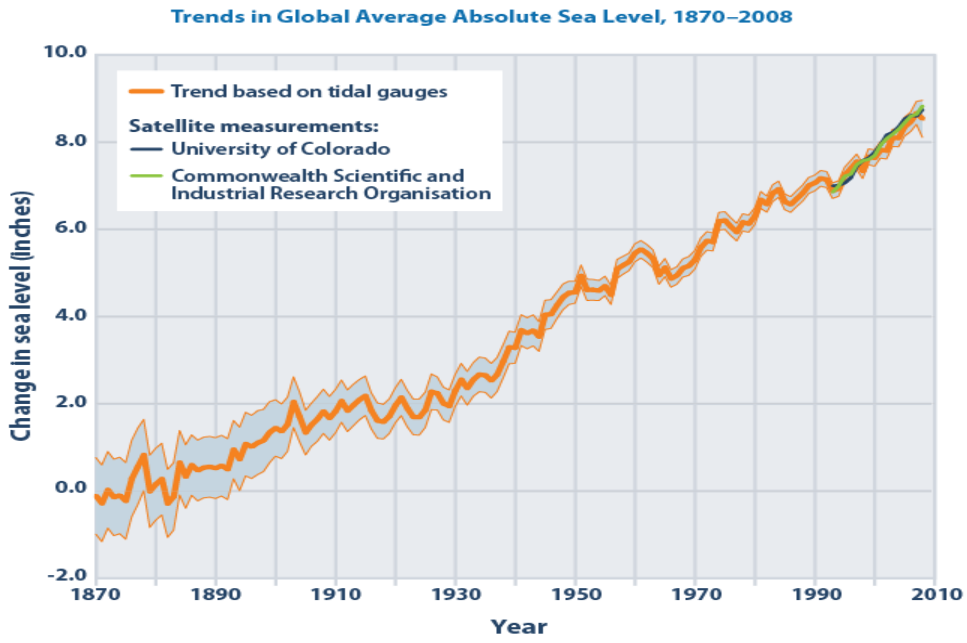

Figure 2. Global Average Absolute Sea level has risen by an alarming magnitude of 9 inches from 1870-2008 [3]

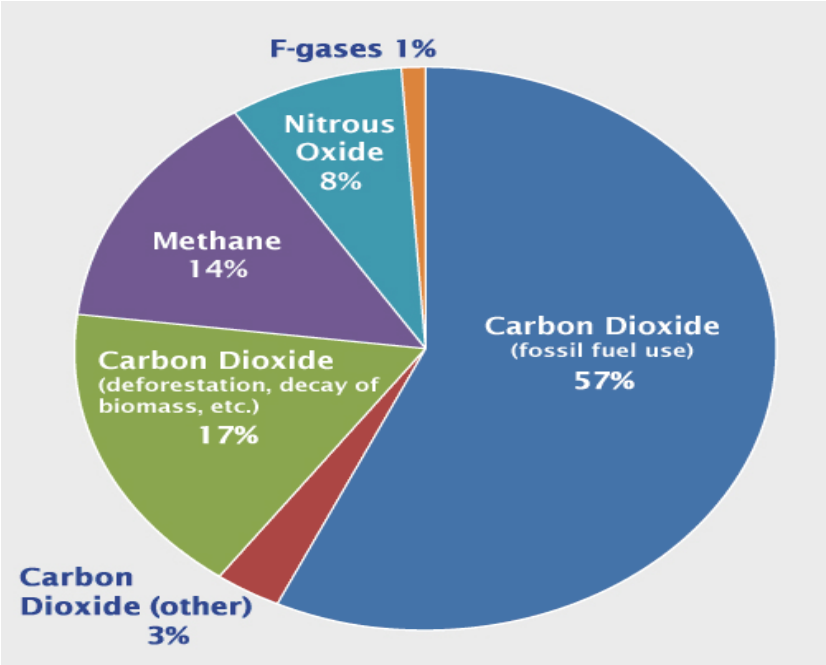

Figure 3. Relative percentage of greenhouse gases [4]

growing sea level, many low-laying and coastal communities are under threat of eradication.

Although concern on global climate changes grows, fossil fuels are still the major energy source in the world. The conversion of fossil fuels into energy is inevitably accompanied by a combustion process which, apart from useful heat, generates flue gases that are harmful both to humans and to the environment. With the ever-rising concern of Global warming, carbon capturing technologies are one of the most challenging fields of research of the millennium. It is predicted that the fossil fuels will continue to be the major source of energy for next decades [5]. As the basic source carbon dioxide is the use of fossil fuels & CO_2 contributes to around 77% of Global Green House emissions [1], there is an immediate need to redesign our industrial & power generation systems. CO_2 emissions levels are expected to rise by 70% by the years 2050 [6]. As fossil fuels continue to be the largest source of power production, carbon capturing technologies provide an essential tool to control the CO_2 emissions in the atmosphere. Thus, a comparatively quick and cost effective way to control the CO_2 emissions is to capture CO_2 from large point sources and subsequently store in the geological sites. Carbon capturing technologies can be grouped into three main categories: (i) Post combustion decarbonisation (ii) Oxy-fuel combustion & (iii) Pre-combustion decarbonisation. Efficiency of current power plants using CCS technology is around 35% [7], where the efficiency loss is of order 7-11% [8].

1.2 Carbon Capture and Sequestration (CCS) Technologies

1.2.1 Pre-combustion

In a pre-combustion system, decarbonisation is done prior to the combustion of the fuel. This techniques has already been used for the production of hydrogen in chemical and refining industries for more than five decades [9]. The first step is to process the fuel in presence of steam and air (or oxygen) to get carbon monoxide and hydrogen (synthesis gas). Carbon monoxide further reacts with the steam in another reactor (a 'shift' reactor) to form carbon dioxide and more hydrogen. The CO_2 is then separated from H_2 and pressurized for transport to a storage facility. Thus, a carbon free pure fuel (H_2) is obtained which can be used in a reactor or a turbine to get zero CO_2 emission power system. Pre-combustion can be employed with Integrated Gasification Combined Cycle (IGCC) plant, which uses natural gas and coal as fuels.

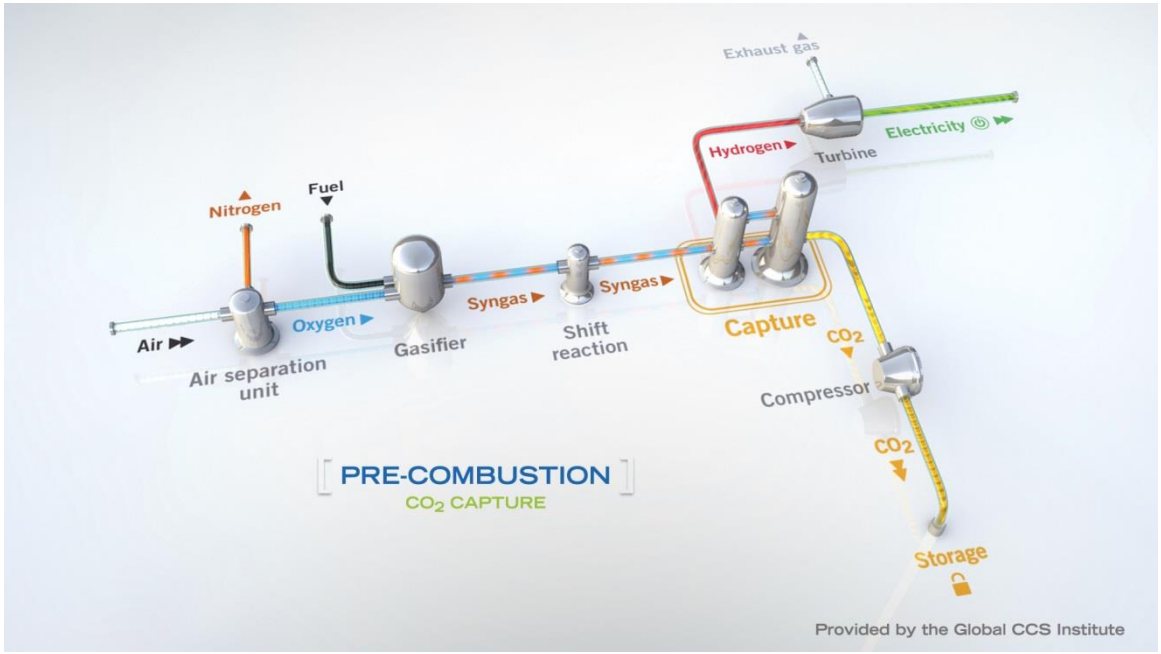

Figure 4. Schematic of Pre-combustion technique [10]

1.2.2 Oxy-fuel Combustion

In Oxy-combustion, oxygen is separated from the air prior to the combustion, using conventional cryogenic liquefaction processes or recently developed Ion Transport Membrane technique [11]. Pure Oxy-combustion leads to very high flame temperature, which is undesirable for the wall of the furnace. In, order to get rid of this complication a part of flue gases, which is basically carbon-dioxide and water vapour, is recirculated into the reactor to absorb excess heat. Unlike conventional air-fuel combustion, oxy-combustion provides a good means to control the flame temperature by just circulating the required amount of flue gas. Though separation of oxygen requires a modest amount of energy, studies shows that current technologies of oxy-fuel combustion is technically feasible [12].

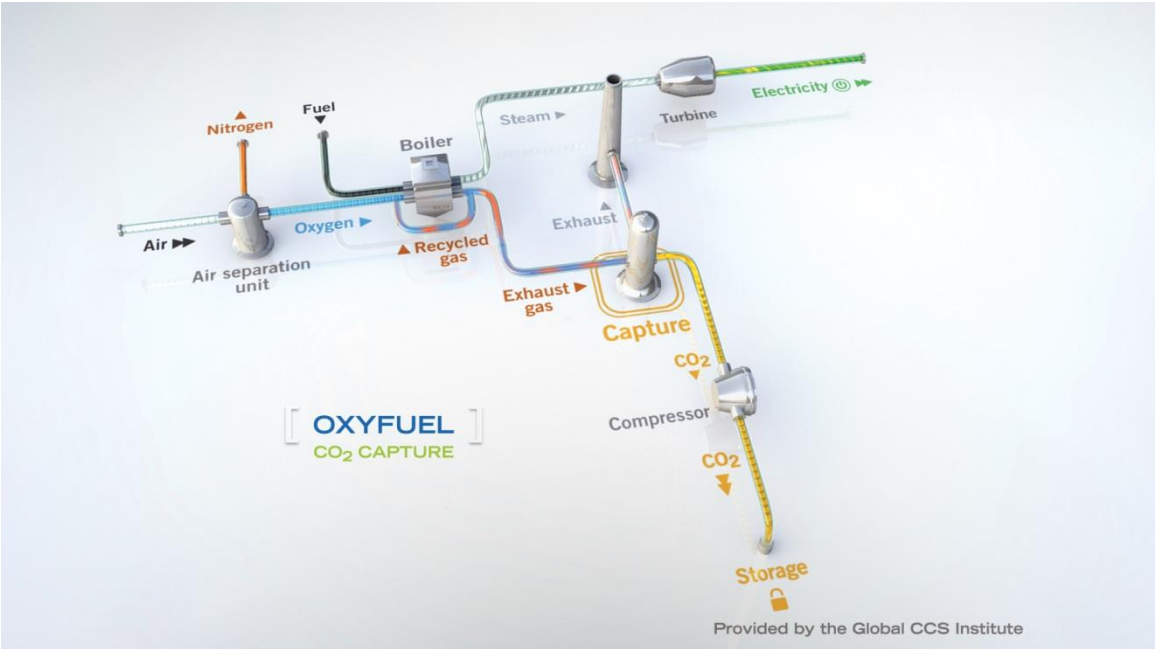

Figure 5. Schematic of Oxy-combustion technique [10]

1.2.3 Post Combustion

In this process, CO_2 is captured from the flue gases produced by the combustion of fuel in air. Liquid solvents, such as amines, are usually used to capture the fraction CO_2 from the flue gas stream. High percentage of oxides of nitrogen and sulphur in the flue gas, however, causes complications by forming stable and non-regenerable salts in reaction with amines. Thus, it is required that the plant should have facilities of upstream de-NO_x and Flue Gas desulfurization. Current post-combustion technology employs organic solvent such as monoethanolamine (MEA) for a modern pulverized coal power plant or a natural gas combined cycle power plant [9,13–15]. The regenerated solvent is recycled into the carbon capture process, resulting in a closed scrubbing cycle.

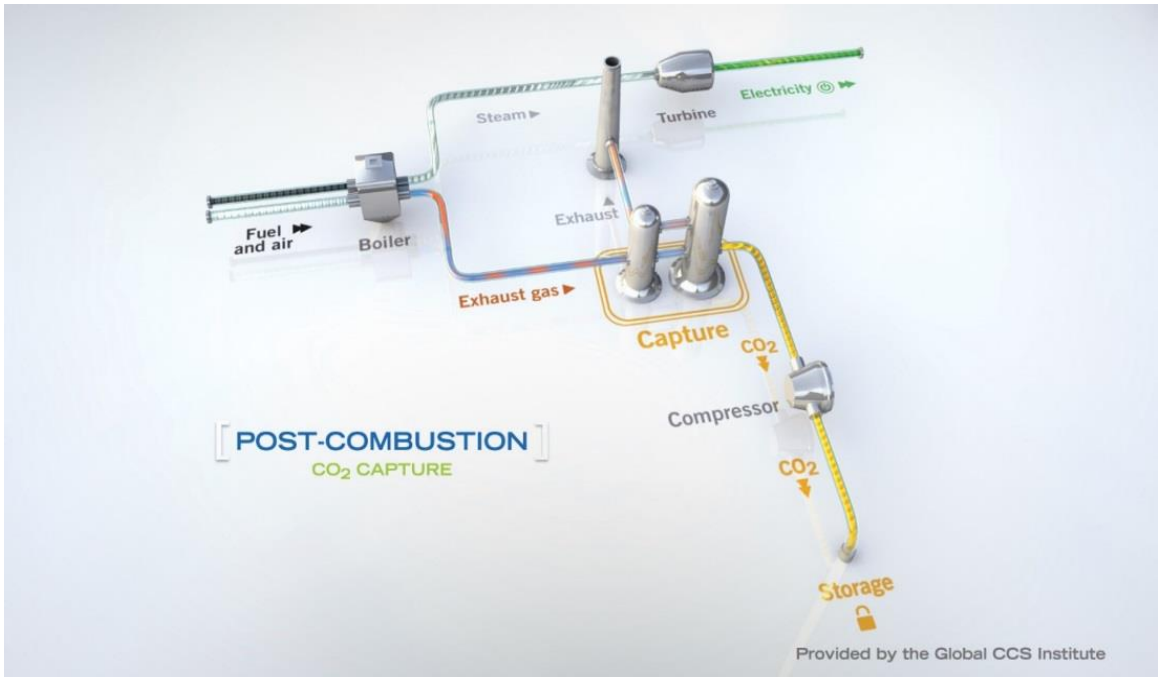

Figure 6. Schematic of Oxy-combustion technique [10]

In recent years, Metal Organic Frameworks (MOFs) have gained a good reputation in research fields as a promising post combustion carbon capturing technology [16]. MOFs are a new class of crystalline porous materials with great potential as adsorbents. MOFs with selective adsorbent properties are under research stage for capturing and separating CO_2 from the flue gases.

Basic advantage of post combustion technology is that it can be easily retrofitted into the existing plants, provided that there is enough room to install the capture system.

1.3 Problem Statement

Oxy-fuel combustion of liquid fuel is modeled numerically for the geometry of the water-tube boiler (Figure 7). The boiler has a length (x-axis) of 12.54 m, width (y-axis) of 6.865 m and height (z-axis) of 7.248 m. The boiler consists of two parts: (i) the furnace and (ii) the tube bank. The part forming the tube bank has a width of 2 m. There are two burners in the furnace at a distance of 2.24 m from the left wall at the height of 2.198 m & 4.662 m respectively. A set of water jackets runs from the top to the bottom of tube bank.

The boiler has a firing rate of 208 MW with a drum pressure of 50 atm and steam flow rate of 66.5 kg/s. A combination of primary air with swirl and secondary air is introduced at the room temperature from the annular inlet. Liquid fuel is injected at the room temperature from the nozzles. Carbon-dioxide is recirculated and introduced into the boiler along with the oxygen. Walls of the boiler are given constant temperature boundary condition with temperature of 538 K. Internal emissivity is given as 0.7.

Table 1. Composition of the liquid fuel

Type of fuel	Formula	Mole Percentage %
n-butane	C_4H_{10}	0.1
n-pentane	C_5H_{12}	37.7
iso-pentane	C_5H_{12}	23.0
n-hexane	C_6H_{14}	25.9
n-heptane	C_7H_{16}	8.6
n-octane	C_8H_{18}	4.1
n-nonane	C_9H_{20}	0.4
n-decane	$C_{10}H_{22}$	0.1
n-dodecane	$C_{12}H_{26}$	0.1
Total		**100**

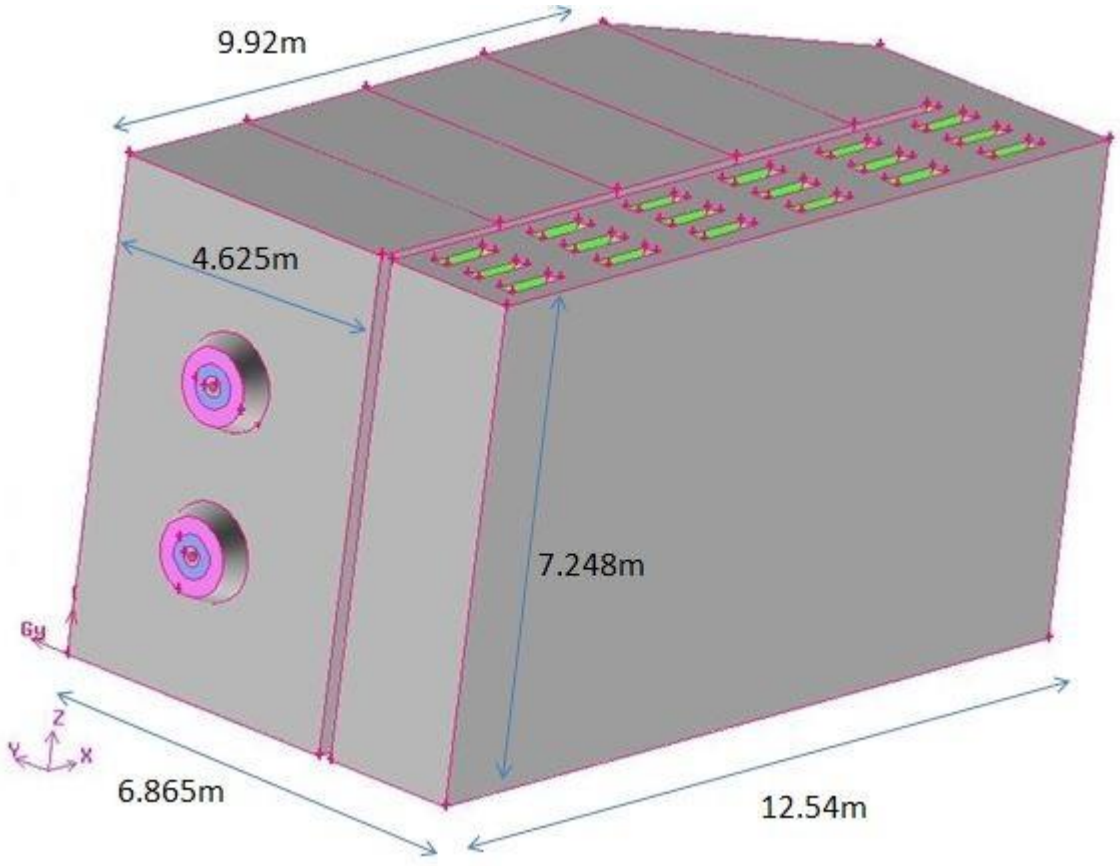

Figure 7. Geometry of the water tube boiler

1.4 Objectives

The objectives of this research are:

1. To develop a computational model to simulate the combustion of liquid fuel droplets in different oxidizer environments inside the furnace of a water-tube boiler.
2. To validate the liquid fuel combustion model with the experimental data available in previous research.
3. To predict the heat transfer from the burned gases to the water jacket along the different surfaces of the furnace.
4. To compare the combustion characteristics of the liquid fuel at different dilutions of carrier gas with the conventional air combustion case.
5. To study the effects of droplet size on the combustion characteristics.
6. To study the effects of swirl number on the liquid fuel combustion.

1.5 Thesis Outline

The objective of this thesis is to develop a numerical model to solve the combustion of liquid fuel droplets in a turbulent environment. The model is used to analyse the combustion characteristics of the fuel in oxygen-carbon dioxide environment and effects of the dilutions of the carrier gas is compared with that of the conventional air combustion case.

This thesis contains five chapters:

Chapter 1 introduces the threats of Global warming and various carbon capturing and sequestration technologies. The challenges and feasibility of oxy-combustion as a carbon capture tool is also discussed. The chapter further includes the problem specifications and defines the objectives of this thesis.

Chapter 2 discusses the prior researches conducted on liquid fuel evaporation, droplet combustion and oxy-combustion. Various experimental and numerical works are presented and analysed in this section.

Chapter 3 is divided into two parts: Model development and Numerical Study. The first part includes the descriptions of reactor design and boundary conditions applied to the geometry. Then, a brief summary of the governing equations and applied mathematical models has been discussed. The second part describes the problem definition of an experimental case. It further discusses the solution procedure and validation of the model with the experimental data.

Chapter 4 includes the results and discussion and is divided into two parts. The first part presents the combustion characteristics of ethanol in a vertical reactor. The study is extended to analyse the choice of turbulence model, effect of dilution and effect of soot on radiation in the combustion of ethanol. The second part presents the combustion

characteristics of heavy fuel oil in the furnace of a water tube boiler. Effect of dilution of oxidizer stream with the carrier gas, effect of droplet size and effect of swirl number on the combustion characteristics of the liquid fuel has been discussed.

Chapter 5 presents the conclusion of this study and provides the recommendations of possible future results.

CHAPTER 2

LITERATURE REVIEW

2.1 Experimental Work on Evaporation of Liquid Fuel

Li et. al. [17] investigated experimentally the droplet size distribution and evaporation characteristics of fuel spray by a swirl type atomizer. They utilized the Laser Diffraction technique to measure droplet size distribution. The spray outer zone was found to be exhibiting larger diameter than those in the inner zone which can be attributed to the effect of spray-induced ambient air flow. They also noticed a reduction in ambient pressure increases the air entrainment and droplet evaporation.

At low temperature, Ghassemi et. al. [18] found that the evaporation of kerosene droplets increases with increasing ambient pressure, but at high temperature they found a maximum rate of evaporation at 2.0 MPa and then it decreases again. The liquid droplet evaporation followed the d^2-Law after initial heating up process and the rate of evaporation increased monotonically with the temperature. They also found that the rate of evaporation reduces by increasing pressure at a temperature of 700 ^{o}C and above, due to the formation of a dense cloud around the droplet, inhibiting its evaporation.

The effect of surface conditions on evaporation of sprayed liquid droplet was studied by Negeed et. al. [19]. They used a high speed camera to capture the behaviour of droplets during the collision with hot surface. They found that the contact timing or the

evaporation timing decreases with increasing thermal conductivity of the surface and increases with increasing diameter of the droplets. The maximum droplet spread diameter was found to be increasing with increased droplet Weber number, droplet size & impinging velocity.

2.2 Numerical Studies on Evaporation

Abramzon and Sirignano [20] developed a new model of vaporization of a moving fuel droplet which takes account of non-unitary Lewis number in the gas phase, influence of Stefan flow on heat and mass transfer and the effect of the transient liquid heating inside the internally circulating droplet. This model is based on 1-D equation of convective heat transfer and predicts reasonably accurate results at comparatively less computational time in respect to 2-D extended liquid heating model. They also suggested that the proposed model is valid for a wide range of droplet sizes and Reynolds Number. Daif et al. [21] studied the vaporization of multicomponent fuel droplets utilizing model proposed by Abramzon and Srignano [20]. They found a good agreement between the experimental and predicted results using this model for natural convection as well as for forced convection. Evaporation and combustion of multicomponent fuel droplets was numerically modeled by Kitano et al. [22]. They utilized the discrete multicomponent (DM) method to model the evaporation, which assumes that each component evaporates individually from the surface according their volatility while the temperature and composition are uniform inside the droplet. Yasin et al. [23] also utilized DM model to predict the biodiesel spray combustion. They found that DM model is more successful in

predicting longer penetration length of biodiesel compared to that of diesel, than the Continuous Thermodynamics (CTM) model.

Bhattacharya et. al. [24] uses inter-diffusion model and rapid mixing model to predict the evaporation of two component fuel droplets. The authors found that both models give similar results for evaporation characteristics of liquid fuel with components with close volatility, but for those with higher volatility difference, inter-diffusion model gives more realistic results. This model predicts that though the more volatile component evaporates first from the surface, yet inside composition remains the same. Effects of ambient pressure and gravity on the evaporation of liquid fuel droplets was modelled numerically and discussed by Gogos et. al. [25]. They predicted that the lifetime of the droplet decreases with increasing ambient pressure, but this effect is more pronounced under normal gravity than micro-gravity. This is because under higher ambient pressure, effect of natural convection is more significant in normal gravity condition, which increases the surface temperature of the droplets and thus reducing its lifetime.

2.3 Experimental Works on Combustion of Fuel-droplets

An experimental investigation of liquid fuel combustion on a cross-flow swirl burner was carried out by Kamal et al. [26]. They found that the CO & NO_x emissions are significantly reduced by the introduction of swirl which enhances better mixing and increase kinetics rates. Flame radiation output was 1.9 times more in swirl air burner than the one without swirl. Inspired by the results of Mital & Gore, they put a porous medium in the flame downstream region to enhance the radiation output of the flame. The idea

behind this technique is to prevent any deterioration in mixing between air and fuel, resulting in effective transfer of enthalpy of the burnt gases into the thermal radiation.

An experimental investigation was conducted by Seiser et al. [27] on methanol and ethanol flames in laminar non-uniform flows. They found that the value of strain rate at extinction increases as the equivalence ratio is increased from a value less than unity and reaches a maximum value for equivalence ratio between 1.05 and 1.11. A further increase in equivalence ratio decreases the strain rate extinction value. For constant volume combustion bomb, they found that maximum burning velocity is achieved at an equivalence ratio at around 1.1, while for the twin flame configuration the maximum value is achieved at around 1.15.

Fei et. al. [28] experimentally investigated the combustion characteristics of n-heptane under conditions like equivalence ratio (ER), fuel flow, mixed-gas flow rate and materials. They found that equivalence ratio only affects heat release but doesn't alter the time required for stable combustion. Moreover, with increasing equivalence ratio, wall temperature first increases and then decreases because of poor combustion with lower oxygen concentration at higher ER. They also found a shift in highest wall temperature towards the exit with increasing ER, which they proposed to be because of higher time required in fuel-air mixing as less oxygen is available which eventually causes the combustion zone to move downstream to increase the response time.

An experimental investigation of flame stability and emissions from ethanol combustion at various oxidizer-dilutions was conducted by Lacas et al. [29]. They found that the flame stability and higher extinction velocity both corresponds to higher oxygen

concentrations. Effect of fuel-air rate and air pre-heat on droplet diameter and velocities in a small gas-turbine combustor was experimentally investigated by Heyes et. al. [30]. They found that arithmetic and Sauter mean diameter decreases with increasing air-fuel ratio and preheat temperature because of faster evaporation and burning of droplets. A better combustion efficiency was recorded for lower air-fuel ratio and higher preheat temperature whereas at lower preheat temperature a three-fold increase in unburned hydrocarbon was recorded.

Nejati et al. [31] investigated experimentally the production and emission of NO_x pollutant in a cylindrical furnace liquid fuel, for various angles and patterns of fuel spray. They found that with increasing in the spray angle, a more perfect combustion happens and the maximum flame temperature increases. Also, the concentration of NO_x, which is affected by maximum temperature, increased. Eisazadeh-Far et al. [32] calculated laminar flame speed of ethanol experimentally over a wide range of temperature, pressure, fuel/air equivalence ratio and diluent. Their findings show that the instability occurs at low pressure and temperature in rich ethanol air mixture. Also, laminar flame speed was found to be decreasing with increasing diluent gases. An experimental study on combustion of methane using spray and direct injection is presented by Askari et al. [33]. In another experimental work Brajas et al. [34] compared the combustion characteristics of biofuels in terms of pollutants, radiative heat release, temperature profile etc.

2.4 Numerical Studies on Combustion of Fuel droplets

Greenberg [35] developed a numerical model to simulate a spherical flame front propagating through liquid fuel mist. The model was able to account for the finite rate evaporation of the droplets and the possibility of having a different velocity of the droplets than their surroundings. He found that the vaporization Damkohler number and the droplet drag significantly affect the flame existence and extinction. Also, predicted results for droplet velocity were in good agreement with the experimental data.

Patel and Menon [36] performed a Large Eddy Simulation (LES) of an experimental liquid fuelled Lean Direct Injection (LDI) combustor using a sub-grid mixing and combustion model. They applied Kelvin-Helmholtz break model and comparison with the available experimental data showed a good agreement. They found that break up has a significant impact on fuel evaporation in the vicinity of the injector. However, further downstream, the break up simulation case produces a wide range of droplet sizes and the spray quality produced was similar to that of no breakup case.

Numerical simulations of liquid fuel combustion in fluidized bed by Okasha [37], shows that gas mixing is the rate limiting steps for the in-bed combustion processes. He also predicted that jet velocity, bed temperature, excess air and decrease in fluidization velocity enhance the burning rate of liquid fuel.

Pang et. al. [38] used Combustion Engine research Center (CERC) mechanism developed by Chalmer University of Technology to predict the emissions from a diesel engine. They formulated a reduced chemical mechanism consisting of 109 elementary reactions and 44

species and found a good agreement with the experimental measurements with a maximum error of 4%.

Wang et. al. [39] uses Full Second-order Moment (FSM) Model to simulate methanol air combustion and compared with traditional two phase combustion model and experimental data. They found that FSM model was more successful in predicting the experimental data and temperature peaks because unlike the traditional model, it keeps account of individual droplet burning phenomenon.

Saario et al. [40] numerically simulated the combustion of heavy fuel in a cylindrical furnace. They used both the standard k-ε turbulence model and the Reynolds stress model (RSM). They found that the standard k-ε model does not satisfactorily predict the highly swirling flow field in the furnace. The RSM was able to improve the prediction of the flow field. For highly non-isotropic turbulent flows, RSM gives better results than k-ε model, but it is computationally extensive. For low swirling flows ($S<0.5$) RKE and RNG k-ε can give satisfactory results [41].

A comparative study of Eddy Dissipation Model (EDM) and Probability Density Function (PDF) approach was conducted by Rohani et. al. [42]. They concluded that the PDF gives better prediction of experimental values than EDM, because of implementation of probabilistic approach for relating the turbulence characteristics of the flow field to the thermo-chemical properties of the flame. Ilamathi et. al. [43] utilized an artificial neural network (ANN) to model the unburnt carbon in a coal-fired boiler. The model was coupled with a genetic algorithm (GA) to determine optimum level process parameters which decreases the unburned carbon content in the boiler. It was also

predicted that jet velocity, bed temperature, excess air and decrease in fluidization velocity enhance the burning rate of liquid fuel.

2.5 Oxy-combustion

Combustion of fuel in oxygen-carbon dioxide environment is quite different to that of in air environment and hence, presents new challenges to combustion specialists. Combustion of pulverized coal in oxy-firing burners has significant effect on flame temperature and stability [7]. Numerical investigation of methane oxy-combustion in a water-tube boiler by Habib et al. [44] showed slower rate of reaction in oxygen-carbon dioxide environment than that of air in case if the oxygen present in the oxidizer mixture is less than 29%. Croiset and Thambimuthu [45] experimentally investigated the coal combustion in a reactor with recycled flue gas and found that the flame speed is slower with comparison to combustion in air. However, the obtained results showed that the radiative heat transfer in oxy-carbon dioxide environment is higher due to higher emissivity of the mixture [6,11,46–48].

Liu et al. [49] studied the chemical effect of replacement of N_2 in air with CO_2 on the burning rate of methane and hydrogen premixed flames. They found that the burning rate of methane and hydrogen flames is significantly reduced with the addition of CO_2 in the oxidizer stream and the relative effect increases with the increasing concentration of carbon dioxide. The chemical participation of CO_2 in the combustion is dominated by the following reaction:

$$CO + OH \rightleftharpoons CO_2 + H \quad (1)$$

However, the most important chain branching reaction is:

$$H + O_2 \rightleftharpoons O + OH \quad (2)$$

The competition of CO_2 for H radicals with the second reaction plays an inhibiting role and thus reduces the overall combustion rate.

In an experimental study by Anderson et al. [50] on soot-related radiation effect in oxy-combustion and air combustion, showed a drastic drop in flame temperature as well as delayed combustion in oxygen-carbon dioxide (27% O_2 and 73% CO_2) environment as compared to conventional air combustion. Blarigan et al. [51] experimentally investigated the oxy-combustion of methane in a spark-ignited engine. It was found that the maximum fuel conversion efficiency was achieved with 29% oxygen by volume in the intake for wet exhaust gas recirculation (EGR), while for dry EGR maximum efficiency was achieved at 32.5% oxygen by volume. However, peak fuel-conversion efficiency was found to be significantly reduced for oxy-methane combustion in comparison to methane-air combustion, which was attributed to the reduced ratio of specific heats of the EGR working fluid relative to air. A comparison of direct chemical reaction (combustion) in a partially premixed flame (PPF) and electrochemical reaction in a solid oxide fuel cell (SOFC) of biogas was presented by Quesito et al. [52]. Results showed that the exergetic efficiency of electrochemical oxidation of biogas in a SPFC is much higher than the chemical oxidation in PPF. Moreover, The PPF exhaust stream also contains significant amount of NO_x and C_2H_2 while SOFC exhaust stream doesn't contain any pollutant.

Abdul-Sater and Krishnamoorthy [53] studied the various radiation modelling strategies in simulations of oxy-methane diffusion flames. They confirmed the numerical results with the experimental data that the flame length increases with the increase in fuel-inlet Reynolds number but decreases with the increase in O_2 composition in the oxidizer stream. They used gray and non-gray formulations of weighted-sum-of gray-gas-model (WSGGM) to compute the radiation. They found that the radiant fraction was increasing with the decrease in Reynolds number that was attributed to shorter flames and steeper temperature gradient.

WSGG models are popular for the calculations of radiation with the combustion model because of lower computational cost, better accuracies and ease of implementation. The accuracies of WSGG models were assessed and compared against the standard solutions in prototypical geometries [54–57]. Yin [58] and Krishnamoorthy [54] in their respective studies on numerical investigation of oxy-combustion of natural gas, found that the non-gray gas models are more accurate in predicting the wall fluxes than temperatures. Though, the importance of this model was diminished if the particles are present in the flame. In a numerical study on oxy-combustion of coal in small scale furnaces by Nakod et al. [59], it was concluded that the difference between gray-gas and non-gray gas model was minimal as the particle radiation was prominent than the gas radiation. While in large scale furnaces, where the effect of gas radiation was dominant over the particle radiation, non-gay gas model gives better accuracies [60].

Hjartstam et al. [61] concluded from their numerical investigations on oxy-propane flames in a lab-scale furnace that the non-gray radiation model accurately predicts the source term than the gray model. Also, they found that the inclusion of soot radiation is

more critical in air and oxy-fuel flames than the use of more rigorous description of the radiative properties of the gas. Turbulence Radiation Interaction (TRI) was found to be important for the numerical analysis of oxy-combustion of coal [62] and natural gas [63], due to the presence of large concentrations of radiatively participating gases. However, Krishnamoorthy [54] found that the introduction of TRI was not significant for highly swirling flames.

Although, oxy-fuel combustion is a very promising technique in CCS, lower adiabatic flame temperature, delayed ignition and lower burning rate in O_2-CO_2 environment are some of its major challenges to be dealt with [64–67]. An attempt to increase the thermal efficiency often comes at the cost of increased NOx emissions. Moderate or Intense Low-oxygen Dilution (MILD) combustion technique offers great advantage of achieving higher thermal efficiency in oxy-combustion with reduced pollutant formation [64,68]. Blasiak et al. [69]] investigated the MILD oxy-combustion of natural gas in the thermal treatment processes of wastes and the recovery of zinc bearing feed on a rotary kiln and found that it reduces the fuel consumption as well as NOx emissions in addition to increasing the productivity of the rotary kiln. Krishnamurthy et al. [70] conducted experimental and numerical studies on flameless oxy-fuel combustion in a low intensity (26 kW/m^3) burner. They found that soot and NO_x formation is significantly reduced in flameless combustion. In addition, flameless combustion has the advantage of more uniform temperature and heat flux distributions than flame mode, however, radiative heat flux in both modes were found to be the same.

CHAPTER 3

MATHEMATICAL MODELING

3.1 Model Development

Turbulent combustion modeling is a broad subject, which involves a wide range of coupled problems like fluid properties, detailed chemical reaction scheme, two or three phase system and radiative heat transfer [71]. The turbulence model is governed by the classical Navier-Stokes, species and energy transport equations in modified form by incorporating Reynolds and Favre averaging [71]. These partial differential equations are discretized and approximated by algebraic equations for finite number of volumes in the domain [72].

3.1.1 Reactor Design, Boundary and Inlet Conditions

The boiler geometry shown in Figure 7, having length of 12.54 m, width of 6.86 m and height of 7.25 m, has been considered for simulating the liquid fuel oxy-combustion. The geometry was divided into more than 1,000,000 finite volumes and grids were concentrated in the regions of high gradient to minimize the diffusion error. Details about the mesh can be found in previous papers [44]. The boiler walls were assigned constant temperature boundary condition equivalent to the saturation temperature of water-steam corresponding to the boiler pressure. Water jackets in the tube banks were also given the

constant temperature boundary condition with the same value. The liquid fuel was injected through an injector surrounded by the primary air. The primary air was injected through an annular section surrounding the injector and had tangential velocity component with a swirl angle of 45^{o}. The secondary air was introduced surrounding the primary air without any swirl. Fuel droplets were injected at a temperature of 300 K with the droplet size of 10 microns. Stochastic tracking of the particles was calculated using Discrete Random Walk Model with 20 numbers of tries. Mass flow rate of the fuel was 2.108 kg/s for all the three cases. Primary and secondary air inlet were given an axial velocity of 37.78 m/s for air and OF21 case, while for OF29 case it was 27.36 m/s such that mass flow rate of oxygen is the same for all the three cases. The equivalence ratio was maintained at 0.8 for all cases.

3.1.2 General Conservation Equations

In the present numerical model, the mass, momentum, energy, and species transport conservation equations were numerically solved for the scalar quantities. The flow field, thermal field and species concentration are obtained through the solution of the 3-d elliptic conservation equations inside the reactor. All of these conservation equations including mass, momentum, energy, and species transport can be written in a general form as function of the parameters which are the Reynolds averaged and fluctuating values of the general dependent variable as flows [73]:

$$\frac{\partial}{\partial x_j}\left(\overline{\rho}\overline{U}_j\Phi + \overline{\rho}\overline{u}_j\phi\right) = \frac{\partial}{\partial x_j}\left[\Gamma_\phi \frac{\partial \Phi}{\partial x_j}\right] + \overline{\rho}S_\Phi \quad (3)$$

Where, $\overline{\rho}$ is the density, $\overline{U}$ is the velocity component, $\overline{u_i}$ is the turbulent velocity component, Γ_Φ is the diffusion coefficient, and S_Φ is the source term. When 'Φ' equals to one, this equation represents the mass conservation equation; and when equals to the velocity, it represents the momentum equation. When 'Φ' equals to the enthalpy, this equation represents the energy equation; and finally when equals to the scalar mass fraction, this equation represents the species transport equation. The continuity and momentum equations linkage was based on SIMPLE method.

3.1.3 Turbulence-chemistry Interaction

The turbulent flow of the gases in the reactor is governed by the conservation of mass, momentum and energy equations. These partial differential equations are discretized and approximated by algebraic equations for finite number of volumes in the domain [72]. The present work utilizes the Realizable k-ε model (2-equations) (RKE) and the Reynolds Stress (5-equations) model (RSM) to predict the turbulent characteristics of the flow. RKE model is successful in predicting the flow pattern involving rotation, separation and recirculation [41]. However, RSM gives better results than RKE for highly non-isotropic turbulent flows, as it directly solves the Reynolds stress terms in the momentum equation [74]. In the RKE model, the turbulent scalar fluxes and the Reynolds stresses are related

to the mean velocities gradients and the scalar variable via the following exchange coefficients:

$$-\rho\overline{u_i u_j} = \mu_t\left(\frac{\partial\overline{U_i}}{\partial x_j}+\frac{\partial\overline{U_j}}{\partial x_i}\right)-\frac{2}{3}\rho k\delta_{ij} \tag{4}$$

$$-\rho\overline{u_j\phi} = \Gamma_\Phi\frac{\partial\Phi}{\partial x_j} \tag{5}$$

Where Γ_Φ is equal to μ_t/σ_Φ, and μ_t is the turbulent viscosity which can be defined as follows:

$$\mu_t = c_\mu\rho k^2/\varepsilon \tag{6}$$

Where, c_μ and σ_Φ are predefined fixed values, and the turbulent viscosity is determined through solution of both *k* and *ε* transport equations. The modelled transport equations for *k* and *ε* in the realizable *k*-*ε* model are [72]:

$$\frac{\partial}{\partial t}(\rho k)+\frac{\partial}{\partial x_j}(\rho k u_j)=\frac{\partial}{\partial x_j}\left[\left(\mu+\frac{\mu_t}{\sigma_k}\right)\frac{\partial k}{\partial x_j}\right]+G_k+G_b-\rho\varepsilon-Y_M+S_k \tag{7}$$

And:

$$\frac{\partial}{\partial t}(\rho\varepsilon)+\frac{\partial}{\partial x_j}(\rho\varepsilon u_j)=\frac{\partial}{\partial x_j}\left[\left(\mu+\frac{\mu_t}{\sigma_\varepsilon}\right)\frac{\partial\varepsilon}{\partial x_j}\right]+\rho C_1 S\varepsilon-\rho C_2\frac{\varepsilon^2}{k+\sqrt{\upsilon\varepsilon}}+C_{1\varepsilon}\frac{\varepsilon}{k}C_{3\varepsilon}G_b+S_\varepsilon \tag{8}$$

Where:

$$C_1=\max\left[0.43,\frac{\eta}{\eta+5}\right],\qquad \eta=S\frac{k}{\varepsilon},\qquad S=\sqrt{2S_{ij}S_{ij}}$$

In these equations, G_k represents the generation of turbulence kinetic energy due to the mean velocity gradients. G_b is the generation of turbulence kinetic energy due to buoyancy. Y_M represents the contribution of the fluctuating dilatation in compressible turbulence to the overall dissipation rate. $C_{2\varepsilon}$ and $C_{1\varepsilon}$ are constants with the value of 1.44 and 1.92, respectively. σ_k and σ_ε are the turbulent Prandtl numbers for k and ε and were given a value of 1 and 1.2, respectively. S_K and S_ε are user defined source terms.

For the Reynolds stress model, the six equations are given by [72]:

$$\underbrace{\frac{\partial R_{ij}}{\partial t}}_{\text{Rate of change of } R_{ij}=\overline{u_i' u_j'}} + \underbrace{\frac{\partial\left(\rho U_k \overline{u_i' u_j'}\right)}{\partial x_k}}_{\text{Transport of } R_{ij} \text{ by convection}} = P_{ij} + D_{ij} - \varepsilon_{ij} + \Pi_{ij} + \Omega_{ij} \tag{9}$$

Here, $R_{ij} = -\tau_{ij}/\rho = \overline{u_i' u_j'}$ is the Reynolds stress.

$$P_{ij} = \underbrace{-\left(R_{im}\frac{\partial U_j}{\partial x_m} + R_{jm}\frac{\partial U_i}{\partial x_m}\right)}_{\text{Rate of Production } R_{ij}} \tag{10}$$

$$D_{ij} = \underbrace{\frac{\partial}{\partial x_m}\left(\frac{\nu_t}{\sigma_k}\frac{\partial R_{ij}}{\partial x_m}\right)}_{\text{Transport of } R_{ij} \text{ by Diffusion}} \tag{11}$$

where, $\nu_t = C_\mu \frac{k^2}{\varepsilon}, C_\mu = 0.09$ *and* $\sigma_k = 1.0$.

$$\varepsilon_{ij} = \underbrace{\frac{2}{3}\varepsilon\delta_{ij}}_{\text{Rate of dissipation of } R_{ij}} \tag{12}$$

ε is the dissipation rate of turbulent kinetic energy given by $\varepsilon = 2\nu\overline{s_{ij}'.s_{ij}'}$ where, s_{ij}' is the fluctuating deformation rates.

$$\Pi_{ij} = \underbrace{-C_1\frac{\varepsilon}{k}\left(R_{ij}-\frac{2}{3}k\delta_{ij}\right)-C_2\left(P_{ij}-\frac{2}{3}P\delta_{ij}\right)}_{Transport\ of\ R_{ij}\ due\ to\ turbulent\ \ pressure-strain\ \text{int}eractions} \quad (13)$$

The constants $C_1 = 1.8$ *and* $C_2 = 0.6$.

$$\Omega_{ij} = \underbrace{-2\omega_k\left(\overline{u_j'u_m'}e_{ikm}+\overline{u_i'u_m'}e_{jkm}\right)}_{Transport\ of\ R_{ij}\ due\ to\ rotation} \quad (14)$$

ω_k is the rotational vector and e_{ijk} is the alternating symbol where, e_{ijk} = +1 if *i,j* and *k* are different and in cyclic order, e_{ijk} = -1 if *i,j* and *k* are different and in anti-cyclic order; and e_{ijk} = 0 if any two indices are same.

In non-premixed combustion like in the present model, the reaction between fuel and oxidizer takes place when the mixing occurs at molecular level. When the mixing time scale is much longer than the reaction time scale, Probability Density Function (PDF) approach can be conveniently applied to predict the combustion characteristics and gives better accuracy compared to Eddy Dissipation Model (EDM). For a simple single-step stoichiometric reaction:

$$Fuel + s\,Oxident \rightarrow (1+s)\,\text{Pr}oducts \quad (15)$$

The transport equations for fuel and oxygen mass fraction are given by:

$$\frac{\partial\left(\rho Y_{fu}\right)}{\partial t} + div\left(\rho Y_{fu}\vec{u}\right) = div\left(\Gamma_{fu}\,grad\,Y_{fu}\right) + \dot{\omega}_{fu} \quad (16)$$

$$\frac{\partial(\rho Y_{ox})}{\partial t} + div\left(\rho Y_{ox}\vec{u}\right) = div\left(\Gamma_{ox} grad\, Y_{ox}\right) + \dot{\omega}_{ox} \quad \textbf{(}17\text{)}$$

where $\Gamma_{fu} = \rho D_{fu}$ *and* $\Gamma_{ox} = \rho D_{ox}$ and D is the diffusion coefficient. Y_{fu} and Y_{ox} represent the mass fraction of fuel and oxidizer respectively.

It is possible to reduce the number of transport equations by introducing a variable defined as follows:

$$\phi = sY_{fu} - Y_{ox} \quad \textbf{(}18\text{)}$$

Assuming the diffusion coefficient for to be same for all the species we have, $\Gamma_{fu} = \Gamma_{ox} = \rho D = \Gamma_{\phi}$. Thus, subtracting equation (18) from *s* times equation (17), we get a single transport equation for ϕ:

$$\frac{\partial(\rho\phi)}{\partial t} + div\left(\rho\phi\vec{u}\right) = div\left(\Gamma_{\phi} grad\, \phi\right) \quad \textbf{(}19\text{)}$$

Knowing that for the one-step reaction assumption we have $(s\dot{\omega}_{fu} - \dot{\omega}_{ox}) = 0$ and hence we get a scalar transport equation without a source term. A non-dimensional variable *'f'* called the mixture fraction can be defined as:

$$f = \frac{\phi - \phi_0}{\phi_1 - \phi_0} \quad \textbf{(}20\text{)}$$

or rewritten as:

$$f = \frac{sY_{fu} - Y_{ox} + Y_{ox,0}}{sY_{fu,1} + Y_{ox,0}} \quad \textbf{(}21\text{)}$$

where, the subscripts *'0'* and *'1'* represent oxidant and fuel stream respectively.

By equation (20) '*f*' is linearly related to 'ϕ' so the mixture fraction is also a passive scalar and obeys the transport equation:

$$\frac{\partial(\rho f)}{\partial t}+\frac{\partial}{\partial x_i}(\rho u_i f)=\frac{\partial}{\partial x_i}\left(\Gamma_f \frac{\partial f}{\partial x_i}\right) \quad \textbf{(}22\text{)}$$

Now, Probability Density function, which can be defined as the fraction of time the fluid spends in the vicinity of state *'f'*, is given by the following equation:

$$p(f)\Delta f=\lim_{T\to\infty}\frac{1}{T}\sum_i \tau_i \quad \textbf{(}23\text{)}$$

where, *'T'* is the time scale and τ_i is the amount of time that *'f'* spends in the Δf band.

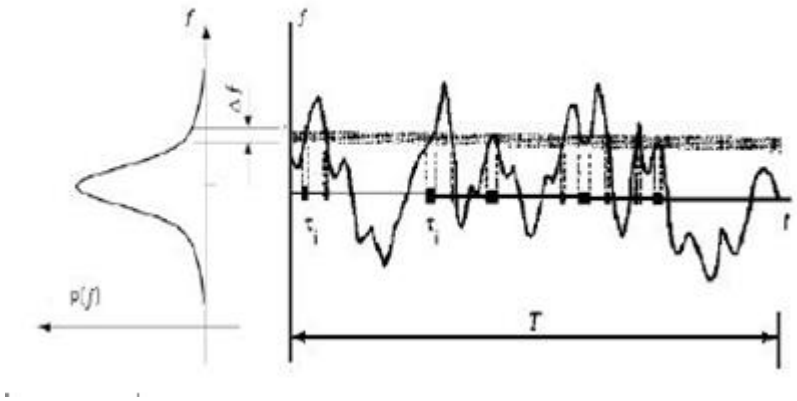

Figure 8. Graphical representation of Probability Density Function

Favre (density weighted) average of any other scalar quantities, like temperature and species, can be calculated by integrating the product of the scalar & PDF [72]. Fluent provides an excellent tool to generate a PDF table for a desired composition of fuel and

oxidiser stream, by performing the chemistry calculations and co-relating the gas variables with the mixture fraction. The density-weighted average of any scalar quantity ϕ, which is itself a function of f , may be obtained from:

$$\phi = \int_0^1 \phi(f) P(f) df \quad \textbf{(}24\textbf{)}$$

where, superscript '~' denotes the density-weighted average of the quantity. Beta functions and delta function pdfs have been used to approximate the measured distributions.

3.1.4 Discrete Phase Model

The Euler-Lagrange approach is utilized to solve the discreet phase model. The gaseous phase treated as continuum, while the dispersed phase is solved by tracking the particles/droplets through the calculated flow field, where both the phases can exchange mass, momentum and energy. The trajectory of discrete particle is predicted by integrating the force balance on the particle in the Lagrangian reference frame [75]:

$$\frac{du_p}{dt} = F_D(\vec{u} - \vec{u}_p) + \frac{g_x(\rho_p - \rho)}{\rho_p} + \vec{F}_x \quad \textbf{(}25\textbf{)}$$

where,

$$F_D = \frac{18\mu}{\rho_p d_p^2} \frac{C_D \,\mathrm{Re}}{24} \quad \textbf{(}26\textbf{)}$$

$F_D(\vec{u}-\vec{u}_p)$ is the drag force per unit particle mass and $\overrightarrow{F_x}$ is the force arising due to the pressure gradient along the fluid. Here, $\vec{u}$ is the gaseous phase velocity, $\vec{u}_p$ is the droplet velocity, μ is the molecular viscosity of the gas, ρ is the gas density, ρ_p is the density of the droplet and d_p is the droplet diameter. C_D is the drag co-efficient and is calculated by the method proposed by Morsi and Alexander [76]. The dispersion of droplets is calculated through Stochastic tracking (Discrete Random Walk) model, which solves the interaction of the droplets with a succession of discrete stylized fluid phase turbulent eddies.

The heat and mass transfer for discrete phase are solved by incorporating three Laws. When droplet temperature is less than the vaporization temperature, the inert heating Law is applied:

$$m_p c_p \frac{dT_p}{dt} = hA_p\left(T_\infty - T_p\right) + \varepsilon_p A_p \sigma\left(\theta_R^4 - T_p^4\right) \quad (27)$$

where, m_p is mass of the particle, c_p is heat capacity of the particle, A_p is surface area of the particle, T_∞ is local temperature of the continuous phase, h is convective heat transfer coefficient, ε is particle emissivity, σ is Stefan-Boltzman constant and θ_R is the radiation temperature given by $\left(\frac{G}{4\sigma}\right)^{1/4}$ where, G is the incident radiation in W/m^2 given by $G = \int_{\Omega=4\pi} Id\Omega$, where *'I'* is the radiation intensity and 'Ω' is the solid angle.

And the heat transfer co-efficient is calculated using the correlation of Ranz & Marshall [77]:

$$h = \frac{k_\infty}{d_D}\left[2 + 0.6\,\mathrm{Re}_d^{1/2}\,\mathrm{Pr}^{1/3}\right] \quad \textbf{(}28)$$

where, Re_d is the Reynolds number of the droplet based on relative velocity of the droplet and gaseous phase and *Pr* is the Prandlt number of the continuous phase.

Droplet Vaporization Law is applied when droplet temperature is above the vaporization temperature but below the boiling point. The flux of droplet vapour into the gas phase is related to the gradient of the vapour concentration between the droplet surface and the bulk gas. The molar flux of vapour is given by:

$$N_i = \kappa_c \left(C_{i,s} - C_{i,\infty}\right) \quad \textbf{(}29)$$

Where, κ_c is mass transfer coefficient, $C_{i,s}$ vapour concentration at droplet surface and $C_{i,\infty}$ is vapour concentration in the bulk gas.

Vapour concentration at the droplet surface is computed by assuming that the partial pressure of vapour at the interface is equal to the saturated vapour pressure, p_{sat}, at the particle droplet temperature, T_p**,** and is given by:

$$C_{i,s} = \frac{p_{sat}\big)_{T_p}}{RT_p} \quad (30)$$

where, *R* is the universal Gas constant. The concentration of vapour in the bulk gas is calculated by:

$$C_{i,\infty} = X_i \frac{p}{RT_\infty} \tag{31}$$

where, X_i is the local bulk mole fraction of species *i*, *p* is the local absolute pressure, T_∞ is the local bulk temperature in the gas and *R* is the universal gas constant. Mass transfer coefficient, κ_c, is calculated from the Sherwood number correlation [77]:

$$\kappa_c = \frac{D_{i,m}}{d_p}\left(2.0 + 0.6\,\mathrm{Re}_d^{1/2}\, Sc^{1/3}\right) \tag{32}$$

where, $D_{i,m}$ is the diffusion coefficient of vapour in the bulk (m^2/s) and *Sc* is the Schmidt number.

Droplet Boiling Law is applied to predict the convective boiling of the droplet when the temperature of the droplet has reached the boiling point.

$$-r\frac{dm_p}{dt} = hA_p\left(T_\infty - T_p\right) + \varepsilon_p A_p \sigma\left(\theta_R^4 - T_p^4\right) \tag{33}$$

where, $\frac{dm_p}{dt}$ is the rate of evaporation of the droplet in *kg/s* and *r* is the latent heat.

3.1.5 Radiation Model

Discreet Ordinate (DO) model is used to solve radiative heat transfer in the reactor, with 5 flow iterations per radiative iteration. The DO model solves the radiative transfer equation by dividing the entire solid angle into finite number of angular spans, each associated with a vector direction $\vec{s}$ fixed in global Cartesian system *(x,y,z)* [75].

$$\frac{dI(\vec{r},\vec{s})}{ds}+(a+\sigma_s)I(\vec{r},\vec{s})=an^2\frac{\sigma T^4}{\pi}+\frac{\sigma_s}{4\pi}\int_0^{4\pi}I(\vec{r},\vec{s}')\Phi(\vec{s}.\vec{s}')d\Omega' \quad (34)$$

Where, $\vec{r}$ is the position vector, $\vec{s}$ is the direction vector, $\vec{s}'$ is the scattering direction vector, s is the path length, a is the absorption coefficient, σ_s is the scattering coefficient, I is the radiation intensity, T is the local temperature, Φ is the phase function and Ω' is the solid angle. Here *'n'* is the refractive index and taken as unity. Absorption co-efficient of the gas mixture is determined by domain based Weighted sum-of-gray-gas model (WSGGM). The internal emissivity of all the walls is taken 0.7.

3.1.6 Soot Model

One step Khan and Greaves model was applied to solve the single transport equation for the soot mass fraction [75], given by:

$$\frac{\partial}{\partial t}\left(\rho Y_{soot}\right)+\nabla.\left(\rho\vec{v}Y_{soot}\right)=\nabla.\left(\frac{\mu_t}{\sigma_{soot}}\nabla Y_{soot}\right)+\Re_{soot} \quad (35)$$

Where;

Y_{soot} = soot mass fraction

σ_{soot} = turbulent Prandtl number for soot transport

$\Re_{soot}$ = net rate of soot generation (kg/m^3-s)

The net rate of soot generation is the difference of soot formation and soot combustion:

$$\Re_{soot}=\Re_{soot,form}-\Re_{soot,comb} \quad (36)$$

The rate of soot formation is given by:

$$\Re_{soot,\,form} = C_s\, p_{fuel} \phi^r e^{-E/RT} \tag{37}$$

Where;

C_s = soot formation constant (kg/N-m-s)

p_{fuel} = fuel partial pressure (Pa)

ϕ = equivalence ratio

r = equivalence ratio exponent

E/R = activation temperature

The rate of soot formation is given by the minimum of the two expressions [78]:

$$\Re_{soot,comb} = \min\left[\Re_1, \Re_2\right] \tag{38}$$

And the two rates are computed as:

$$\Re_1 = A\rho Y_{soot} \frac{\varepsilon}{k} \tag{39}$$

and,

$$\Re_2 = A\rho \left(\frac{Y_{ox}}{\nu_{soot}} \right) \left(\frac{Y_{soot}\nu_{soot}}{Y_{soot}\nu_{soot} + Y_{fuel}\nu_{fuel}} \right) \frac{\varepsilon}{k} \tag{40}$$

Where;

A = constant in the Magnussen model

Y_{ox}, Y_{fuel} = mass fractions of oxidizer and fuel

ν_{soot}, ν_{fuel} = mass stoichiometries for soot and fuel combustion

3.2 Numerical Study

In this section, an experimental work conducted by Lacas et al. [29] has been modeled numerically. The problem definition and the methodology involved has been discussed in details. The results were validated with the experimental values.

3.2.1 Problem Definition & Solution Procedure

An experimental work on oxygen enriched combustion of ethanol in a vertical reactor by Lacas et al. [29] has been modeled numerically. Figure 9 shows schematic diagram of the experimental setup used in the literature. The two-dimensional geometry of the reactor modelled in the present study is shown in Figure 10. Since the combustion chamber is vertical and gravity is acting in the axial direction, an axis-symmetric model of the reactor is simulated. Grid independency check was performed and it was observed that further refinement of more than 9500 cells does not have much effect on the results, so this grid is employed to model the experiment. The outer wall is given as a mixed (convection-radiation) boundary condition with coefficient of heat transfer as 20 W/m^2K and emissivity as 0.8. Characteristic length of the annular inlet is considered for the Reynolds number. Droplets with a mean diameter of 10 microns are injected at 300K. Soot formation was computed as a part of main combustion solution and was coupled with the radiation model to include the effects of soot on the radiation absorption coefficient.

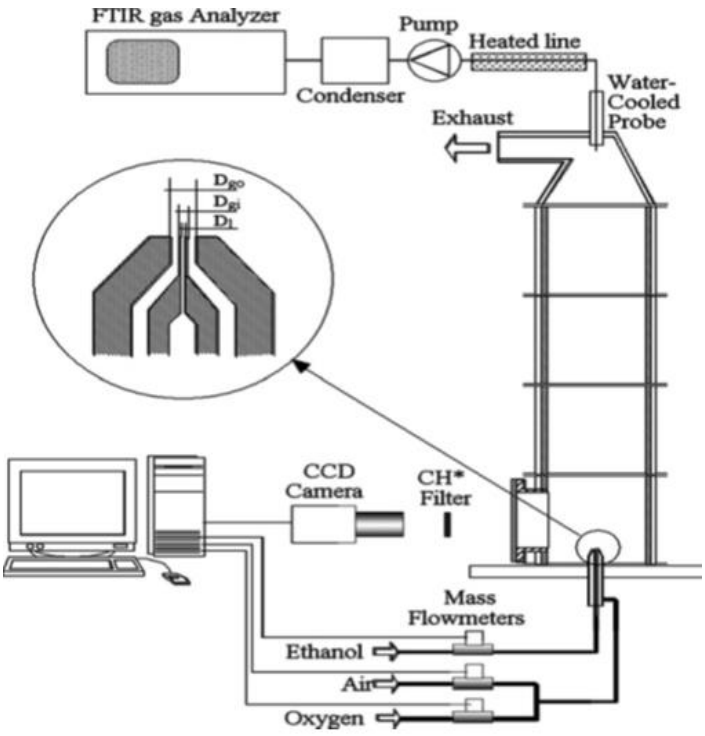

Figure 9. Schematic view of Experimental setup used by Francois et.al.

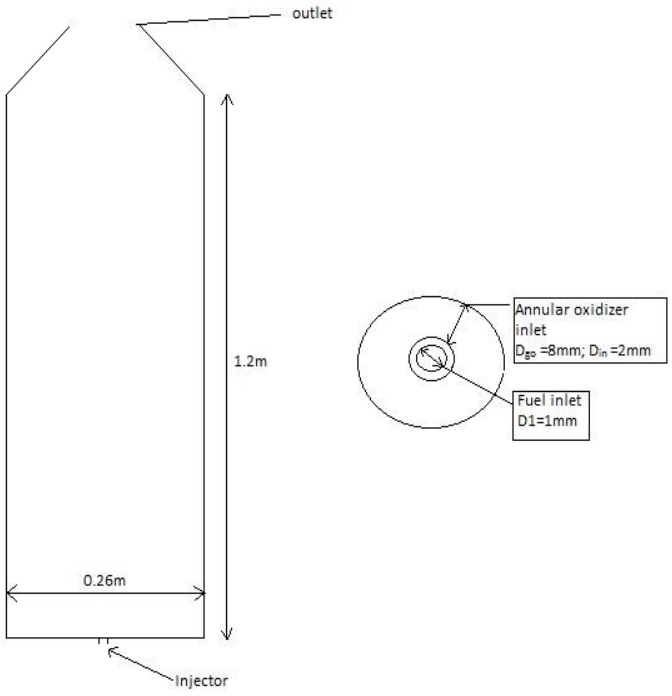

Figure 10. Schematic diagram of the vertical reactor and the injector

3.2.2 Validation of the Numerical Model with Experimental Data

The experimental data for different oxygen enriched air combustion cases of ethanol for the same reactor under the same operating conditions are available in the work conducted by Lacas et al. [29]. The combustion of liquid ethanol droplet has been performed experimentally under a fuel flow rate of 1.5006×10^{-4} kg/s and an equivalence ratio of 0.4. The flame stability has been checked under different concentrations of oxygen in the oxygen enriched air oxidizer mixture. The numerical model has been verified against the experimental data available for the combustion of ethanol in a vertical reactor in the literature. Characteristics of the injector are given in Table 2. As discussed earlier, air doesn't have any swirl, so RKE was employed to solve the flow field as this model is computationally faster than RSM [41]. Figure 11 shows a comparison between the experimental flame shape captured at steady state conditions and the corresponding calculated flame shape using the temperature contours under different percentages of oxygen in the oxygen enriched air. The upper case letters represents the experimental pictures while the lower case letters represents the numerical contours.

Experimental flame picture is the average of 100 images of CH* emission fluctuations taken by CCD camera using a CH* filter [29]. The filter was centred on the emission band of CH* radical and its chemiluminescence is considered to be a good representative of the heat release. As shown in the figure, the experimental and numerical flame shapes are very similar in terms of flame zone and flame height. The applied equivalence ratio is 0.4 which should result in more oxygen availability in the combustion zone. This should result in complete combustion of the fuel and enhance the stability of the flame.

Table 2. Injector Characteristics

Oxidizer channel external dia.	D_{go}	8 mm
Oxidizer channel internal dia.	D_{in}	2 mm
Liquid channel dia.	D_l	1 mm
Oxidizer flow velocity	U_g	71 ms^{-1}
Liquid Flow velocity	U_l	1.3 ms^{-1}
Global Equivalence ratio	Φ	0.4
Oxidizer flow Reynolds Number	Re_x	30060

However, increasing the oxygen concentration at the inlet section should result in more stability of the flame as shown in Figure 11. The flame length is extended in case of higher oxygen concentrations indicating continuous combustion of the lately broken down droplets. Also, the temperature in the flame zone is increased with the increased oxygen concentration in the oxidizer mixture. However, in case of lower oxygen concentrations, the region of stoichiometric combustion is reduced, as a result, the flame length is shortened and complete combustion may not be attained. In reality, oxygen concentration in the combustion zone has significant effect on the burning speed of the fuel and the flow field especially in cases of liquid fuels are used [79].

Figure 12 shows a comparison of the experimental and numerical temperature profiles along the radial direction at different heights inside the reactor of 32cm, 44cm, and 62cm, respectively. This comparison is done for the case of pure oxygen combustion, 100% of oxygen is fed at the oxidizer inlet section, under an operating equivalence ratio of 0.4.

The numerically predicted flame temperature data are in good agreement with the experimentally recorded values at all of the considered heights with the maximum difference of 6.87%. It can also be seen from the figure that the temperature profiles are flattened and the temperature values are reduced with the height from the nozzle. This can be attributed to the reduced combustion reactions intensity with the distance from the inlet nozzle. However, at lower heights, the temperature is maximum close to the centreline of the reactor where the intense combustion reactions exist and it reduced towards the reactor walls due to the diffusion of heat transfer and losses through the reactor walls. In the present case, the applied equivalence ratio is 0.4 which should result in lowering the flame close to the inlet nozzle so that the maximum temperature is obtained in the close region to the inlet nozzle.

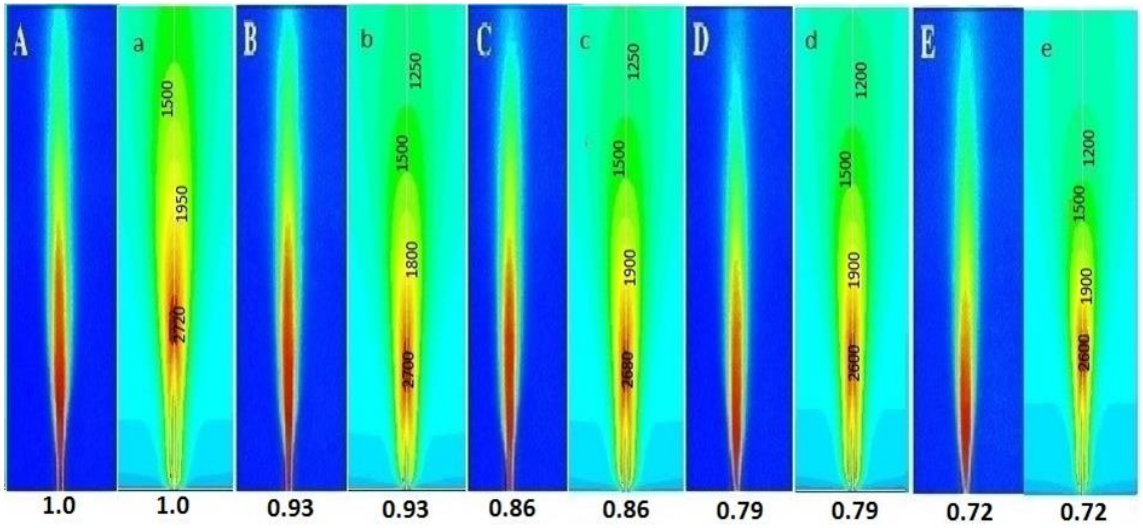

Figure 11. Comparison between the experimental [29] flame shapes captured at steady state conditions (A, B, C, D and E) and the corresponding calculated flame shapes using the temperature (K) contours (a, b, c, d, and e) under different mass fractions of oxygen in the oxidzer mixture

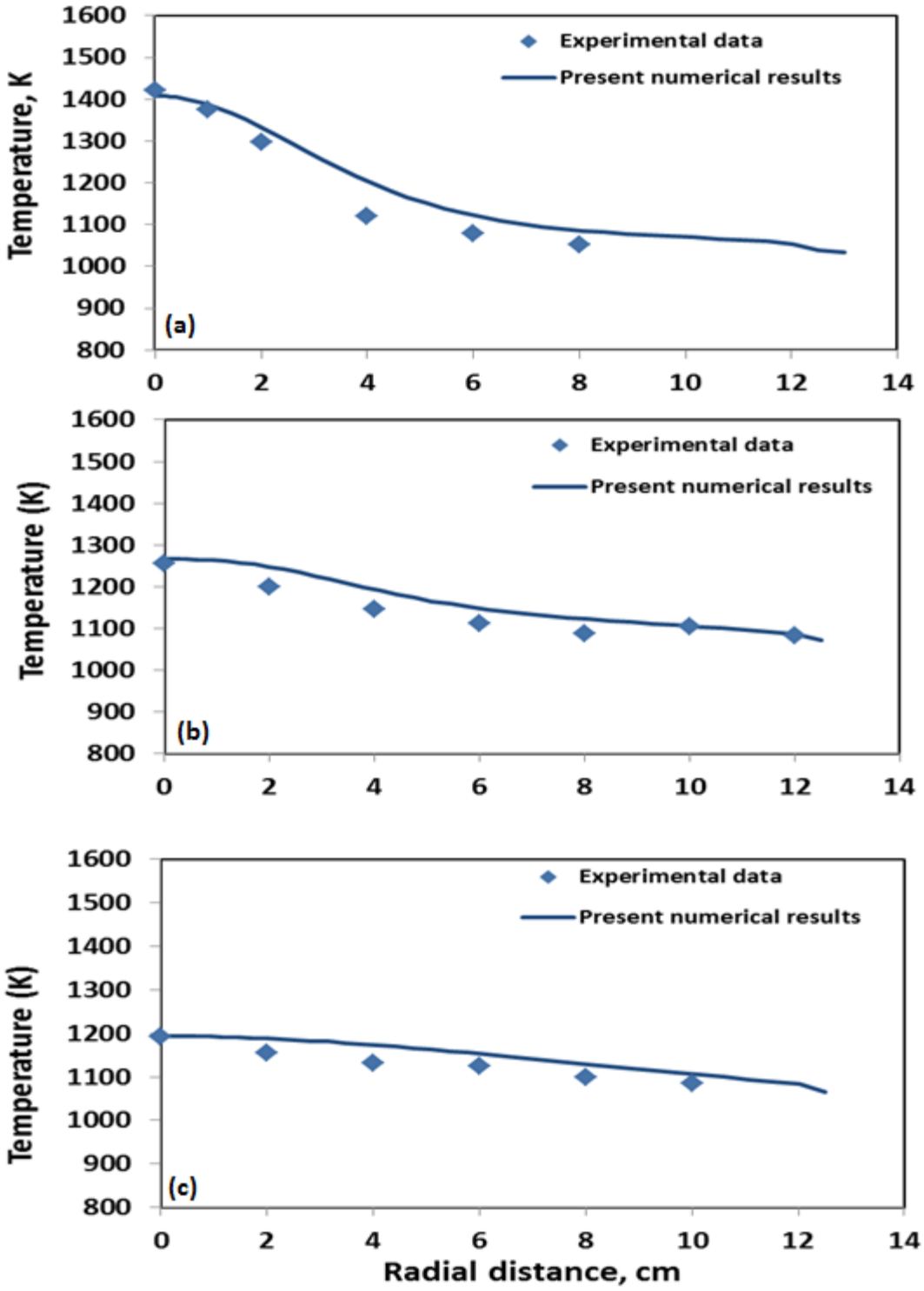

Figure 12. Comparison between experimental [29] and numerical radial temperature profiles at different heights inside the reactor including (a) 32 cm, (b) 47 cm and (c) 62 cm under pure oxy-combustion conditions (100% O_2).

CHAPTER 4

RESULTS AND DISCUSSION

4.1 Ethanol Combustion in a Vertical Reactor

The vertical reactor modeled and verified against experimental data in the previous section has been extended to study (i) the choice of turbulence models, (ii) effects of dilution of oxidizer stream with carbon dioxide and (iii) effect of soot on radiation for ethanol combustion.

4.1.1 Choice of Turbulence Model

In this section, a comparison is made to investigate the effect of turbulence model on the accuracy of the calculated data considering the case of OF29 (29% O_2 and 71% CO_2) oxidizer mixture. In this regard, two turbulence models are investigated including the 2-equations realizable k-ε model (RKE) and the 5-equations Reynolds stress model (RSM). Figure 13 shows the comparison of radial temperature profiles using RKE model RSM model with the experimental data. The results are for complete oxy-combustion case (without any carrier gas) at the height of 32 cm from the injector. It can be seen that RKE model is more successful in predicting the temperature level as compared to RSM model.

A comparison between the two models for OF29 case is presented in Figure 14. As a function of axial temperature and oxygen mass fraction profiles through the reactor height for the OF29 case. As shown in Figure 14 (a), the RSM overpredicts the maximum temperature inside the combustion zone. However, there are no major differences between the oxygen mass fraction profiles predicted by the two models as shown in Figure 14 (b).

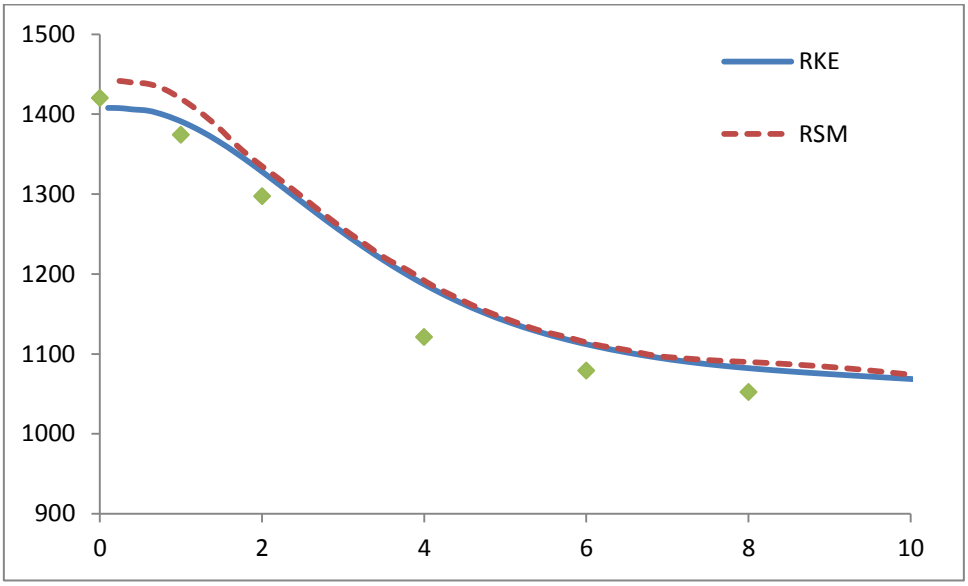

Figure 13. Comparison of radial temperature profile using RKE model and RSM model with the experimental data at the height of 32 cm

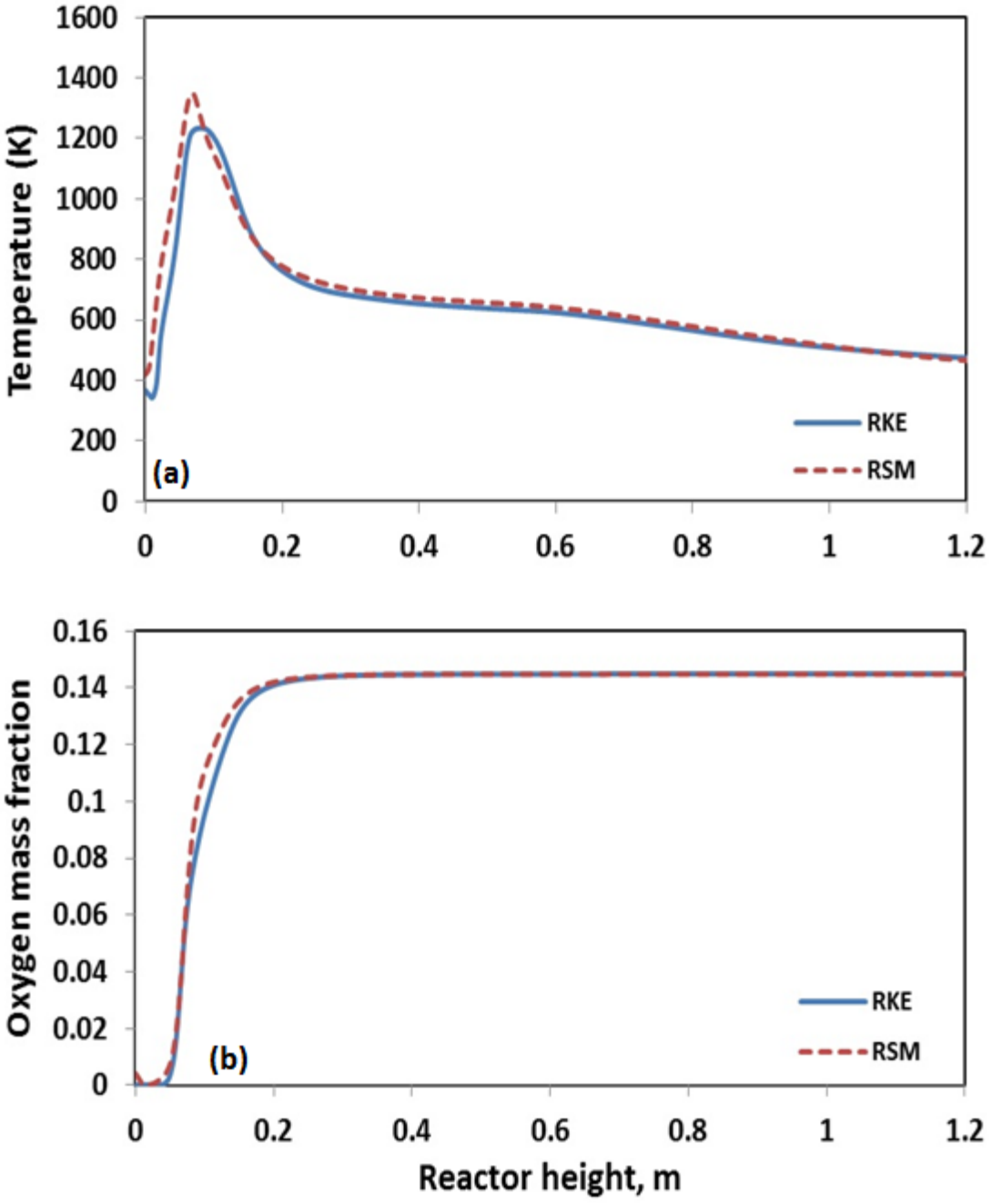

Figure 14. Comparison between the RKE and the RSM models in terms of (a) axial temperature profile, and (b) axial oxygen mass fraction distribution, calculated through the reactor centreline for the case of OF29.

In the comparison Figure 12, between the experimental and the numerical data for the temperature profiles, the RKE turbulence model is the applied turbulence model. As shown in these figures, the RKE model predicts very well the temperature profile inside the reactor. This may be attributed to the model abilities in solving the vertical combustible flows [79]. In fact, the realizable model satisfies certain mathematical constraints on the normal stresses, consistent with the physics of turbulent flows. In addition, the applied RKE turbulence model contains the latest formulation for the turbulent viscosity and turbulent energy dissipation. The model prediction was proven to be more accurate in flows involving strong streamline curvature, rotation, boundary layers under strong adverse pressure gradients, separation, and recirculation [80]. The calculated turbulent intensity values through the reactor centreline are presented in Figure 15 for the two turbulence model at the OF29 case. As shown in the figure, the RSM over predicts the value and the location of the maximum turbulence intensity especially close to the inlet nozzle. This may be attributed to the over prediction of the maximum temperature inside the reaction zone. This may also justify the early increase in the specific thermal capacity of the gases inside the reaction zone and close to the inlet nozzle as shown in Figure 15 (b). Initial studies have shown that the realizable model provides the best performance of all the k-ε model versions for several validations of separated flows and flows with complex secondary-flow features including channel and boundary-layer flows, and separated flows. According to the above discussion, the RKE turbulence model was applied in all simulations.

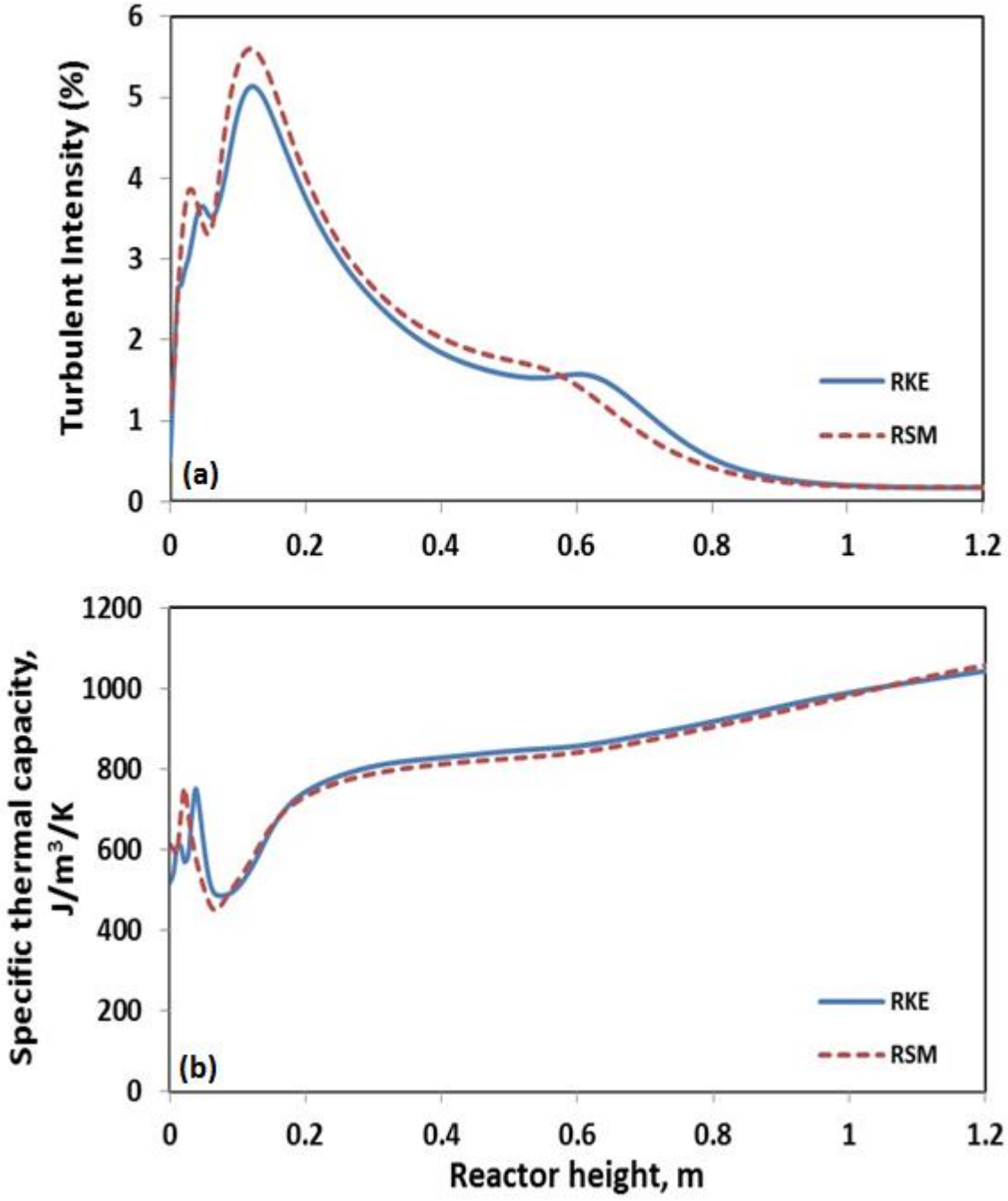

Figure 15. Comparison between the RKE and the RSM models in terms of (a) axial turbulent intensity profile, and (b) axial specific thermal capacity distribution, calculated through the reactor centreline for the case of OF29.

4.1.2 Effect of Dilution of Oxidizer Stream with Carbon Dioxide

In this section, comparisons are performed between the combustion of pure air and the combustion using different mixtures of oxygen and carbon dioxide. Two concentrations of oxygen and carbon dioxide are considered including OF21 and OF29. Figure 16 compares the flame shape and temperature distributions for the three cases. As shown in the figure, replacing nitrogen by carbon dioxide results in a great modification in the flame shape and temperature distribution. Air combustion resulted in similar temperature distribution and flame shape to the case of OF29. This is clear in Figure 18 (b) from the axial distribution of the temperature through the reactor centerline. However, for the case of OF21, the flame is lifted and the combustion temperature is reduced as compared to the air combustion case. Flame lift off is an unwanted condition in which the flame and burner become separated. This flame lift may be attributed to the increased Reynolds number as the amount of carbon dioxide is increased due to its higher molecular weight. This is clearly presented in Figure 17 from the contour plots of total velocity for the three combustion cases. As shown in the figure, the replacement of nitrogen by carbon dioxide for OF21 does not change volume flow rate and hence the velocity contours for the two cases are similar. However, to maintain same oxygen flux, volume flow rate is reduced in OF29 case due to higher oxygen concentration. Thus, velocity level is the lowest for OF29 case.

Also, modification in the burning velocity is expected in case of using carbon dioxide instead of nitrogen. Increasing the amount of carbon dioxide in the combustion zone should result in reduced burning velocity and modified distributions of species

concentrations and temperature [79]. This lowered burning velocity can be attributed to the chemical effects, lower thermal diffusivity, and higher molar heat capacity of CO_2 and modified distribution of the radiation heat transfer [71]. This fact is clearly presented in Figure 18 (a) and Figure 18 (b) form the axial distributions of the temperature and the absorbed radiation heat transfer by the reactor wall. Similar radiation heat transfer profiles are obtained for the combustion cases of air and OF29 as shown in the figure; however, the amount of radiation heat transfer is reduced in the combustion case of OF21.

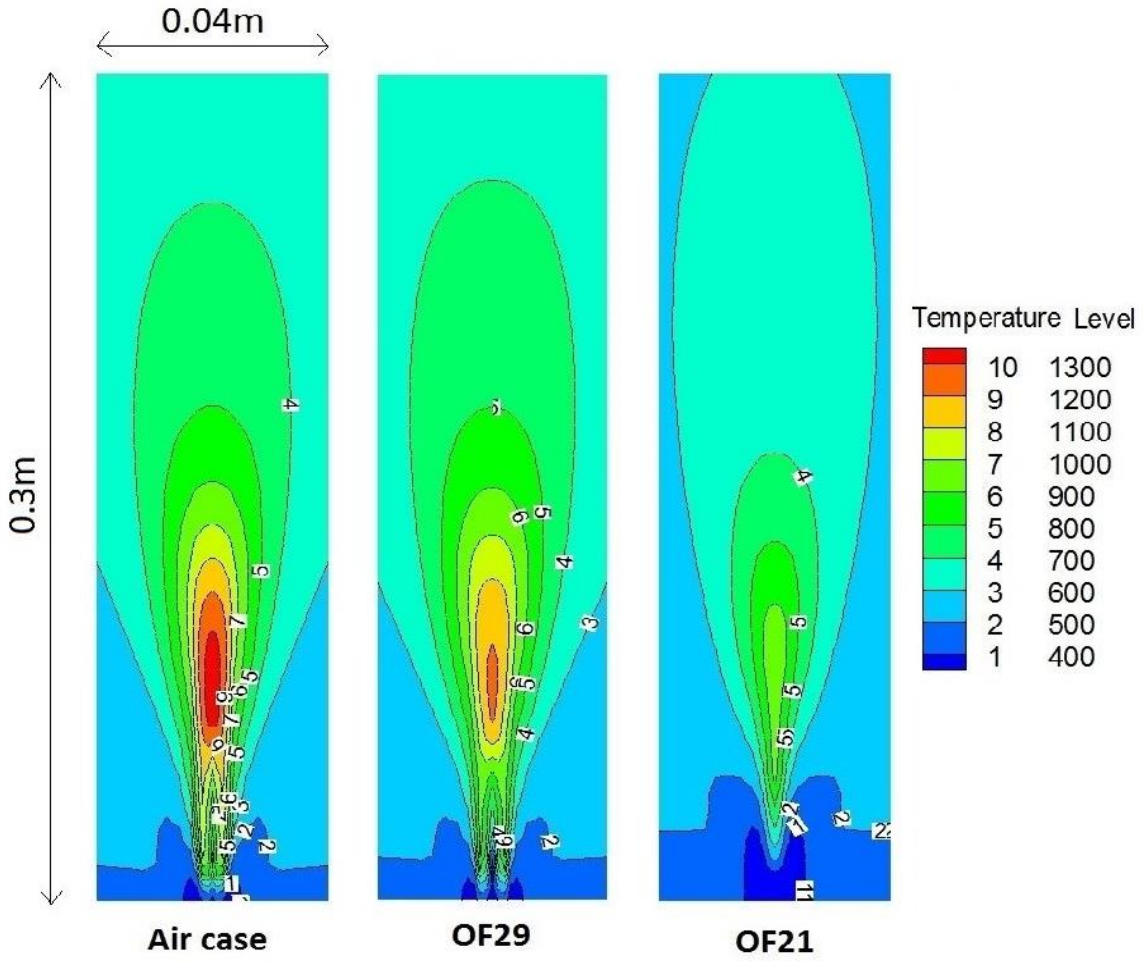

Figure 16. Comparison between the temperature (K) contours for the three cases including air, OF21, and OF29.

This may be attributed to the lowered combustion temperature in this case. Andersson and Johnsson [46] found an increase in the radiation intensity for oxygen-carbon dioxide environment, and this was attributed to the increased gas emissivity. However, the numerical results show approximately same radiation intensity for air case and OF29 case. This is because of comparatively higher temperature of air case, which seems to nullify the effect of higher gas emissivity of OF29 case. In all combustion cases, the peaks of the amount of radiation heat transfer are shifted from the temperature peaks. This can be justified from the flame shapes in Figure 16 and the velocity distribution in

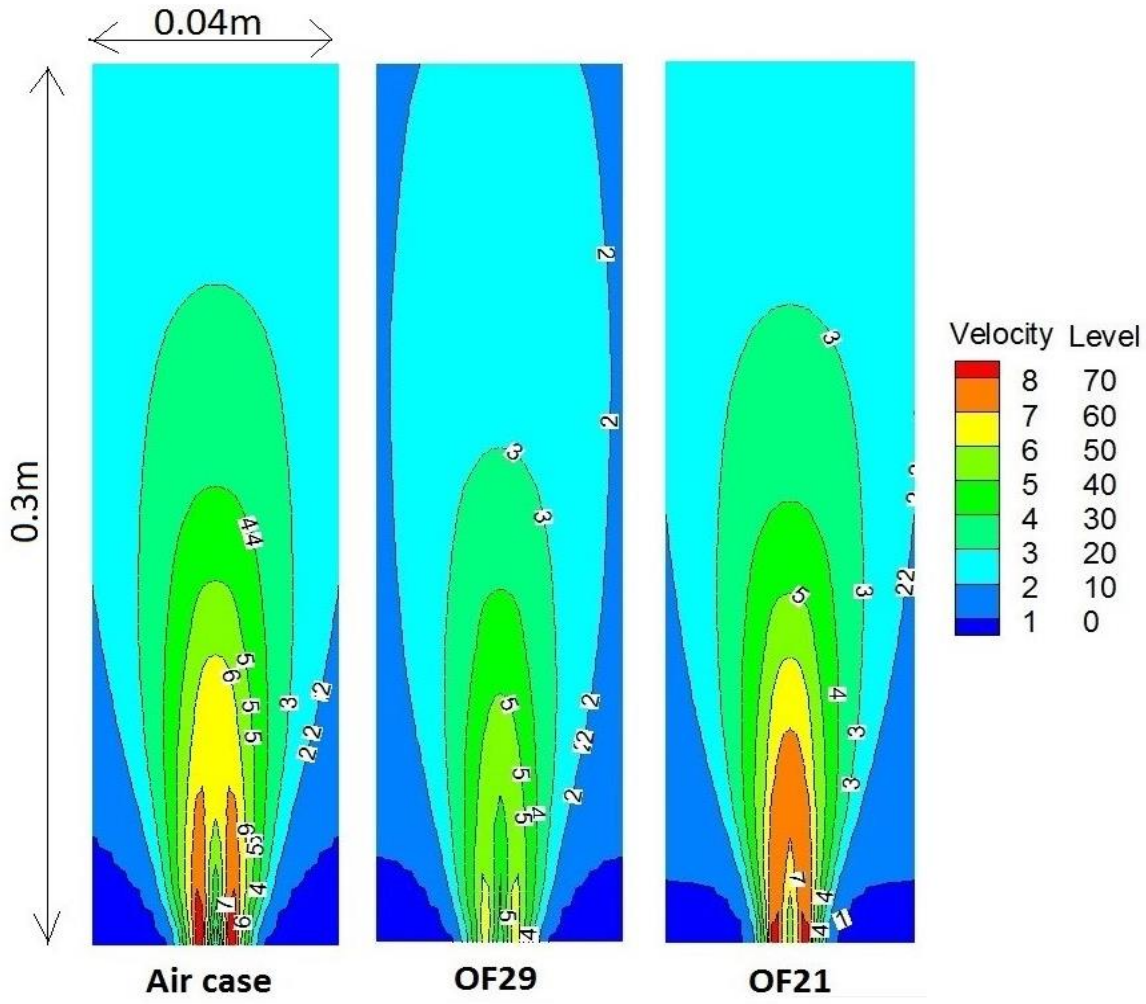

Figure 17. Comparison between the total velocity (m/s) contours for the three cases including air, OF21, and OF29.

Figure 17. Close to the inlet section, the velocity is maximum and the flame width is very tight. However, away from the inlet nozzle, the velocity is reduced and the fuel is evaporated so that, the size of the flame is extended toward the walls of the reactor. As a result, the amount of heat transfer by radiation is increased with height until the main combustion reactions of the fuel are vanished. The mass fraction distributions of both the fuel and the oxidizing oxygen are shown in Figure 19 (a) and Figure 19 (b), respectively. As shown in the figures, air and OF29 produces very similar distributions of the fuel and oxygen inside the reactor; however, the distribution is completely different in the case of OF21. Replacing nitrogen by carbon dioxide in case of OF21 should result in lowering the mass fractions of oxygen and fuel inside the reactor due to the higher molecular weight of CO_2 as compared to nitrogen. In all cases, the fuel is completely vaporized and burned at a height of 5 cm as shown in Figure 19 (a). Due to the higher molecular weight of CO_2, the mixing with the fuel and the combustion process is delayed as shown in Figure 20 (a). To investigate the effect of the replacement of nitrogen by CO_2 on the burning velocity and combustion temperature, the specific thermal capacity (ρC_p) profiles are presented in Figure 20 (b) through the reactor centreline for the three combustion cases. The figure shows that the specific thermal capacity of the combustion gases is higher in cases of oxy-combustion in a medium of CO_2 as compared to the air combustion case. Increasing the amount of CO_2 in the inlet oxidizer resulted in higher specific thermal capacity of the combustion products. As a result, the flame is cooled down and this may justify the lowered combustion temperature in the OF21 combustion case.

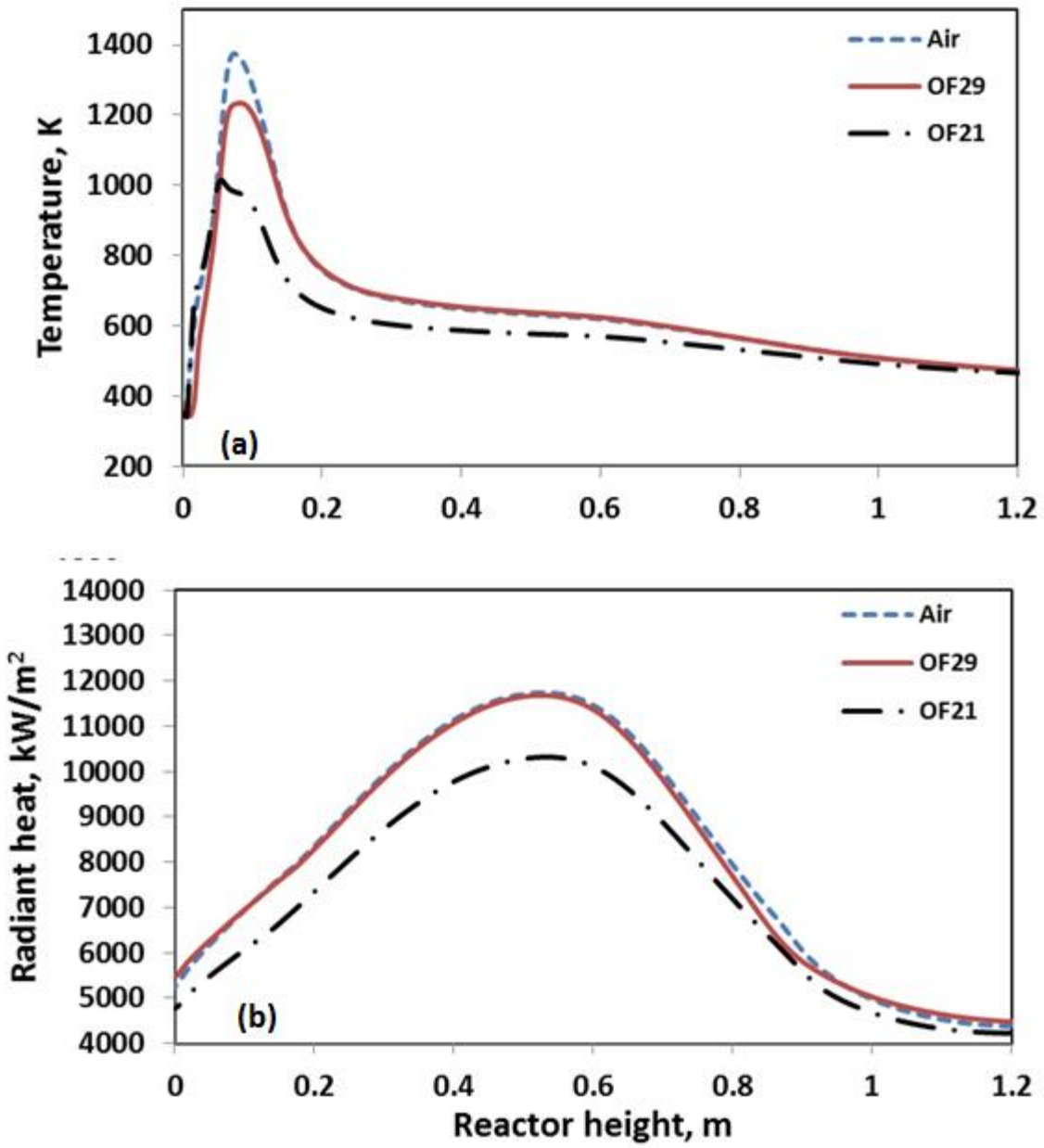

Figure 18. Comparison between the combustion characteristics in terms of (a) combustion temperature through the reactor centreline, and (b) absorbed radiant heat by the reactor wall through the reactor height, for the three cases including air, OF21, and OF29.

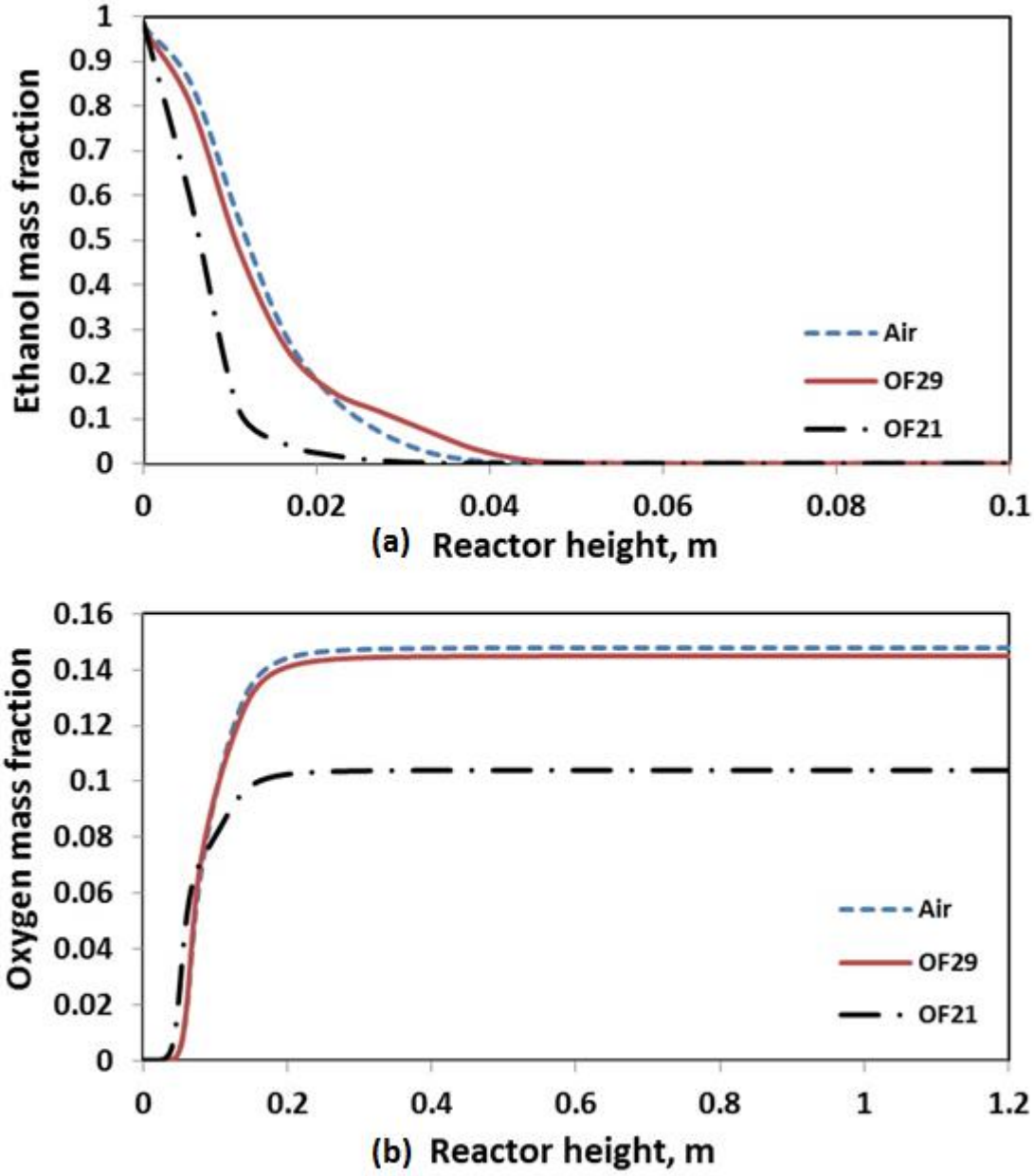

Figure 19. Comparison between the mass fractions distribution through the reactor centreline of (a) ethanol, and (b) oxygen, for the three cases including air, OF21, and OF29.

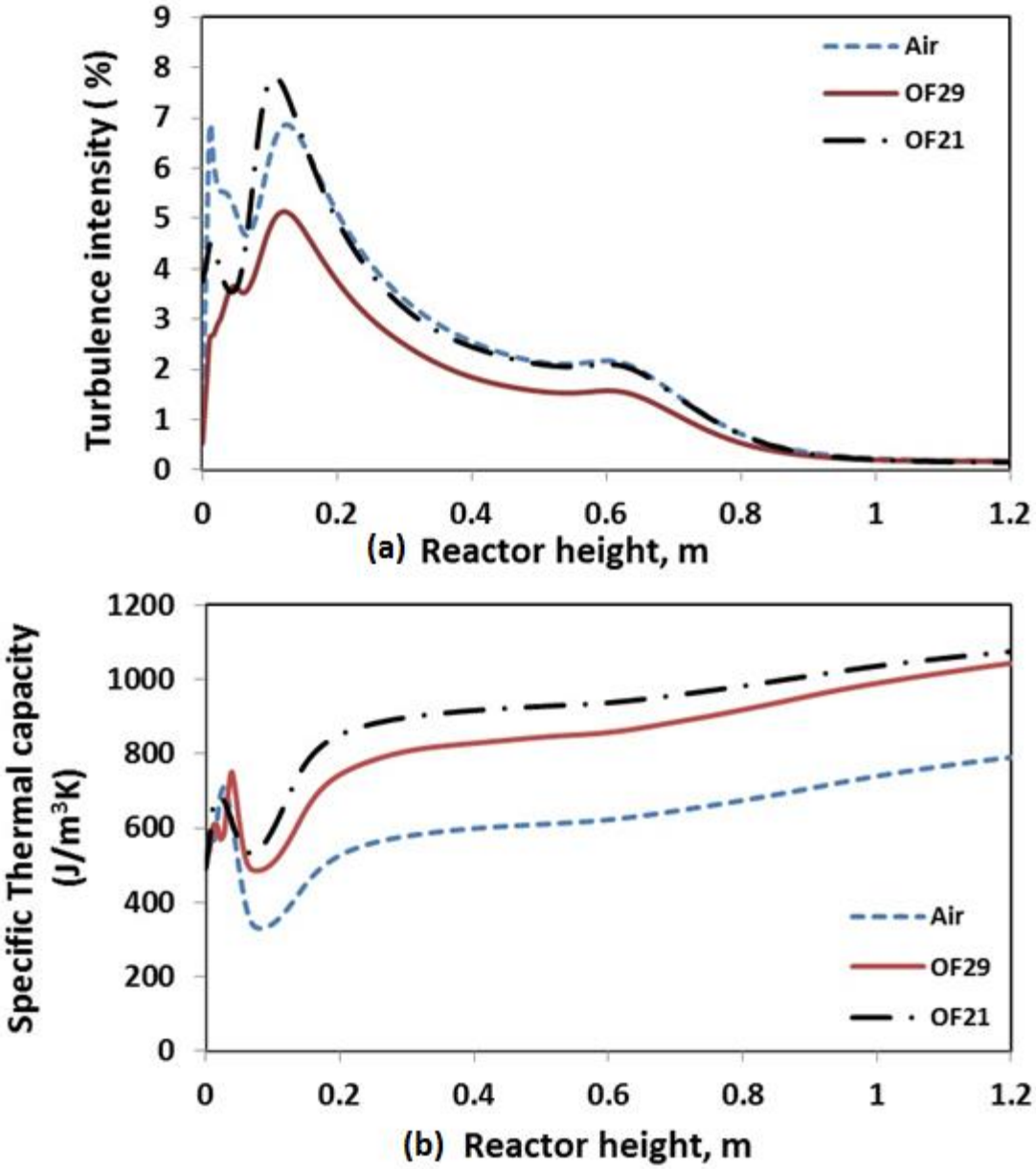

Figure 20. Distributions of (a) turbulence intensity, and (b) specific thermal capacity along the reactor centreline for different combustion cases including air, OF21, and OF29.

4.1.3 Effect of Soot on Radiation

In this section, OF 29 case is incorporated with one step Khan and Greaves soot model and the effect is compared with OF 29 case neglecting the soot model. Figure 21 (a) and Figure 21 (b) shows the temperature profile at the centreline and incident radiation on the reactor wall through the reactor height, respectively. It can be seen that there is negligible effect of soot model on both temperature and radiation profile in ethanol combustion. This is due to the fact that there is little soot formation during the combustion in OF 29 case and apparently it doesn't have any effect on the combustion characteristics. There can be two reasons for the same: (a) Ethanol is a light fuel & (b) Combustion is taking place in abundance of oxygen with equivalence ratio of 0.4. Ethanol has a lower temperature of vaporization and also has oxygen content in the form of OH radical. This causes an efficient burning of ethanol without or very little soot formation in the combustion at normal pressure [81]. In addition to that, it has been observed that soot formation can be significantly reduced if combustion is taking place in carbon dioxide environment. Figure 22 shows the formation of soot in the three cases, namely air case, OF 21 and OF 29. We can see that soot formation is almost negligible for OF 21 case while highest for air case. This trend has also been observed by Andersson et al. [50] in their investigation of propane-fired oxy-fuel flames. OF 21 has negligible soot formation as it has the highest carbon dioxide content. As, the carbon dioxide content is reduced in OF 29 case, soot formation increases and air case with lowest carbon dioxide content has highest soot formation. Thus, it can be concluded that presence of carbon dioxide in the reactor significantly affect the formation of soot.

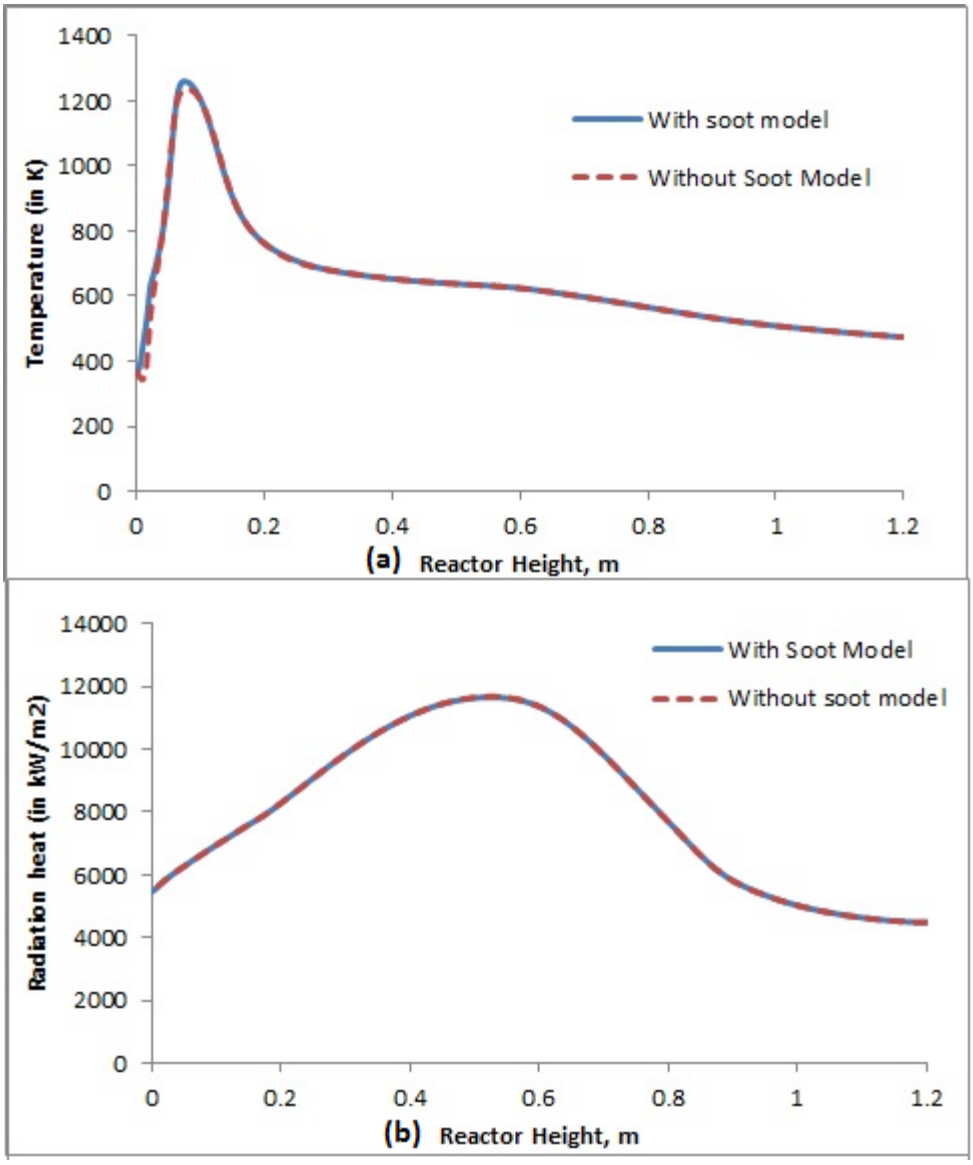

Figure 21. Comparison between the combustion characteristics in terms of (a) combustion temperature through the reactor centreline, and (b) absorbed radiant heat by the reactor wall through the reactor height, for OF29 with soot model and without soot model

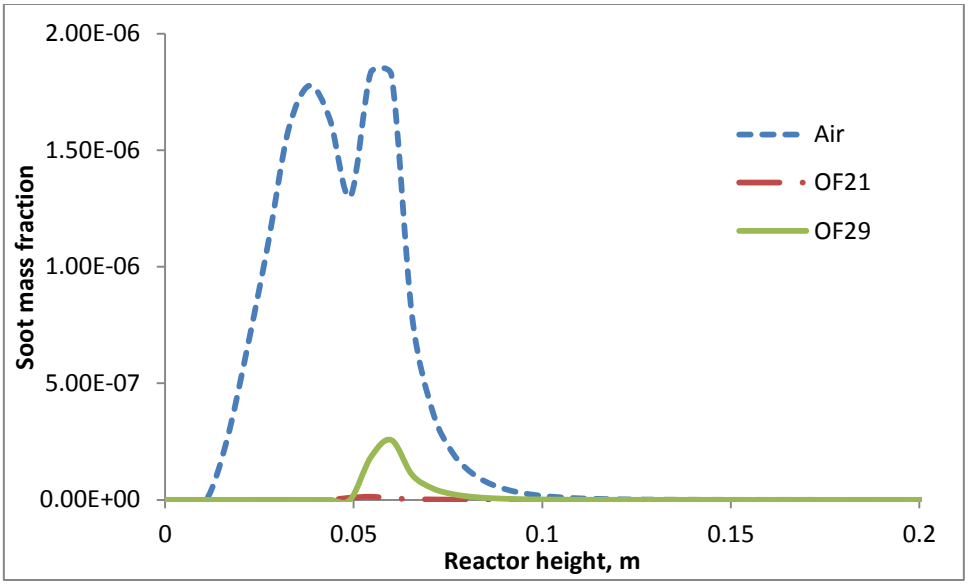

Figure 22. Comparison of soot mass fraction along centreline of the reactor for air case, OF 21 case and OF 29 case.

4.2 Heavy Fuel Oil Combustion in the Boiler

Combustion of heavy fuel oil inside the furnace of a water tube boiler has been modeled using the mathematical formulations described in the previous sections. The boiler geometry has been shown in the Figure 7 and the composition of heavy fuel oil is given in Table 1. The case was extended to study (i) effect of dilution of oxidizer stream with carbon dioxide and its comparison with the combustion in pure air, (ii) effect of droplet diameter on the combustion characteristics and (iii) effect of swirl number on the combustion characteristics.

4.2.1 Effect of Dilution of the Oxidizer with Carbon dioxide

In this section, combustion of the liquid fuel is simulated for the three cases (i) Air case (21 % O_2 and 79 % N_2 by volume), (ii) OF21 (21% of O_2 and 79 % of CO_2 by volume) and (iii) OF29 (29% of O_2 and 71% of CO_2 by volume). Figure 23 and Figure 24 show the temperature profiles along the x-axis for the two burners (Burner 1 at the height of 2.198 m and Burner 2 at the height of 4.662 m). It can be seen that the temperature level is lower for OF21 case but very similar for air case and OF29 case. Maximum temperature levels for the air case and OF29 case are nearly same in contrast to OF21 case, which is significantly lower. We can see that the temperature rises slowly near the burners for OF21 and OF29 cases in comparison to the air case. This suggests that replacement of nitrogen with carbon dioxide slows down the reaction rate, and consequently there is a combustion delay in carbon dioxide environment. Moreover, there are some fluctuations in the temperature profiles near the burners, however, these

fluctuations die further downstream. This is because of the fact that the fuel droplets are discrete in nature and evaporates as individual entities. Thus, the concentration of fuel is dispersed inside the furnace and burning is not so continuous near the burners. Further, the flow has swirl and is highly turbulent which adds to the fluctuations of scalar quantities. However, as the distance from the burners increases, the droplets completely vaporize and diffuse in the stream causing a homogeneous air-fuel mixture and thus smooth profiles are observed. Axial profile through the upper burner (Figure 24) shows that the maximum temperature level is achieved earlier for the air case than for OF29 case. This is because of faster reaction rate in air combustion as compared to that of in carbon dioxide environment. However, for the lower burner (Figure 23), maximum temperature level is reached earlier for OF29 case. Higher temperature level for OF29 case at lower burner can be explained by considering the effect of buoyancy in the two cases. It is evident that upward bending of the flame is more prominent in carbon dioxide environment due to higher buoyant force (Figure 27). Thus, along the axial profile for the lower burner in case of OF29, upward bending of the flame causes a shift in the peak temperature position towards the upstream.

Figure 25 and Figure 26 show the temperature contours for the horizontal plane at upper and lower burners respectively. It can be seen that for the air case temperature distribution is more uniform while for OF21 and OF29 cases temperature level is higher for the upper burner (Burner 2). This is more apparent from Figure 27, which shows the temperature contours for the vertical plane through both the burners. We can see that the flames for OF21 and OF29 cases are lifted upward much more than that of the air case. This causes a more non-uniform temperature distribution in the carbon dioxide

environment. Upward lifting of flames is due to the buoyancy effect which is more significant in a carbon dioxide environment because of higher molecular weight of carbon dioxide as compared to nitrogen. Hence, for a horizontal reactor, as in case of this boiler, replacement of nitrogen with carbon dioxide can greatly affect the temperature distribution inside the reactor. Figure 28 shows the temperature contour for the vertical plane at a distance of 2.24 m from the burners. We can see that for the reactor part (right part of the figure), temperature level is higher in the air case than in OF29 case, which means that the reaction rate is faster in the air case as discussed earlier. However, for the heater part (left part of the figure), temperature level for air case is lower and more uniform than for OF29 case.

Figure 29 shows the trajectories of fuel droplets for the three cases. It can be seen that the droplets get completely evaporated very close to the burners and change of the combustion environment doesn't have much effect on the evaporation rate. This is apparently because of lower vaporization temperature (which is less than 340 K) of the fuel.

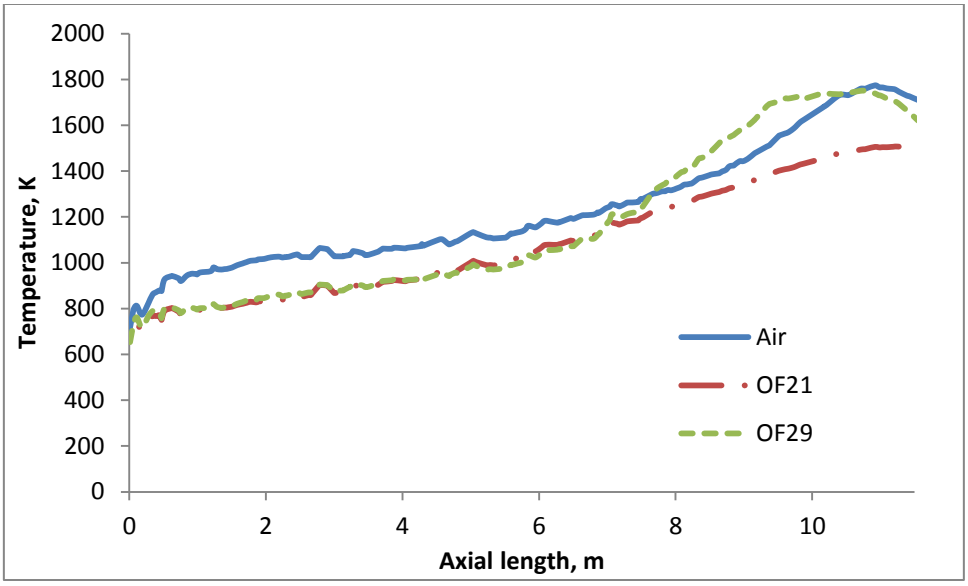

Figure 23. Temperature distribution along the axis of burner 1 (z=2.198 m)

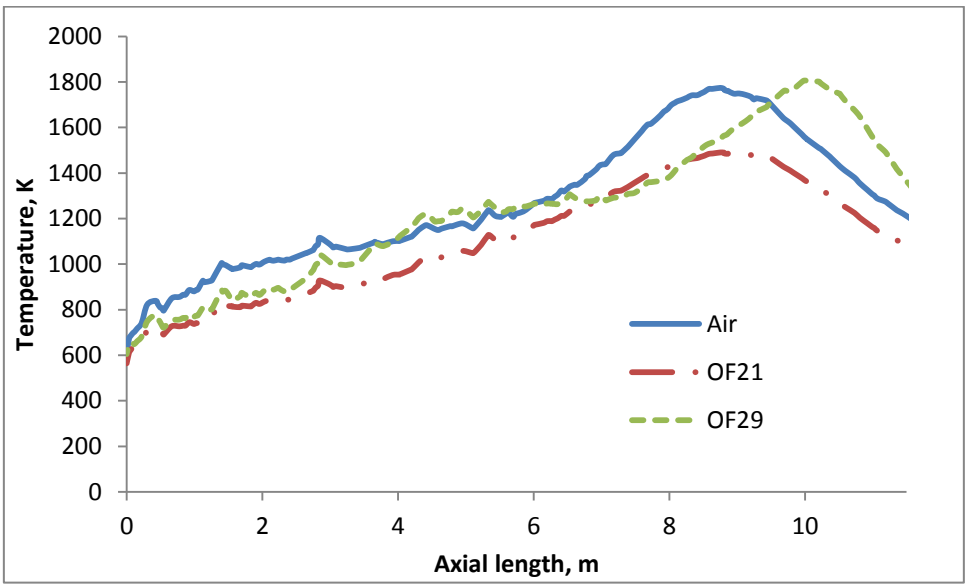

Figure 24. Temperature distribution along the axis of burner 2 (z=4.662 m)

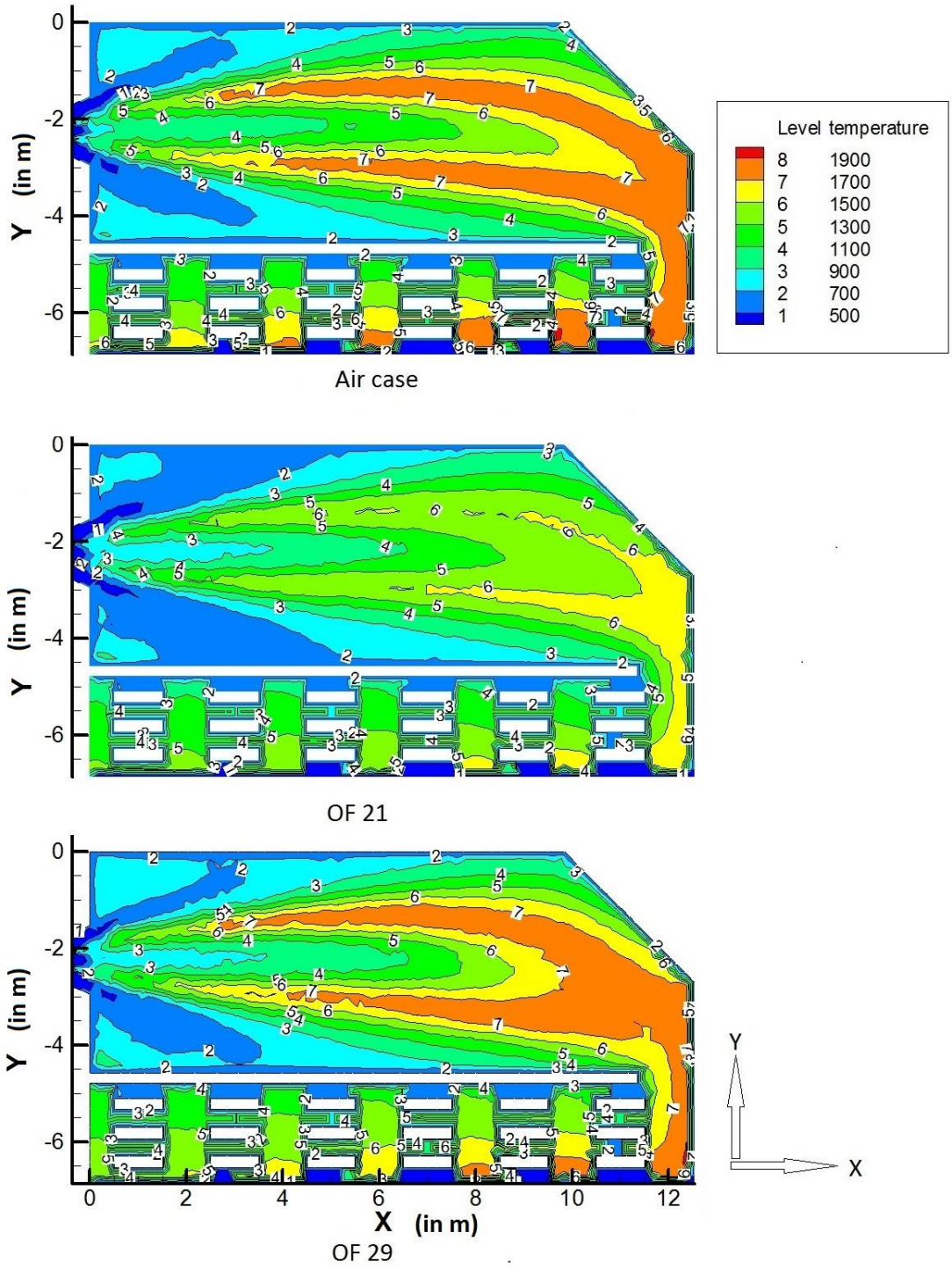

Figure 25. Temperature (K) contours for horizontal plane at z=2.198 m

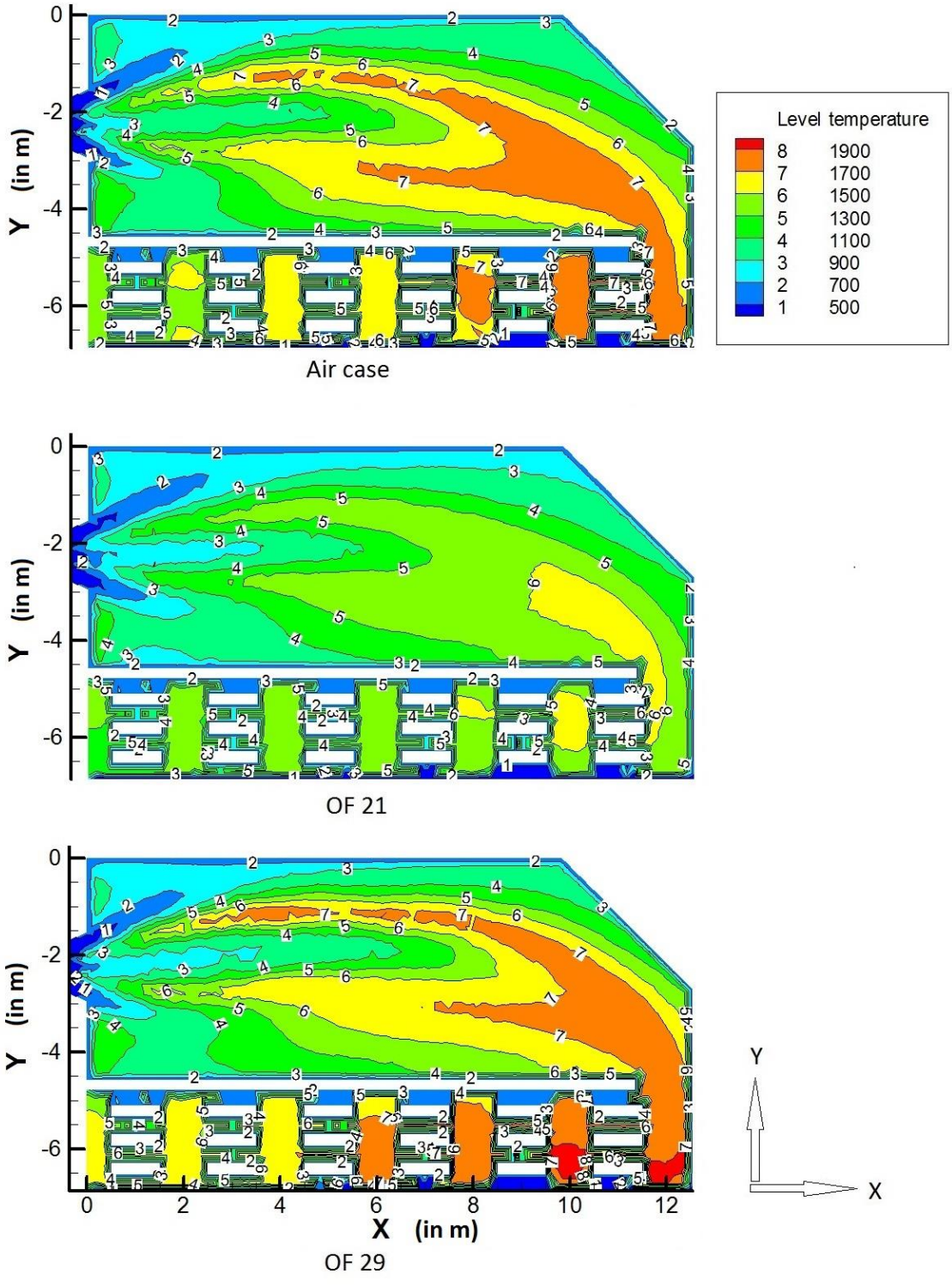

Figure 26. Temperature (K) contours for horizontal plane at z=4.662 m

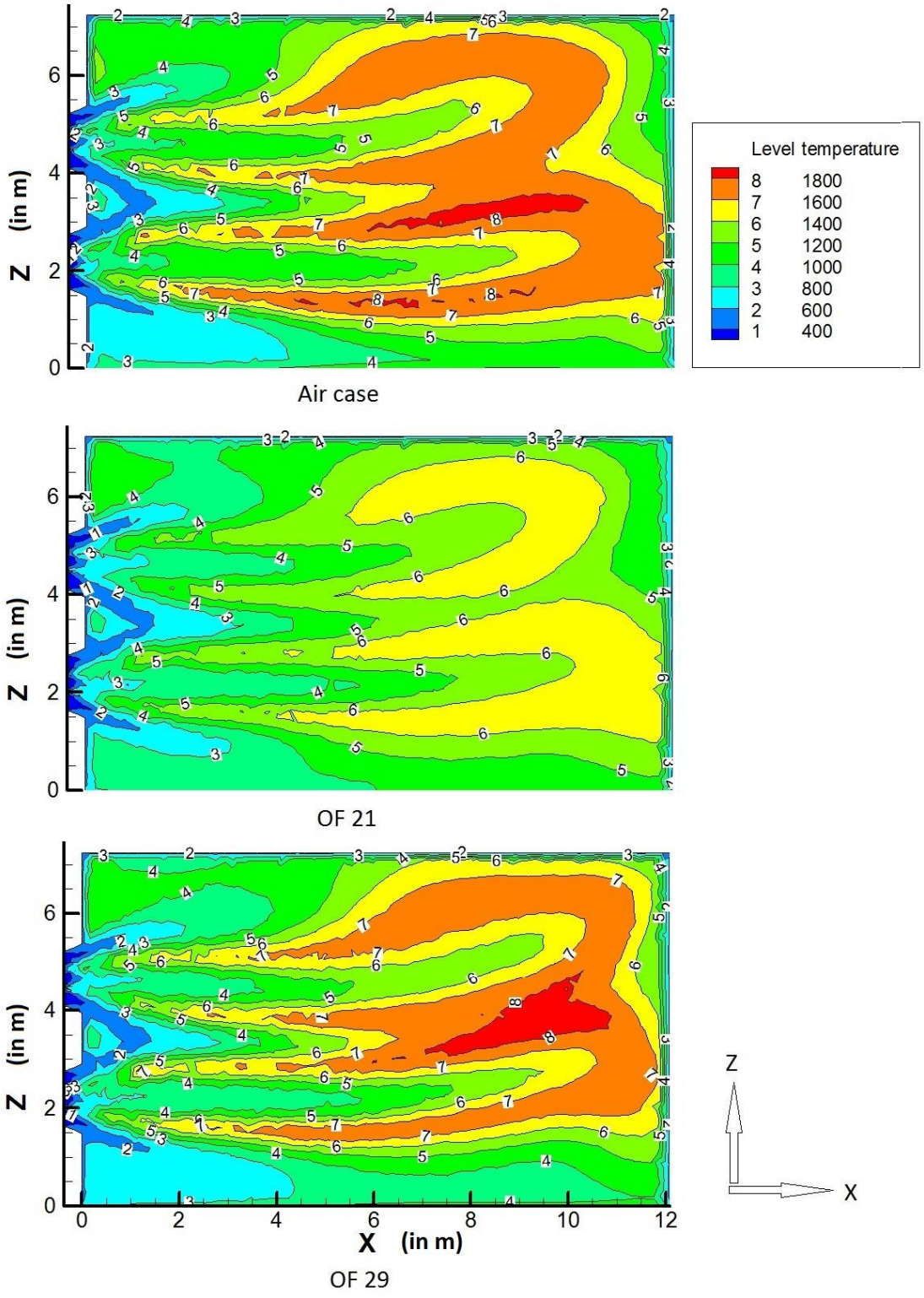

Figure 27. Temperature (K) contours for vertical plane at y=-2.24 m

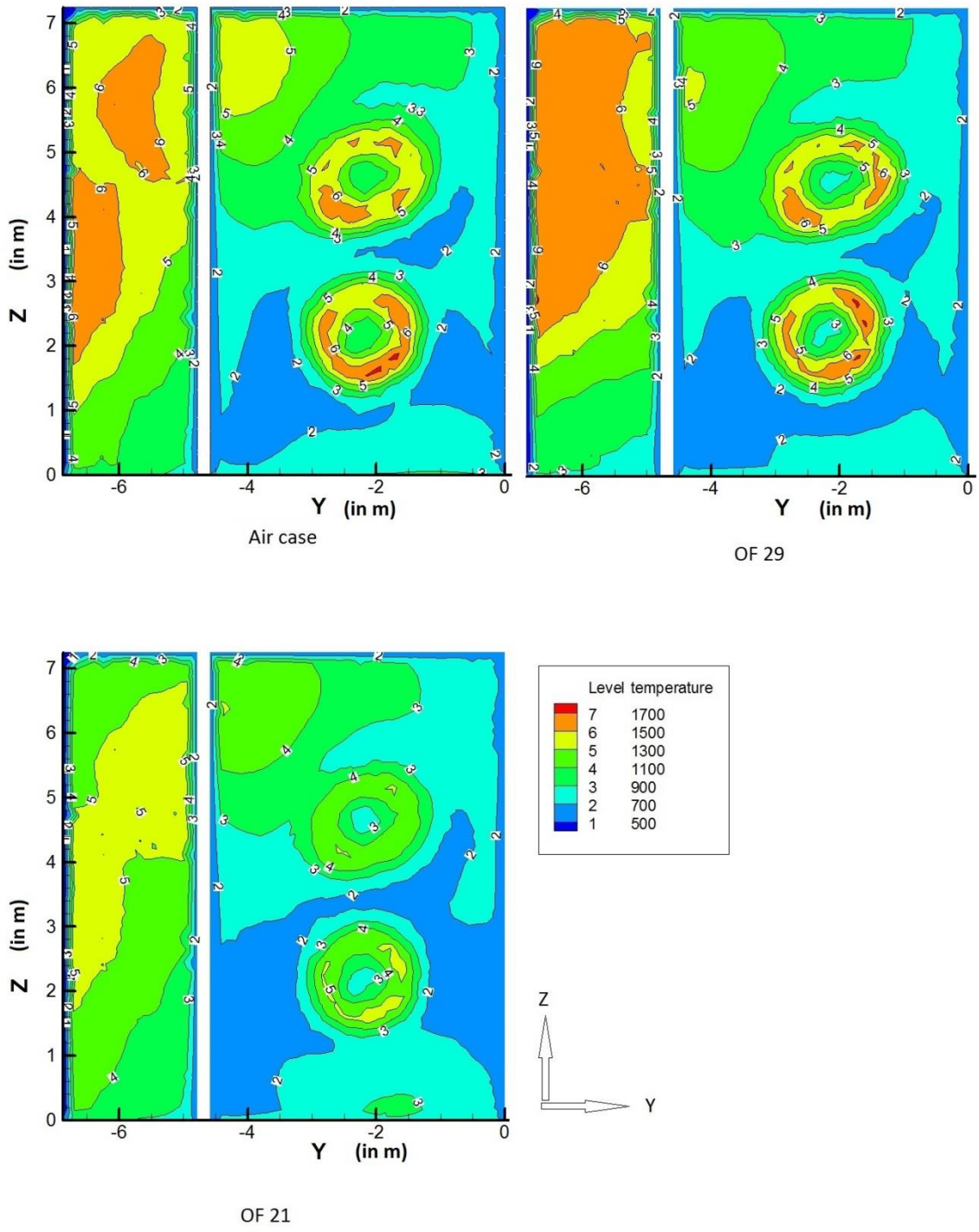

Figure 28. Temperature (K) contours for vertical plane at x=2.24 m

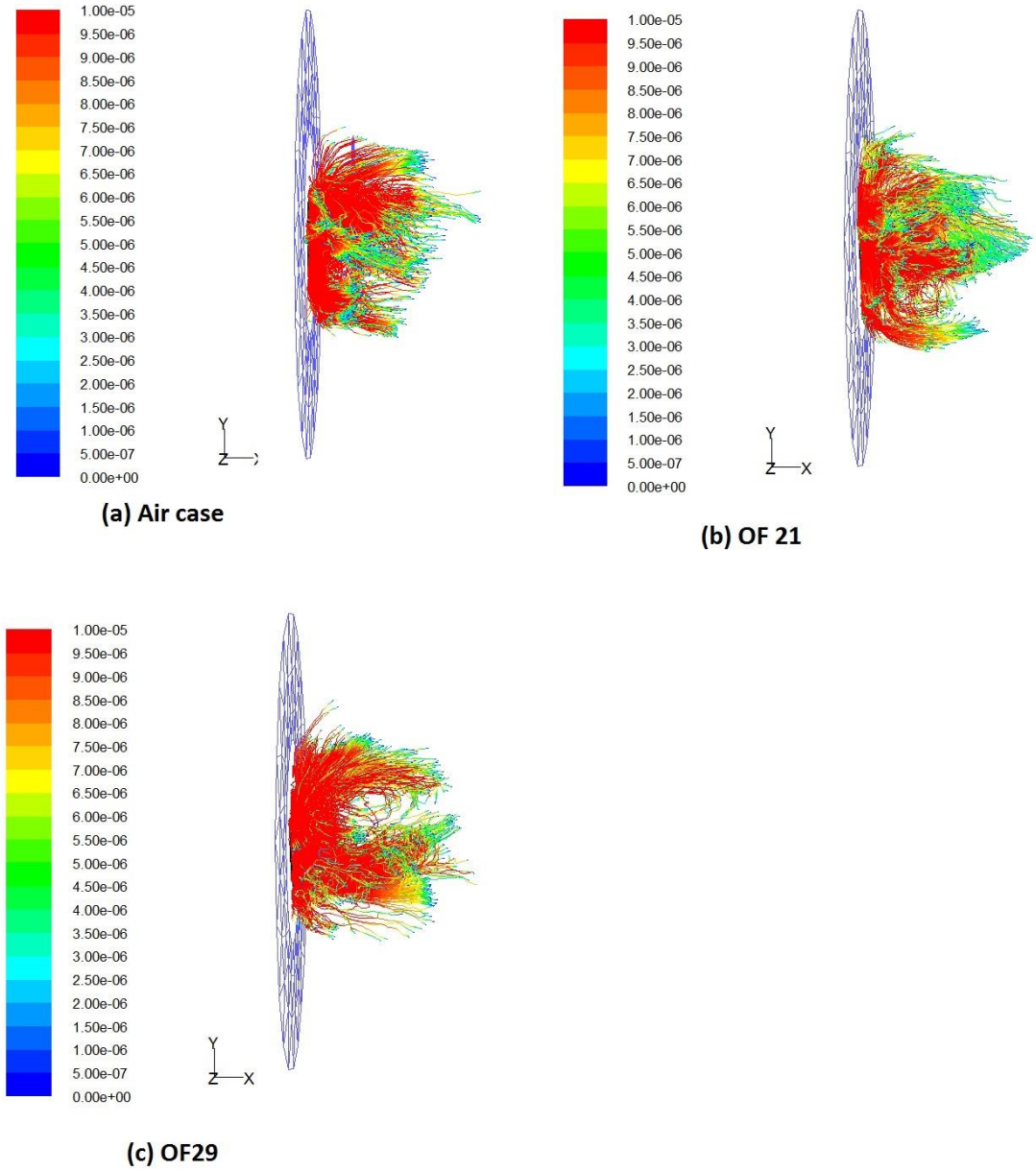

Figure 29. Trajectory of droplets with diameter (in m)

Figure 30 and Figure 31 show the axial velocity profile along the lower and upper burners respectively and Figure 32 shows the velocity contour for the vertical plane containing the two burners. It can be seen that the velocity magnitude for the air case and OF21 case is higher than that of OF29 case. In order to maintain same oxygen flux into the boiler, volume flow rate of the oxidizer stream for OF21 case is kept same as that of the air case, while for OF29 case it is reduced because of the fact that CO_2 has higher molecular mass than N_2. Thus, the velocity level for OF29 case is much lower than that of the other two cases. Also, velocity levels for the air case are slightly higher than that of OF21 case because of higher temperature and combustion rate in the former case, which accelerates the fluids in the vicinity. Further, we can see that for the air case, velocity contour is wider than that of OF21 case near the burners. Evidently, this is because of the fact that reaction rate in air case is faster than that of in carbon dioxide environments as has been discussed in the previous section. Thus, higher temperature levels near the burners in the air case expand the surrounding fluids and cause higher velocity magnitudes.

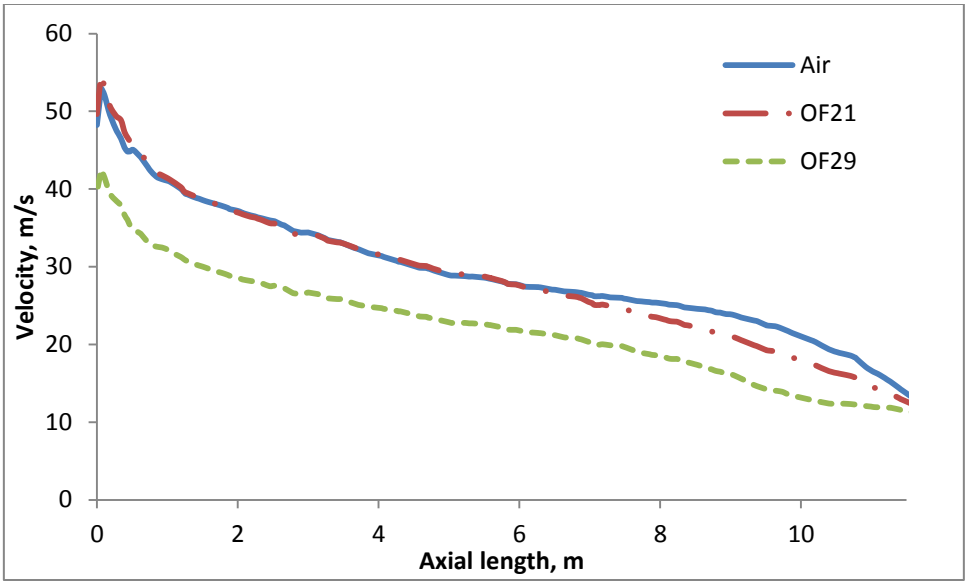

Figure 30. Velocity along the axis of burner 1 (z=2.198 m)

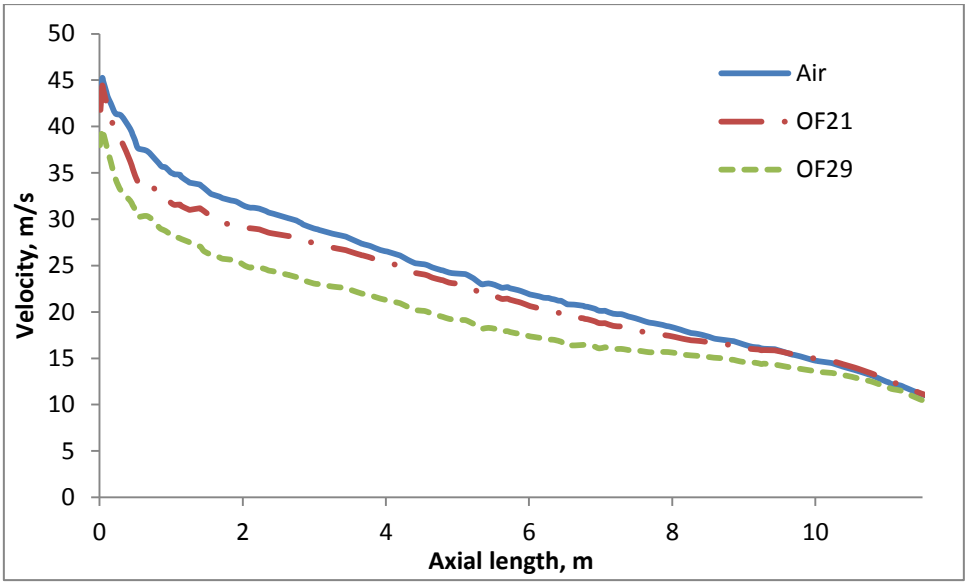

Figure 31. Velocity along the axis of burner 2 (z=4.662 m)

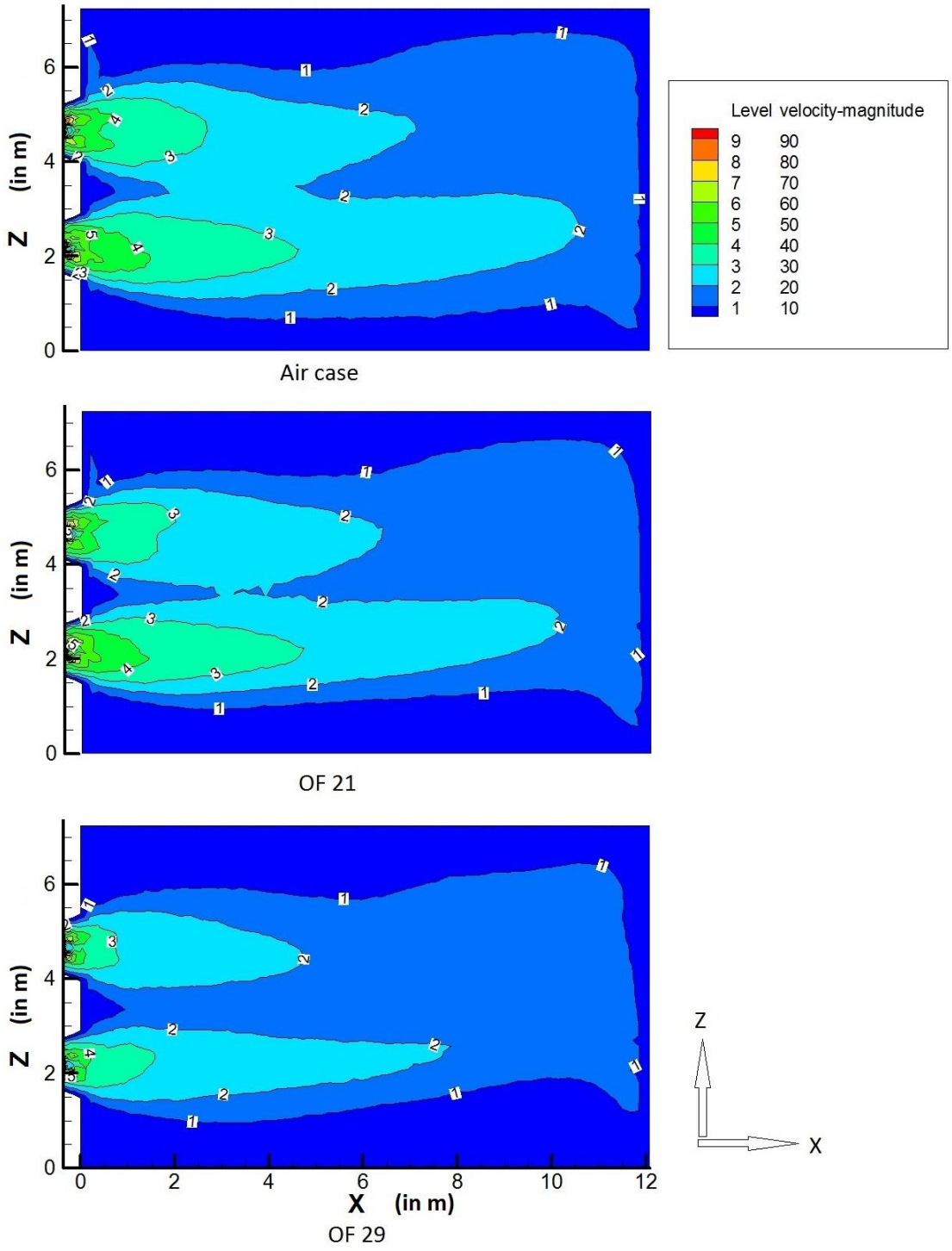

Figure 32. Velocity (m/s) contours for vertical plane at y=-2.24 m

Figure 33 and Figure 34 show the turbulent intensity profile along the x-axis from the lower and upper burner respectively. We can see that the turbulent intensity for the air case and OF21 case follows the same trend while for OF29 case it is significantly lower. This is because of lower tangential component of the velocity in OF29 case than both the other cases, which means lower turbulence. Turbulent intensity decreases downstream as moving away from the burners and then rises again near the end of the reactor. Initial decrease corresponds to the dissipation of turbulent energy along the flow which reduces the magnitude of turbulence. However, near the reactor end, velocity magnitude of the fluid reduces as it makes its way to the tube bank. Remembering that the turbulent intensity is the percentage of turbulent component to the velocity magnitude, a decrease in velocity near the reactor end means higher percentage of turbulent component in the stream. Figure 35 shows the contour of turbulent intensity in the vertical plane and confirms the same trend. Lower turbulent intensity for OF29 case causes slower mixing of fuel with oxygen, which eventually results in slower reaction rate and delayed combustion, as has been observed in the previous section. Thus, even with higher molar concentration of oxygen in OF29 case, the combustion process is slower than that of the air case because of the lower turbulent intensity.

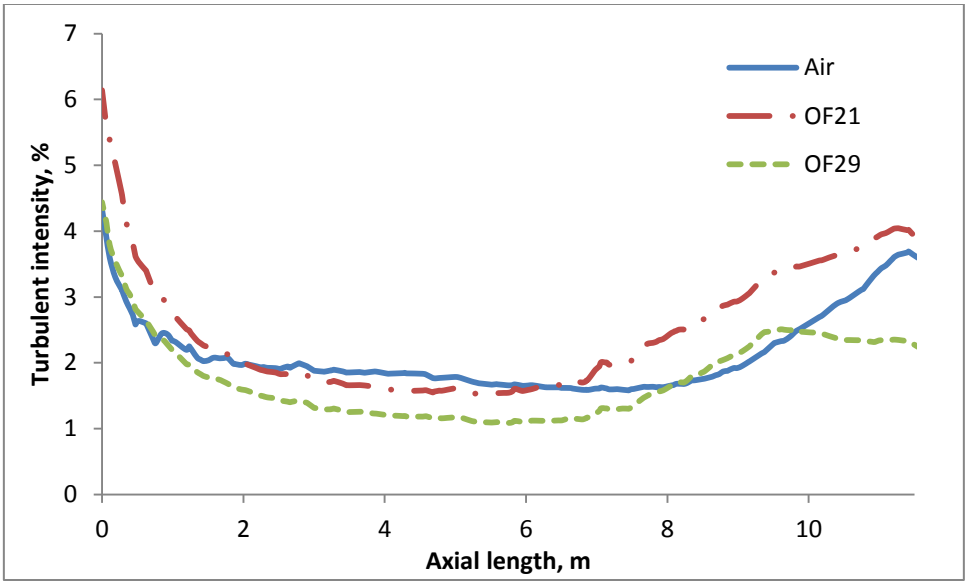

Figure 33. Turbulent Intensity along the axis of burner 1 (z=2.198 m)

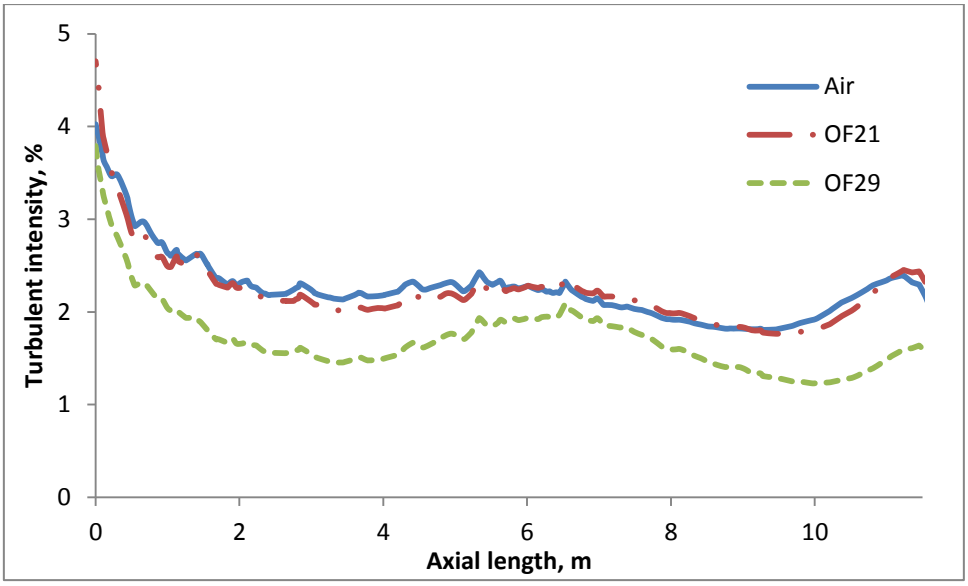

Figure 34. Turbulent Intensity along the axis of burner 2 (z=4.662 m)

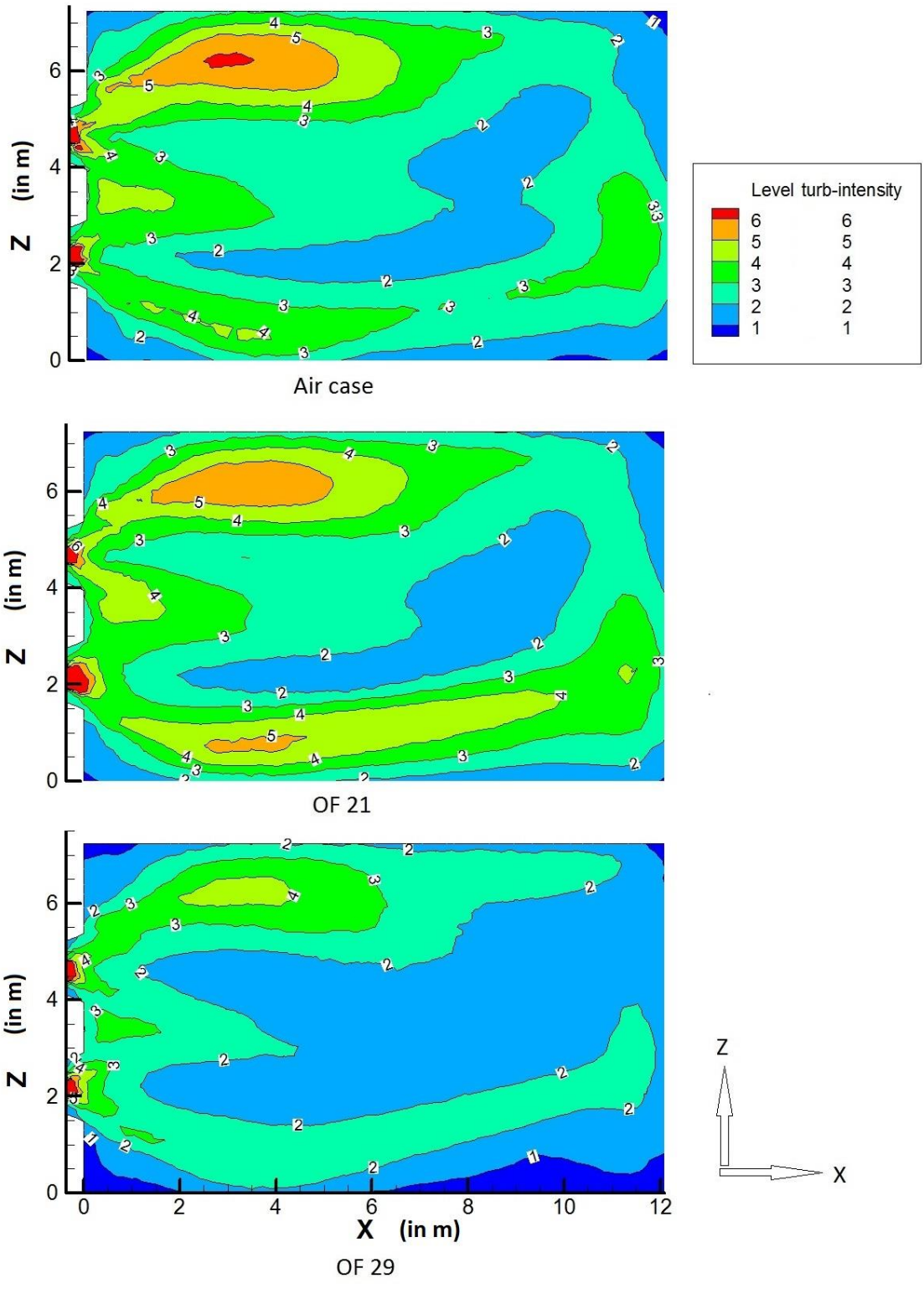

Figure 35. Turbulent intensity (%) contours for vertical plane at y=-2.24 m

Figure 36 and Figure 38 show the turbulent viscosity level for the three cases. We can see that turbulent viscosity for the air case and OF29 case is in the same range, however, it much higher for OF21 case. As, nitrogen is replaced by carbon dioxide, turbulent viscosity of the gases increases significantly (OF21) and decreases with decrease in the percentage of carbon dioxide (OF29) in the combustion environment. From the contours (Figure 38) it is apparent that the turbulent viscosity is lower in the high velocity regions. This explains why turbulent viscosity is more uniform for OF29 case than for the air case, as we know that the velocity level for OF29 case is lower than the latter case to ensure equal mass influx of oxygen in the reactor. Also, it is clear from the plots (Figure 36 and Figure 37) that the turbulent viscosity increases near the end of reactor for all the three cases because of lower velocity level near the reactor wall. Turbulent viscosity is related to the turbulent kinetic energy. Thus, it explains that for OF29 case lower turbulent viscosity reduces mixing of gases and thus the reaction rate.

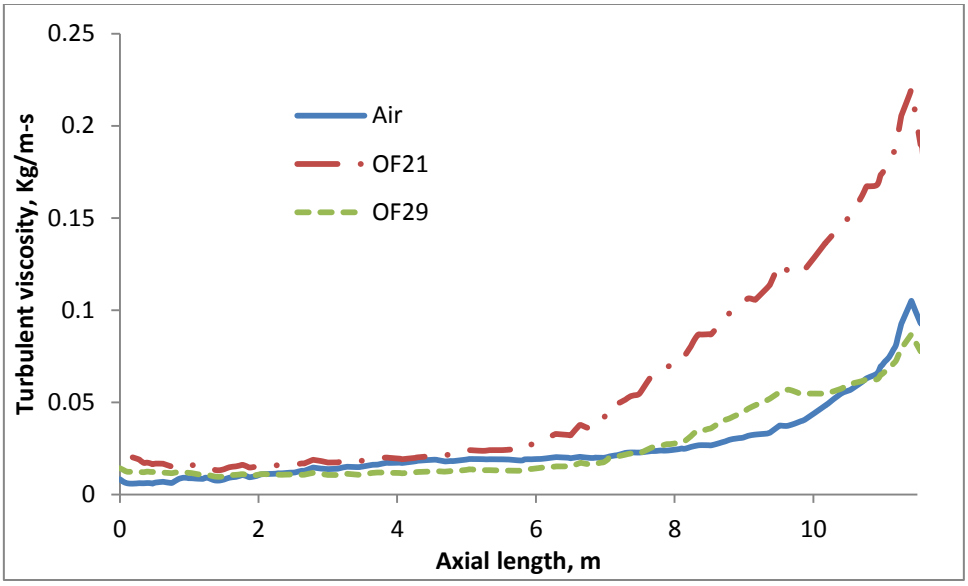

Figure 36. Turbulent Viscosity along the axis of burner 1 (z=2.198 m)

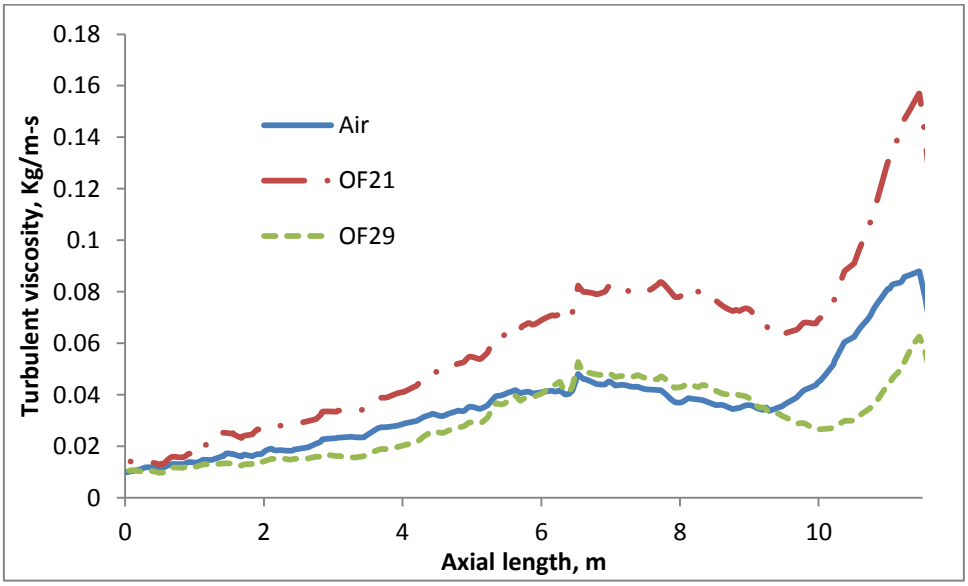

Figure 37. Turbulent Viscosity along the axis of burner 2 (z=4.662 m)

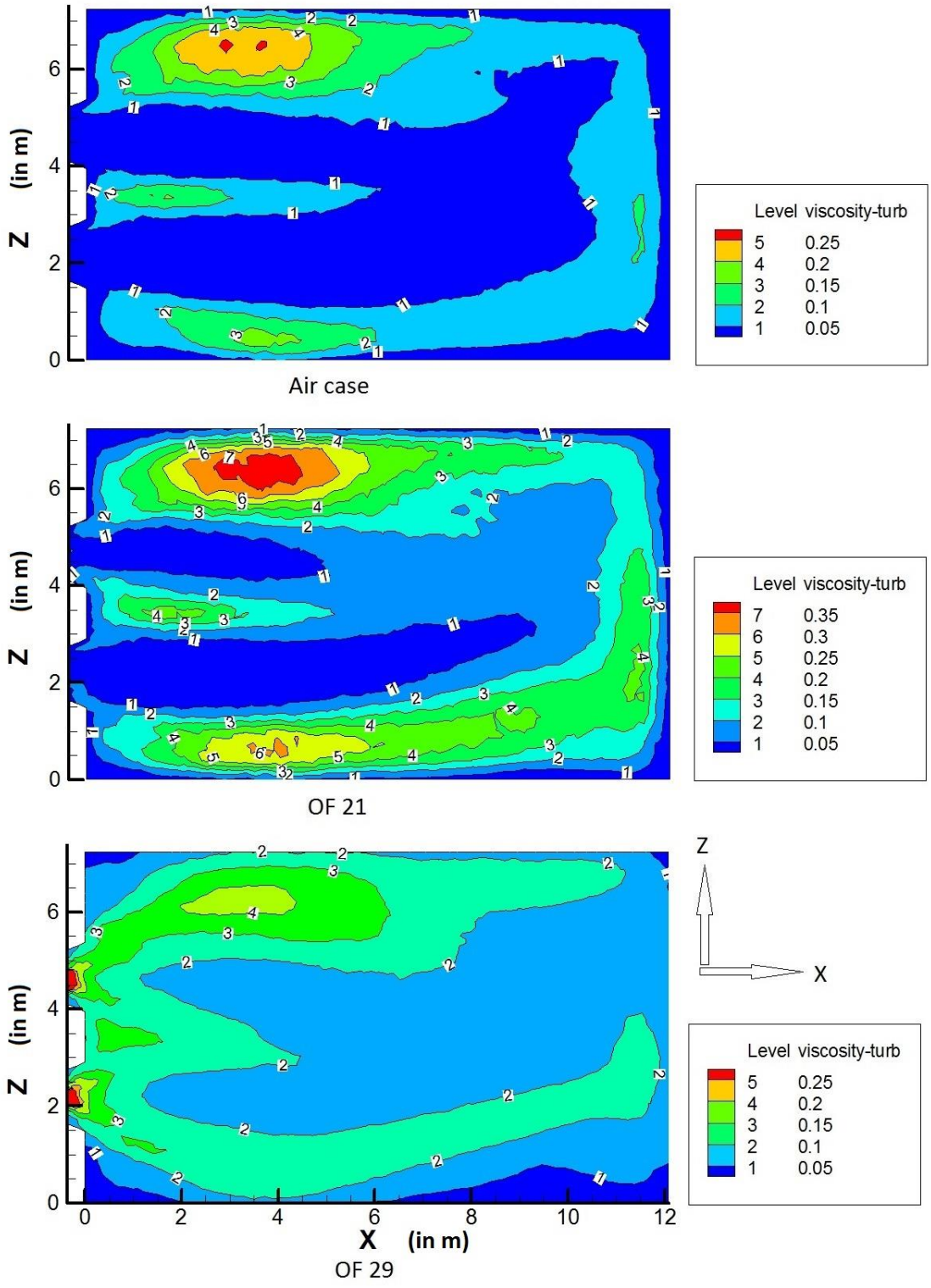

Figure 38. Turbulent viscosity (kg/m-s) contours for vertical plane at y=-2.24 m

Figure 39 and Figure 40 show the axial profile for specific heat capacity along the lower and upper burners respectively. We can see that the specific heat capacity increases with the replacement of nitrogen with carbon dioxide and further increases with the increase in carbon dioxide percentage in the oxidizer stream. This is due to the fact that CO_2 has higher heat capacity than N_2. Thus, temperature level for OF21 case is the lowest among the three cases because of highest CO_2 percentage in the oxidizer stream. Also, the specific heat capacity is higher near the burners and decreases downstream along the length of the reactor for all the three cases. This can be explained due to the presence of various intermediate species in the reaction zone near the burners which are eventually consumed and the gases mixtures are more homogeneous in the downstream. This trend was also observed in the previous works [44].

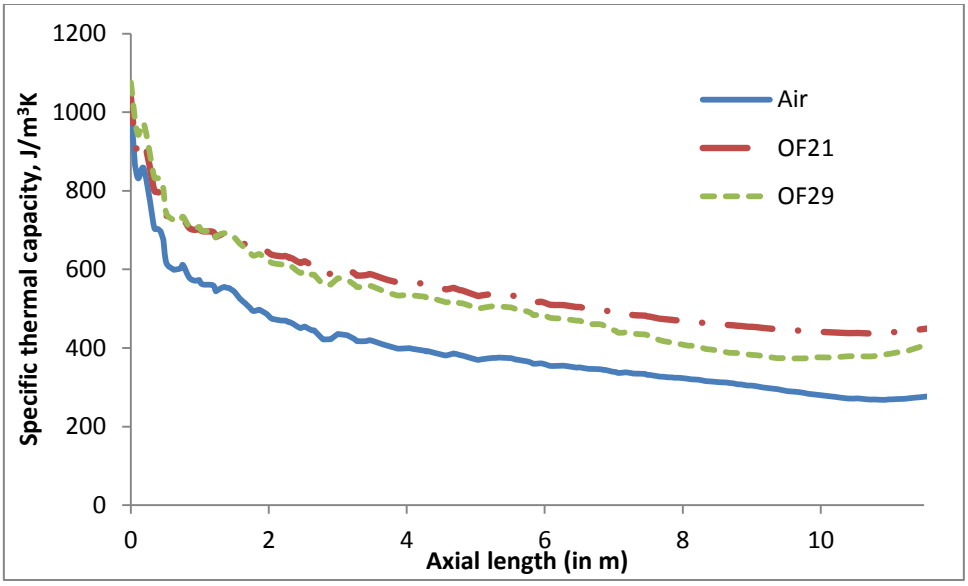

Figure 39. Specific thermal capacity along the axis of burner 1 (z=2.198 m)

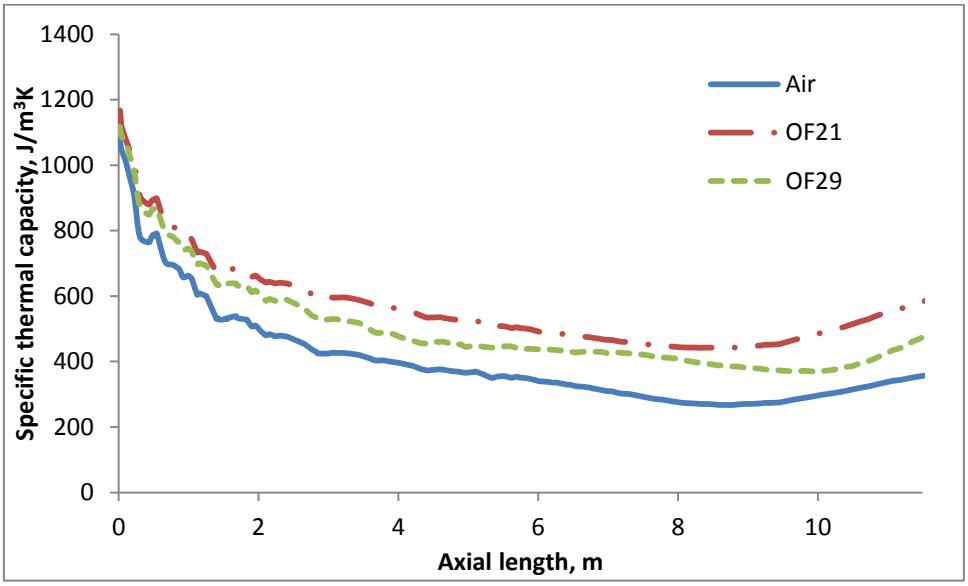

Figure 40. Specific thermal capacity along the axis of burner 2 (z=4.662 m)

Figure 41 to Figure 64 represent the mass fraction of various species for the three cases. Combustion mechanism in CO_2 environment differs significantly from that of in the air. It is observed that intermediate hydrocarbon species like C_2H_4, C_6H_6 and CH_4 are broken and consumed quickly in CO_2 environment than in air combustion. Figure 41 and Figure 42 show the mass fraction of C_6H_6 along the x-axis for both the burners. It can be seen that longer carbon chains breaks quickly in the carbon dioxide environment while for air the case it is slower. Further, carbon dioxide reduces the production of intermediate carbon chains as can be seen from Figure 47 and Figure 48. A significant amount of intermediate carbon compound, C_2H_4, is produced in the air case while for OF21 and OF29 cases it is negligible. This shows that longer chains break directly into smaller components in the carbon dioxide environment, while in air case intermediate carbon chains are formed. Hence, the concentration levels of smaller component, CH_4, follow the same pattern for the air case and OF29 case as can be seen from Figure 44 and Figure 45. However, for OF21 case we see higher concentrations of CH_4 near the burners than both the other cases, but soon it breaks down and is consumed faster than the latter cases. This is because of higher percentage of carbon dioxide present the combustion environment which enhances the breakdown of carbon compounds.

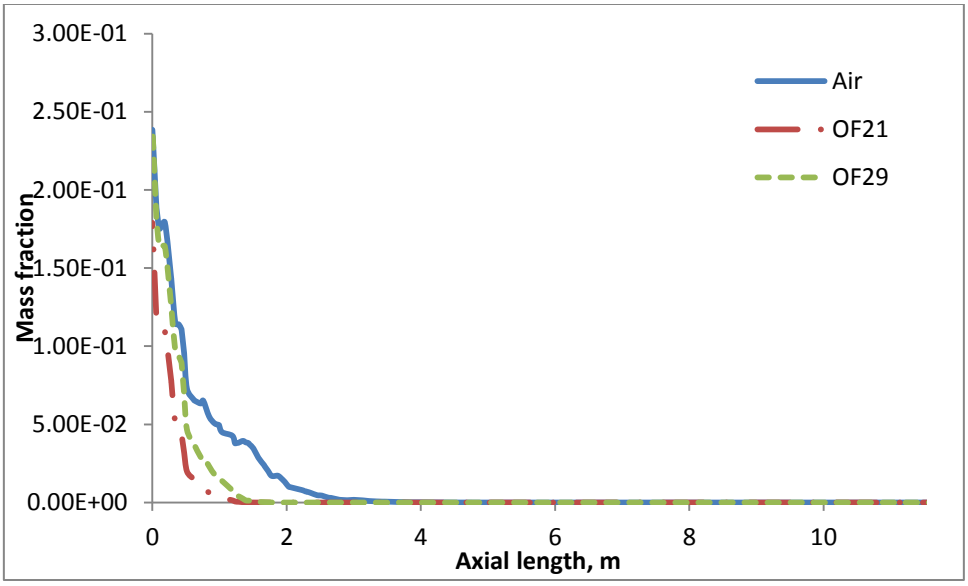

Figure 41. Mass fraction of C_6H_6 along the axis of burner 1 (z=2.198 m)

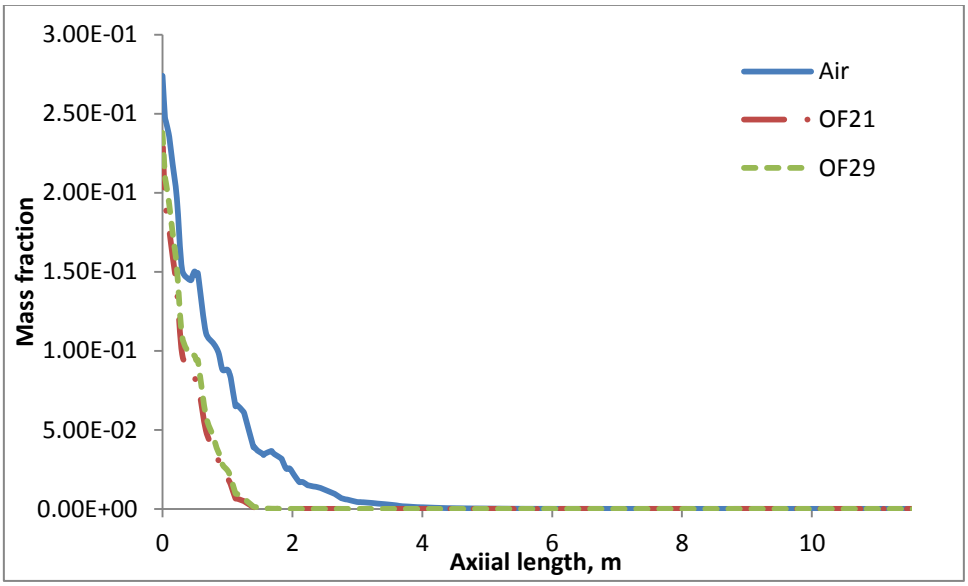

Figure 42. Mass fraction of C_6H_6 along the axis of burner 2 (z=4.662 m)

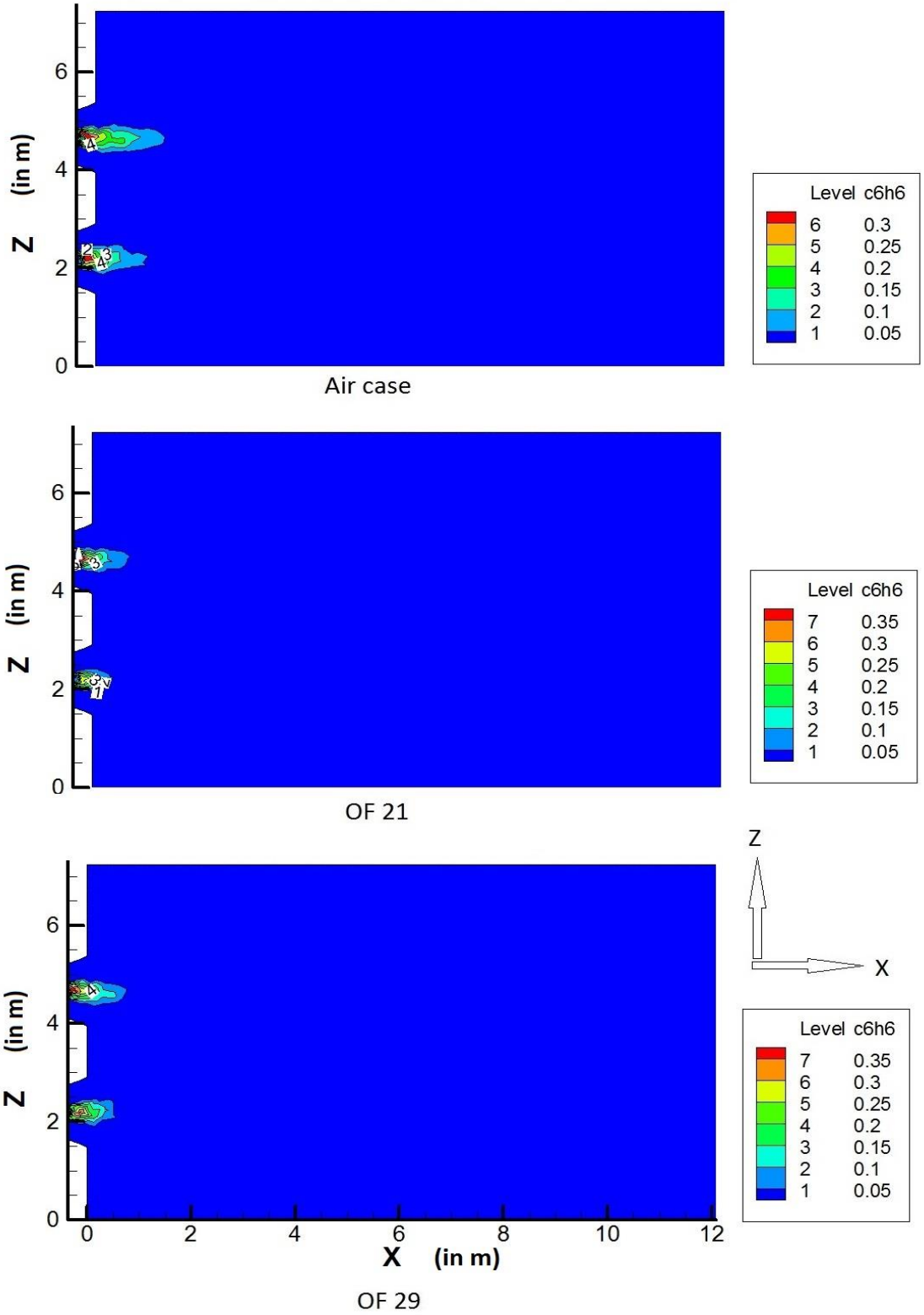

Figure 43. Mass fraction of C_6H_6 for vertical plane at y=-2.24 m

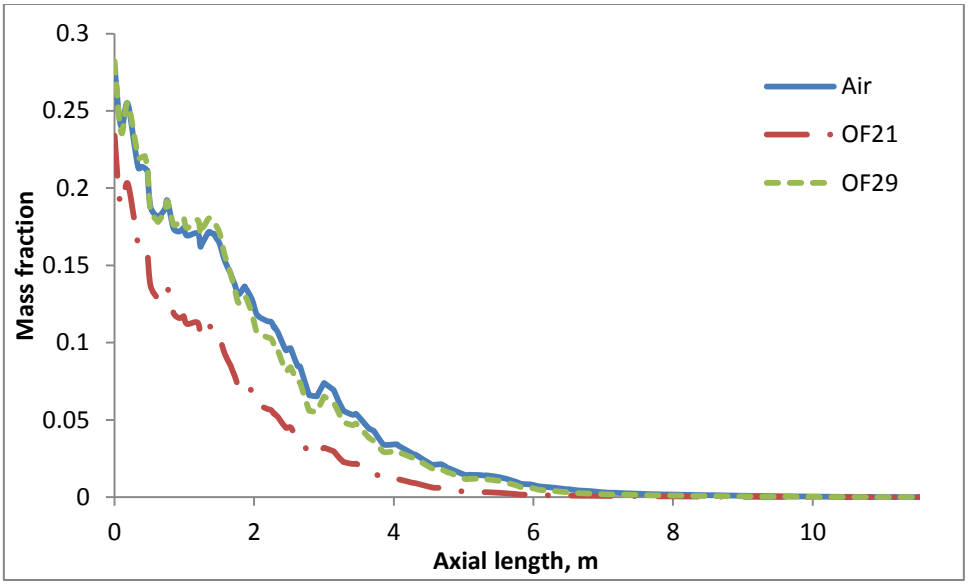

Figure 44. Mass fraction of CH_4 along the axis of burner 1 (z=2.198 m)

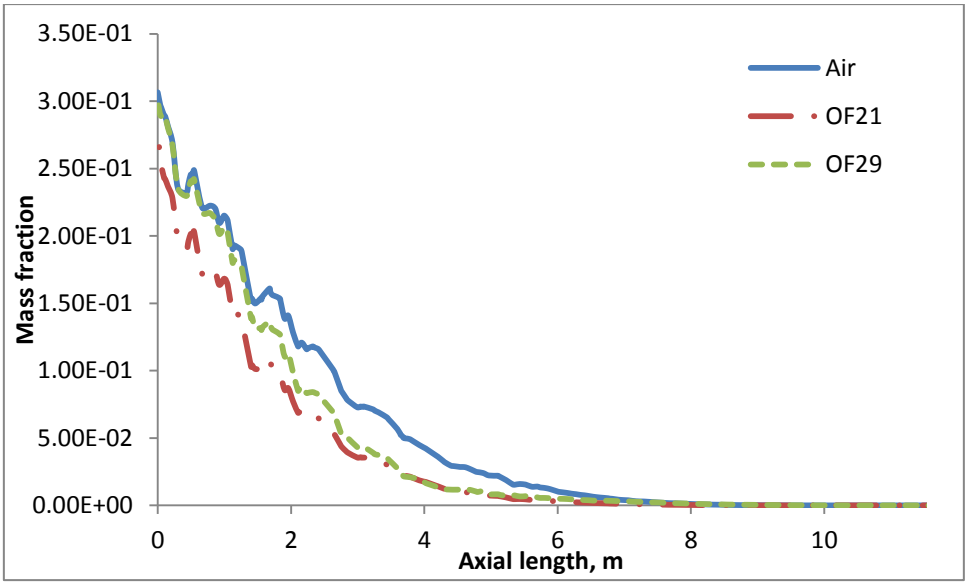

Figure 45. Mass fraction of CH_4 along the axis of burner 2 (z=4.662 m)

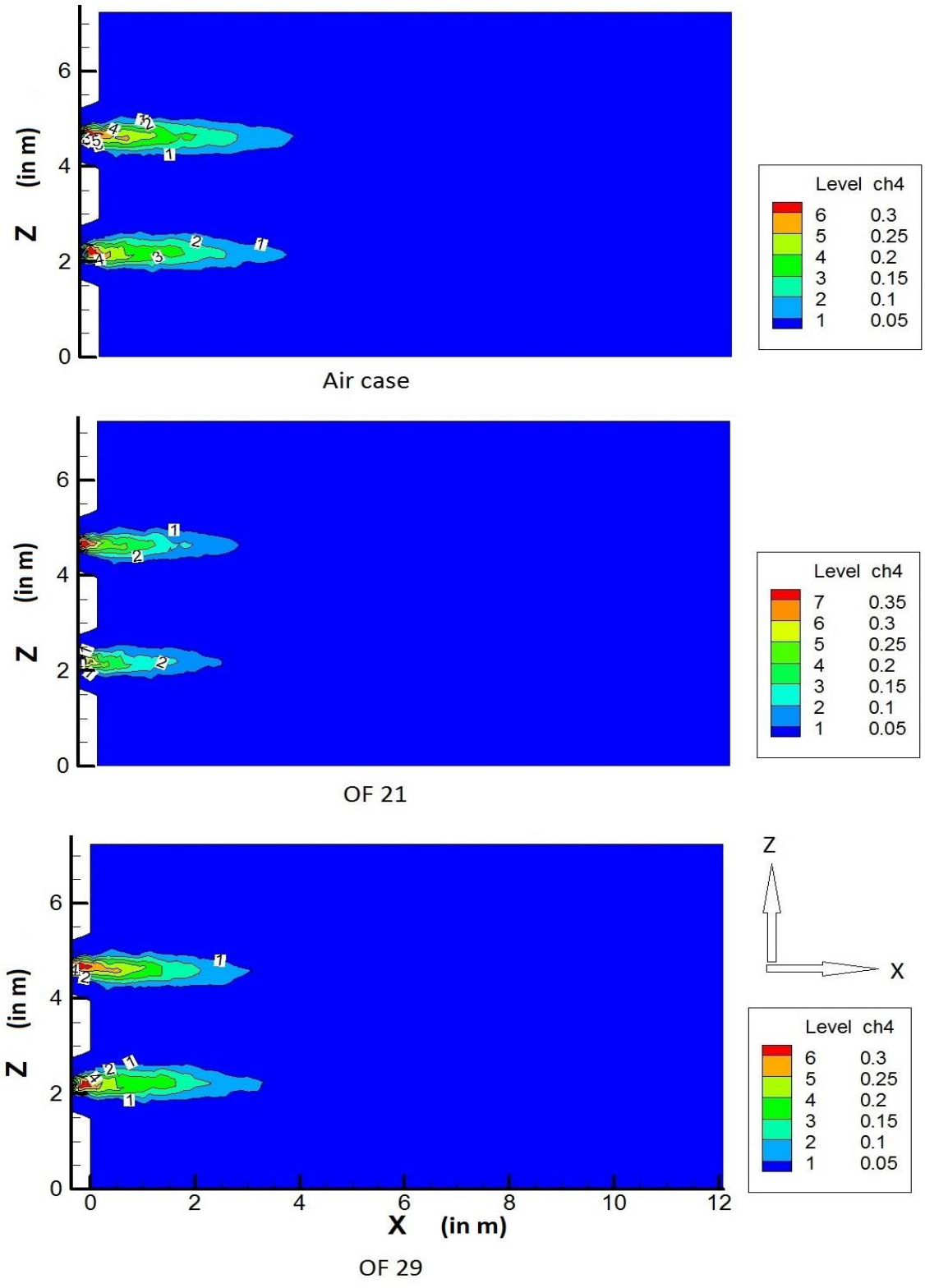

Figure 46. Mass fraction of CH_4 for vertical plane at y=-2.24 m

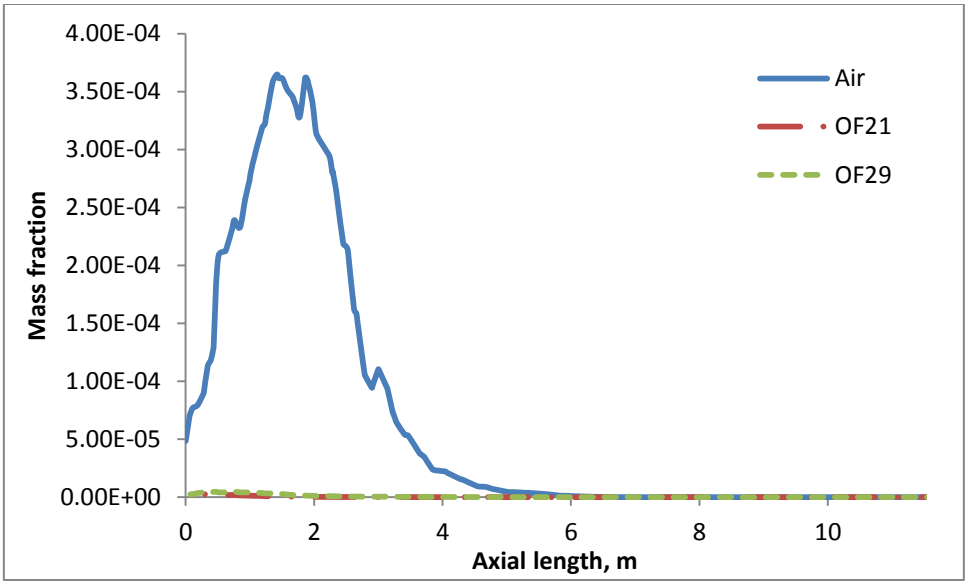

Figure 47. Mass fraction of C_2H_4 along the axis of burner 1 (z=2.198 m)

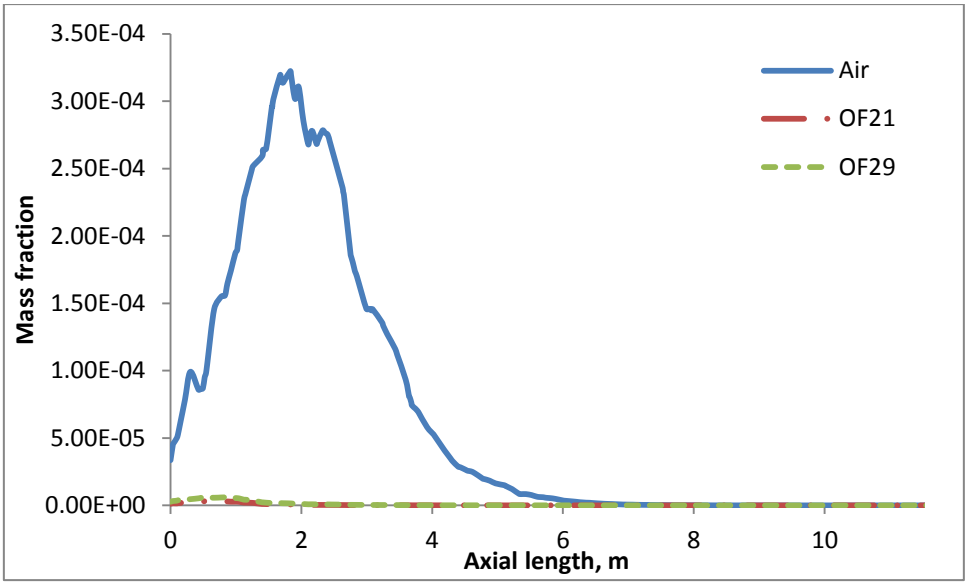

Figure 48. Mass fraction of C_2H_4 along the axis of burner 2 (z=4.662 m)

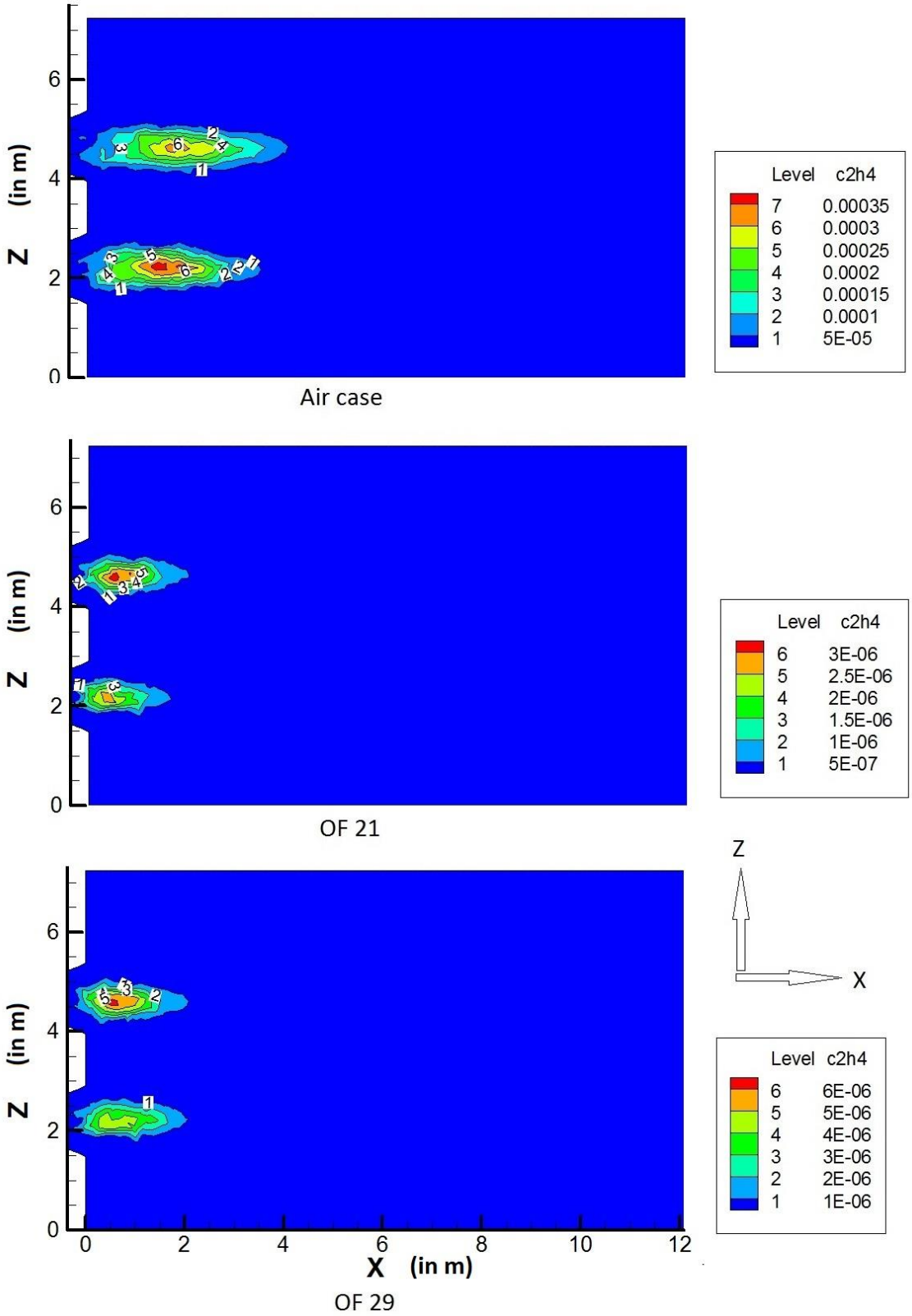

Figure 49. Mass fraction of C_2H_4 for vertical plane at y=-2.24 m

Figure 50 and Figure 51 represent the mass fraction of carbon monoxide along the x-axis for the two burners. It is evident that CO concentration in OF29 case is significantly higher than that of air case. However, production of hydrogen during the reaction is higher in the air case than in the other cases. This can be explained by understanding the mechanism of CO_2 participation during the reactions as has been discussed in the earlier section. As proposed by Liu et al. [49], the CO_2 chemical interaction during combustion is dominated by the following reaction:

$$CO + OH \rightleftharpoons CO_2 + H \quad (41)$$

Thus, an increase in concentration of CO_2 in the environment will shifts the reaction towards the left side which means higher *CO* production. This means higher *CO* and lower *H* radical concentrations in carbon dioxide rich environment. Lower *H* radical reduces the production of hydrogen as is evident from Figure 53 and Figure 54, which show that the mass fractions of hydrogen is highest for the air case while lowest for OF21 case.

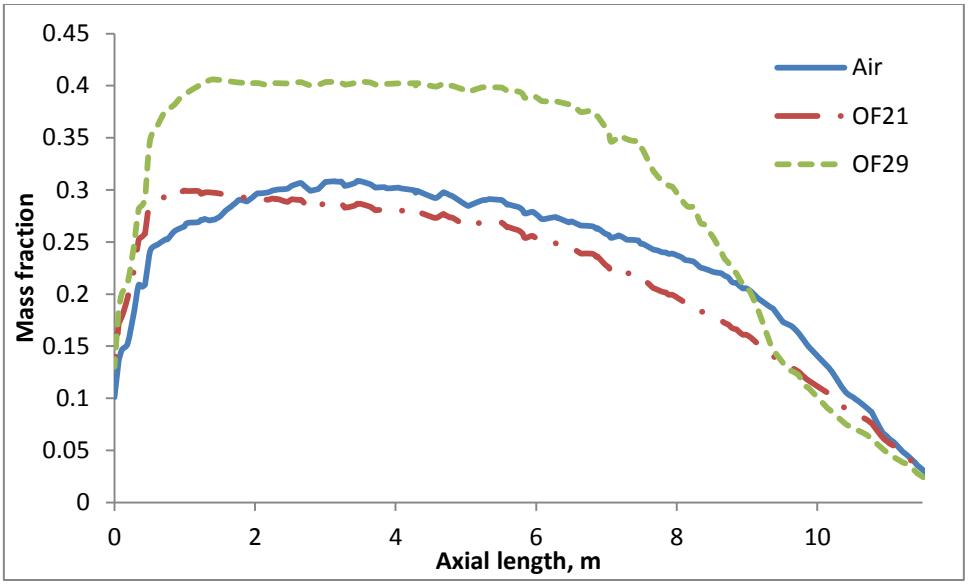

Figure 50. Mass fraction of CO along the axis of burner 1 (z=2.198 m)

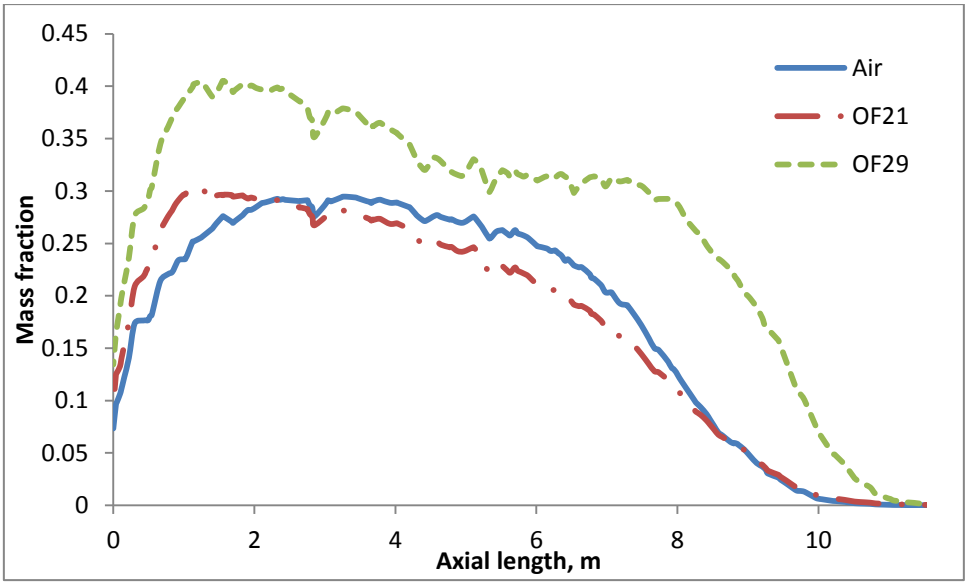

Figure 51. Mass fraction of CO along the axis of burner 2 (z=4.662 m)

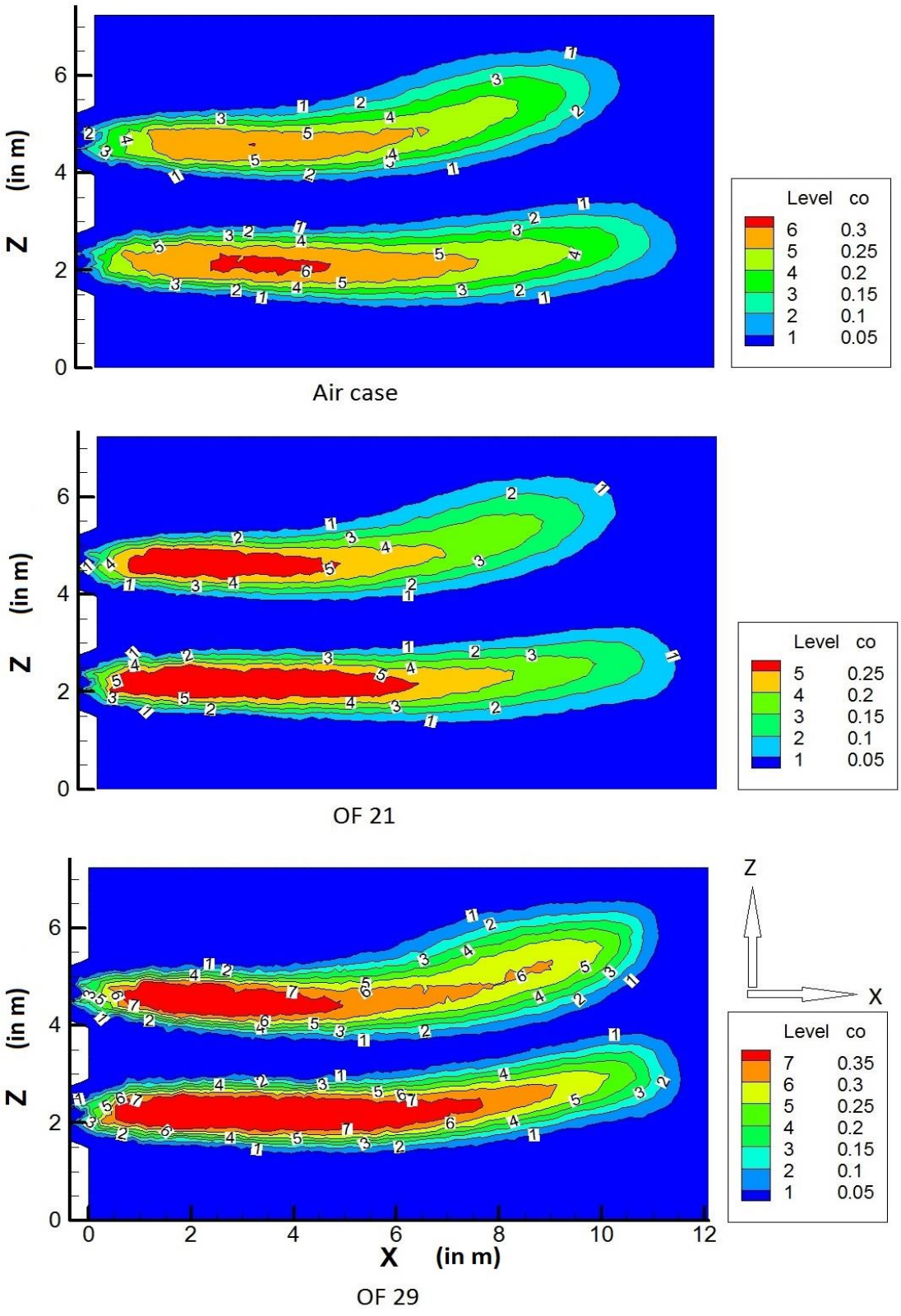

Figure 52. Mass fraction of CO for vertical plane at y=-2.24 m

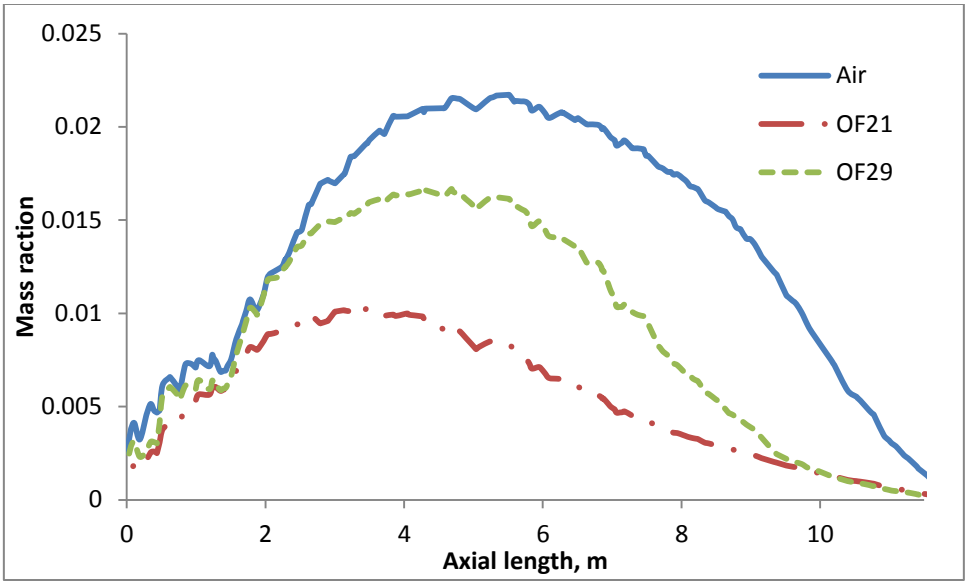

Figure 53. Mass fraction of hydrogen along the axis of burner 1 (z=2.198 m)

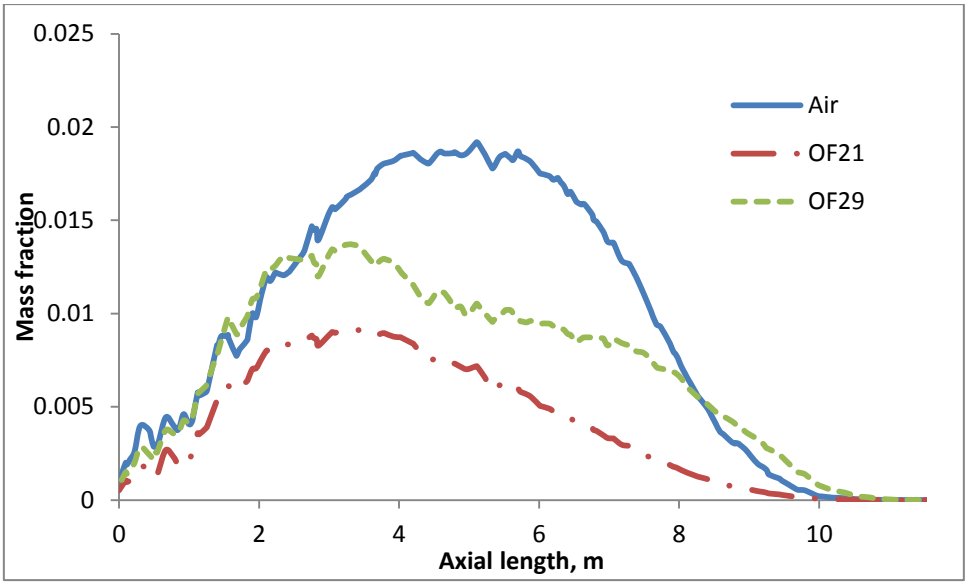

Figure 54. Mass fraction of hydrogen along the axis of burner 2 (z=4.662 m)

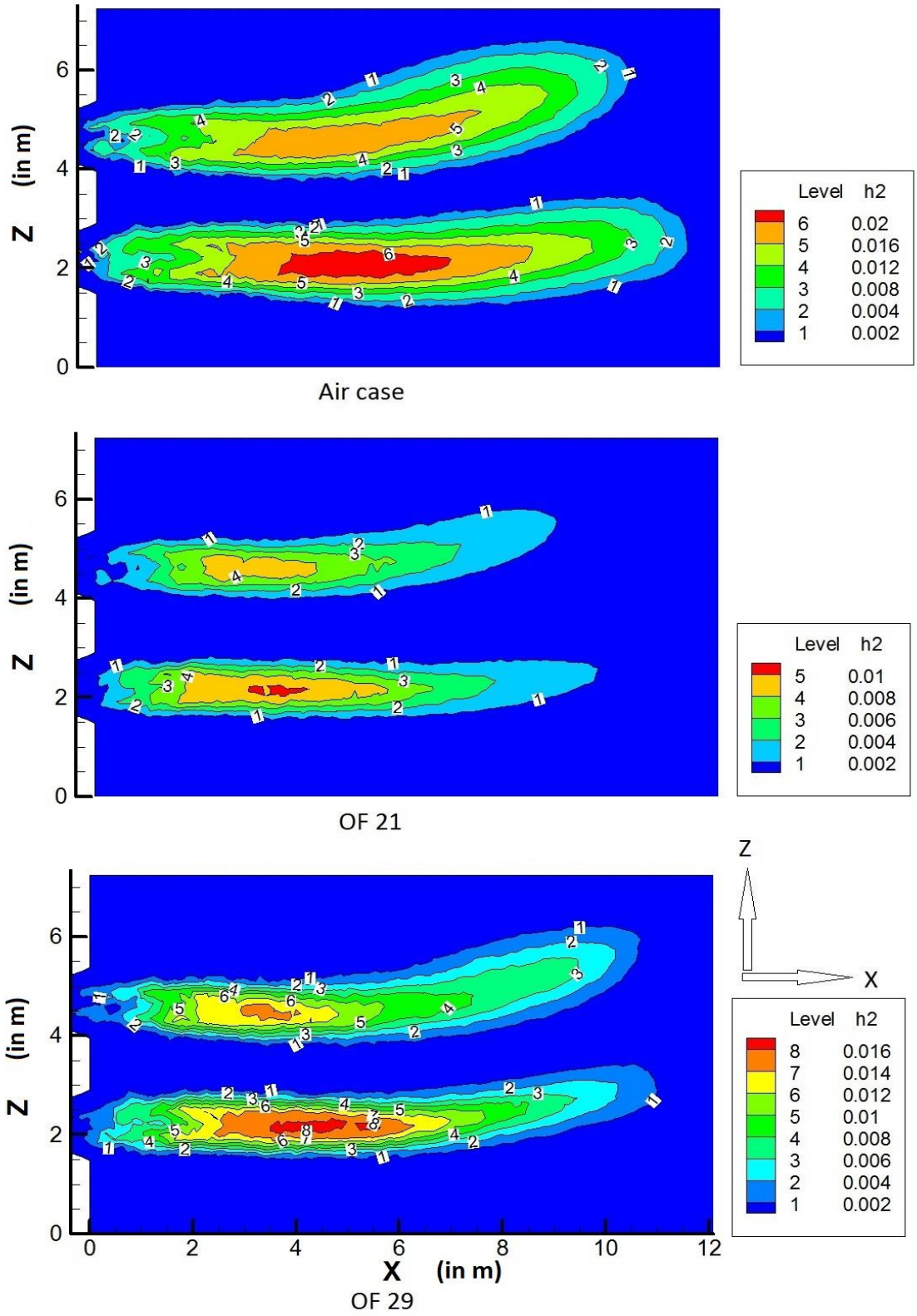

Figure 55. Mass fraction of hydrogen for vertical plane at y=-2.24 m

As discussed above, longer carbon chains break quickly in the carbon dioxide environment into smaller components, which means more reactive hydrogen is available to participate in combustion. Thus, hydrogen quickly reacts with oxygen to form water vapour in CO_2 environment while this is not the case for air combustion as intermediate and smaller carbon compounds are formed during the reaction. Thus, we can see from Figure 56 and Figure 57 that H_2O production is less in the air case in comparison to the oxy-combustion cases. Also, the peak value of H_2O concentration is close to 8 m from the burners which is also the maximum temperature zone as can be seen from Figure 23 and Figure 24. Thus, higher production of H_2O corresponds to higher reaction rate. Moreover, OH concentration for the air case and OF29 case show the same trend but for OF21 case it is quite low. From Figure 59 and Figure 60 we see that along the lower burner, OH concentration is very low and starts appearing from a distance of 7 m onwards from the burner, but for the upper burner it starts appearing from a distance of around 3 m onwards. Also, we can see some fluctuations in the concentration profiles. This is a combined result of buoyancy and turbulence. Thus, OH produced along the lower burner diffuses upwards due to buoyancy and the swirl results in fluctuating concentration profile. Effect of buoyancy is more prominent in OF29 case than the air case, as can be seen from the axial profile for the upper burner that OH concentrations at the distance of around 3 m to 6 m is higher for OF29 case. This has been explained in the previous section that the replacement of N_2 with CO_2 increases the buoyancy effect and upward bending of the flames is more apparent. It can be seen from the figure that the maximum OH concentration levels are achieved earlier along the upper burner (Figure 60) for the air case because of higher reaction rate. This can be confirmed by the axial temperature

profile for the upper burner (Figure 24) which shows that the maximum flame temperature is achieved earlier for the air case. However, for the lower burner (Figure 59) the peak is achieved earlier for OF29 case because of upward bending of the flame. Bending causes the reaction zone to shift towards the axial line, thus, shifting the concentration and temperature peaks upstream along the lower burner for OF29 case.

The mass fractions of oxygen along the x-axis for the upper and lower burners are shown in Figure 62 and Figure 63, respectively, for the three cases. Again, we see that the peak is achieved earlier for OF29 case along the lower burner while along the upper burner the peak is achieved earlier for the air case. As has been discussed earlier, this is because of the faster reaction rate for the air case as is evident from the upper burner profile. However, for the lower burner, upward bending of the flame causes a shift in the peak.

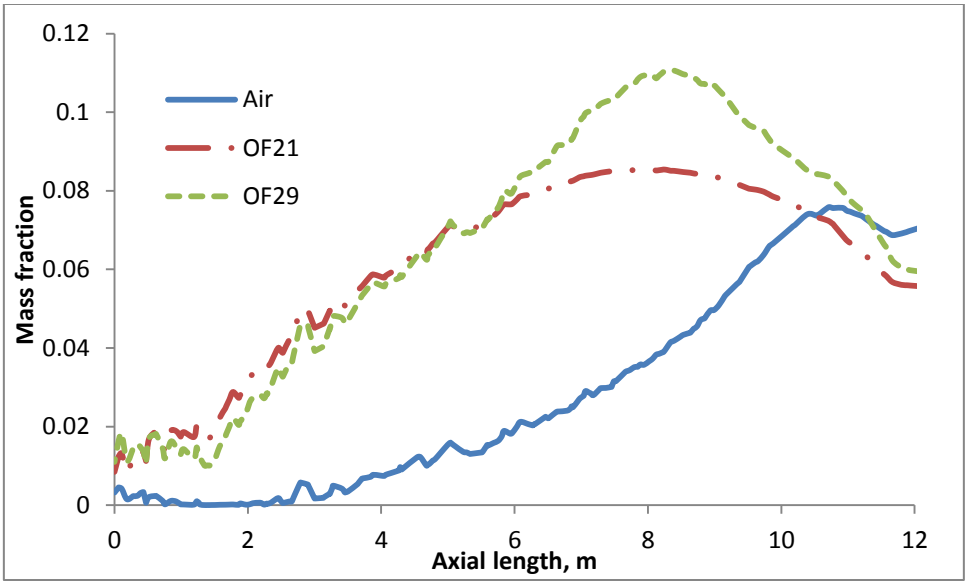

Figure 56. Mass fraction of H_2O along the axis of burner 1 (z=2.198 m)

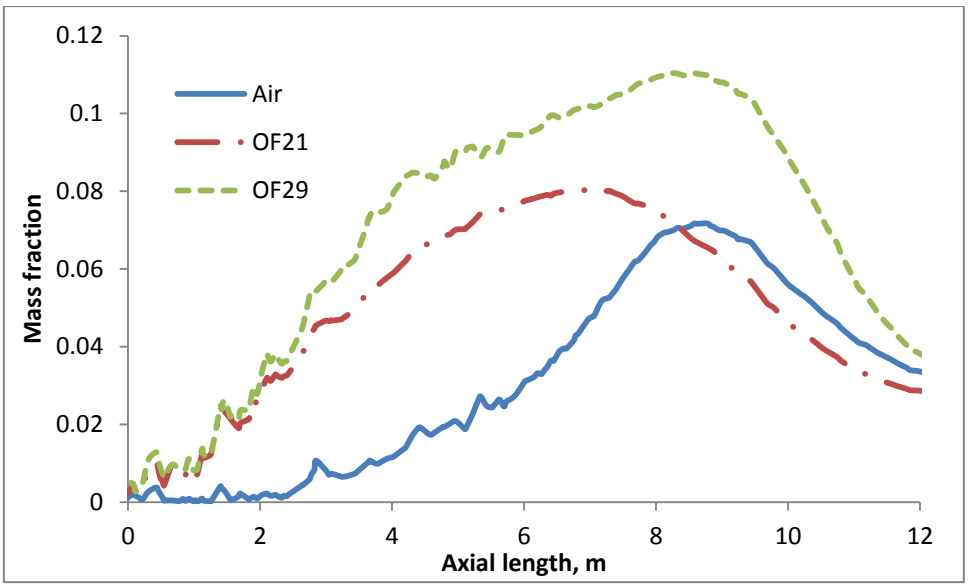

Figure 57. Mass fraction of H_2O along the axis of burner 2 (z=4.662 m)

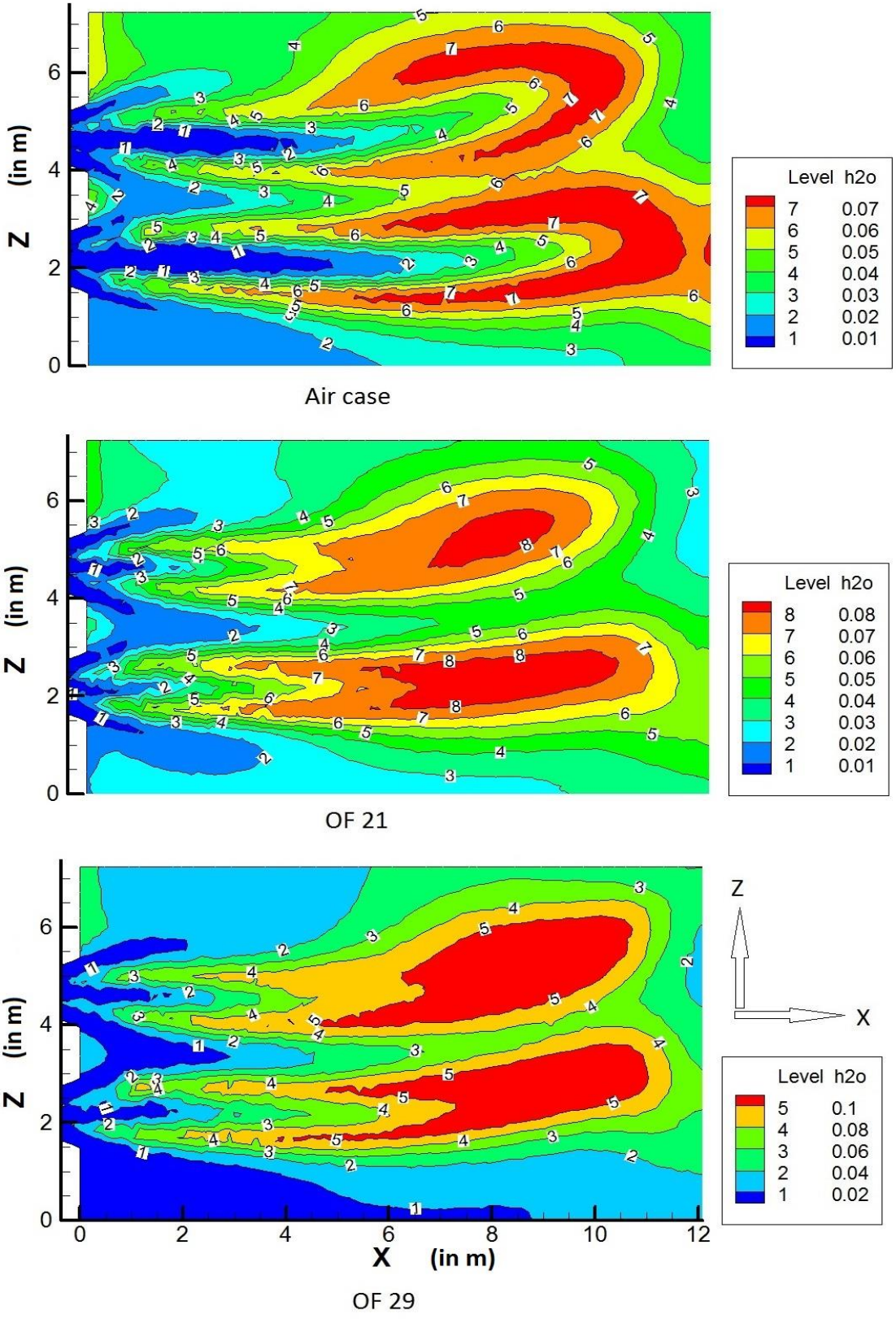

Figure 58. Mass fraction of H_2O for vertical plane at y=-2.24 m

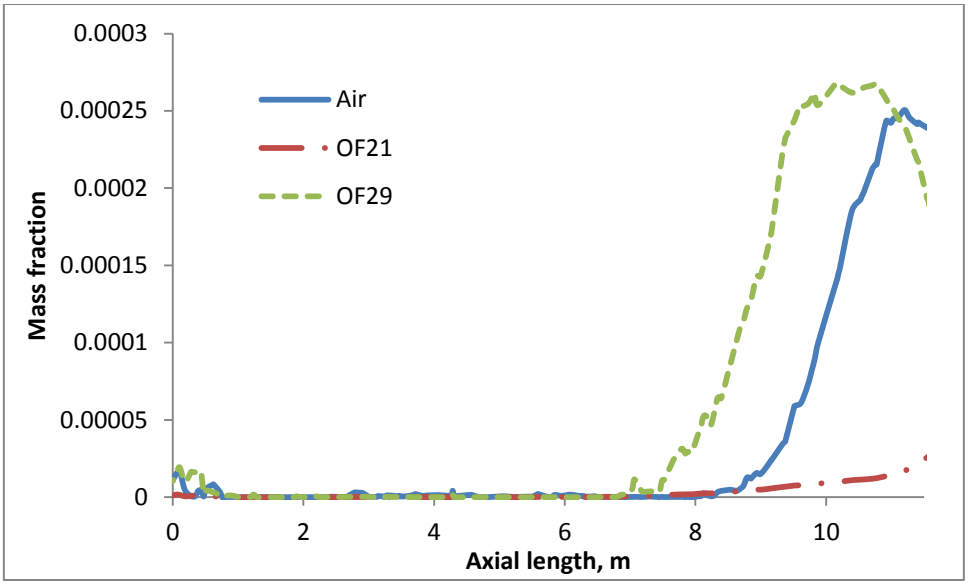

Figure 59. Mass fraction of OH along the axis of burner 1 (z=2.198 m)

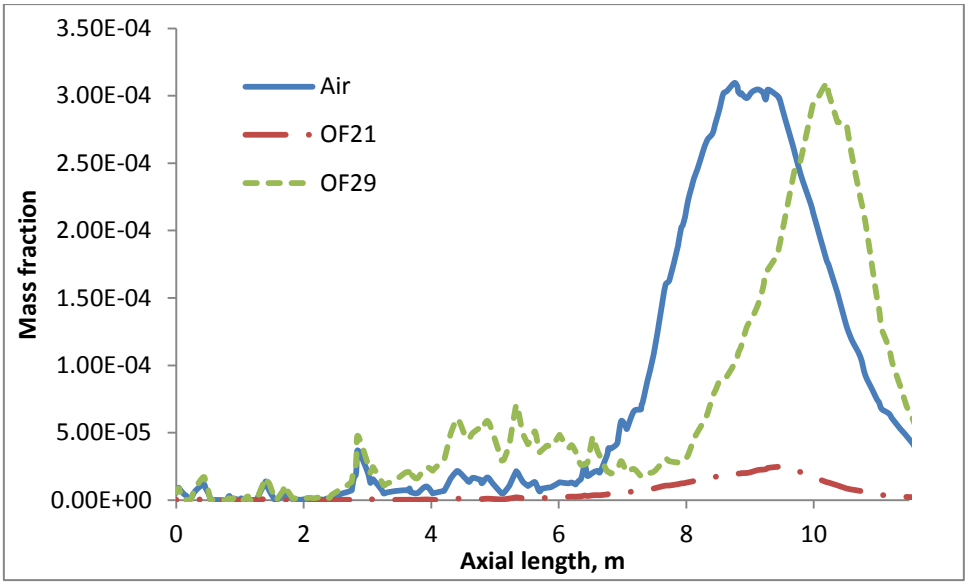

Figure 60. Mass fraction of OH along the axis of burner 2 (z=4.662 m)

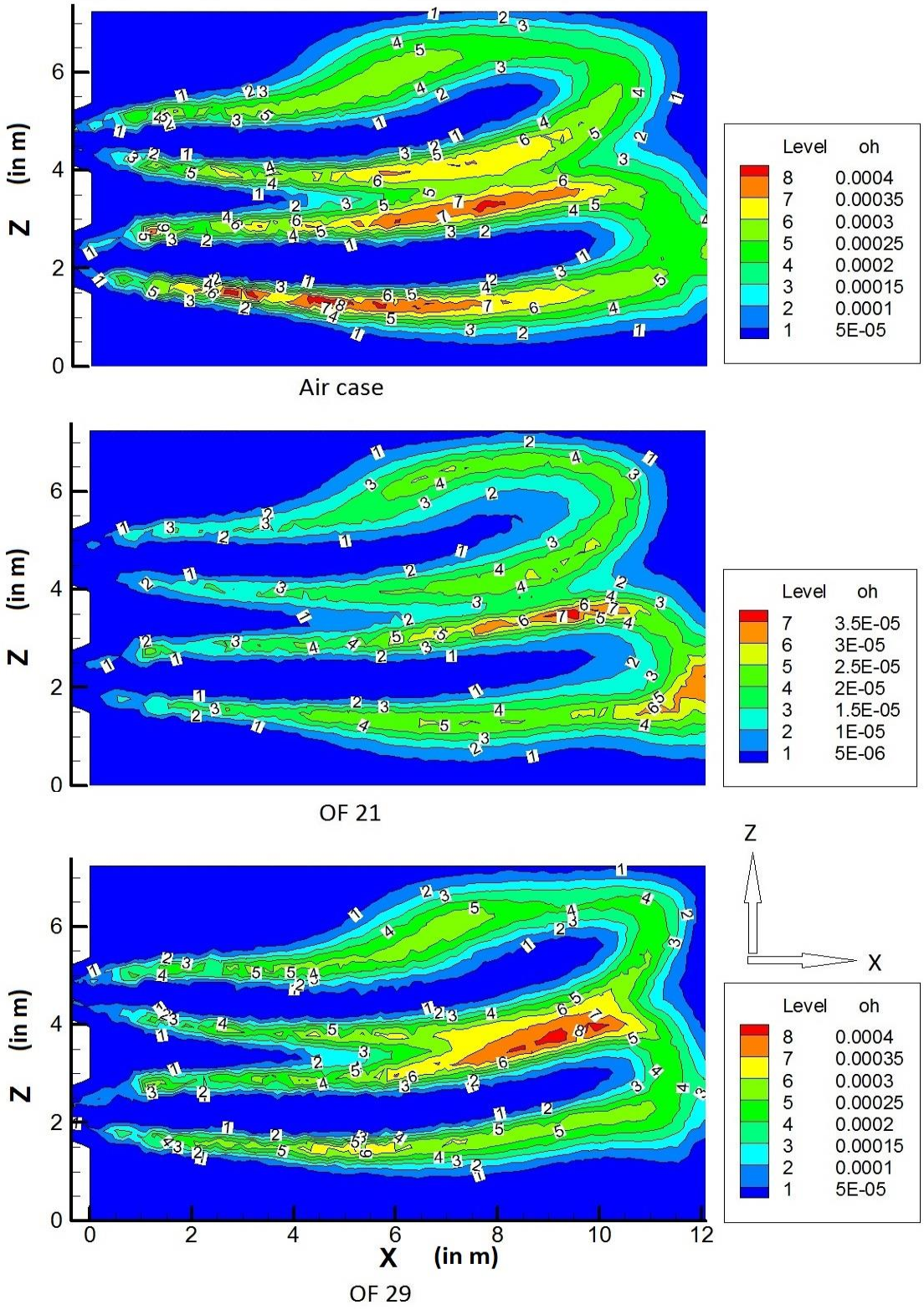

Figure 61. Mass fraction of OH for vertical plane at y=-2.24 m

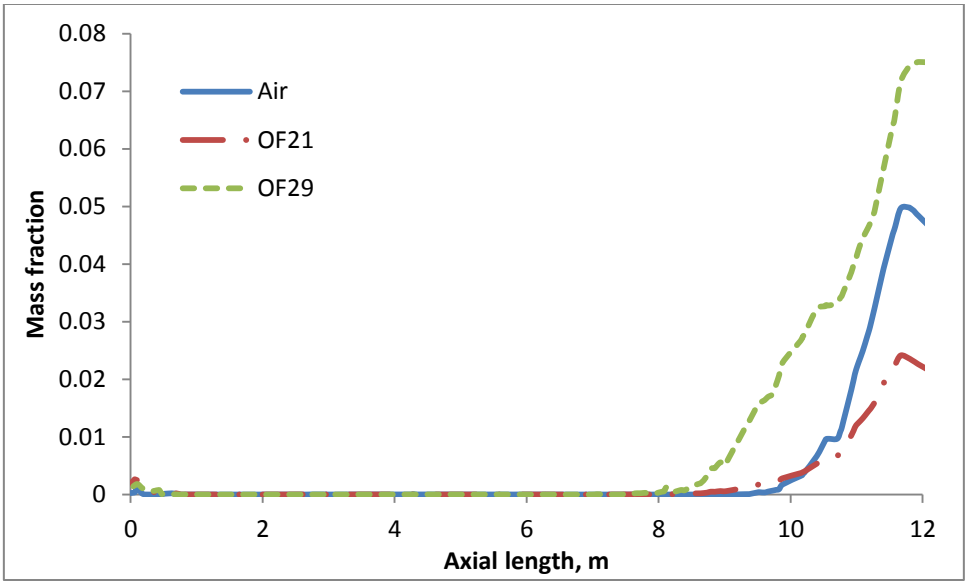

Figure 62. Mass fraction of oxygen along the axis of burner 1 (z=2.198 m)

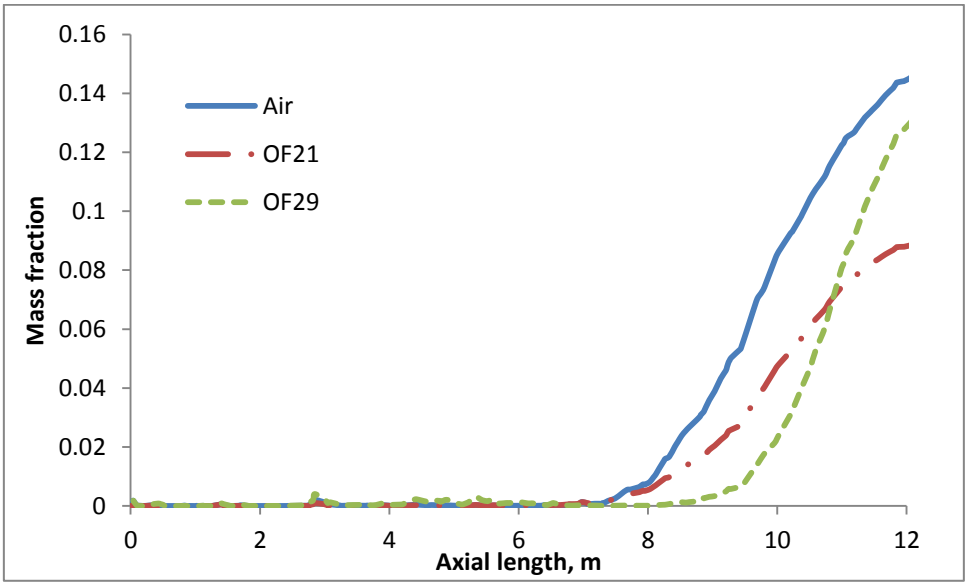

Figure 63. Mass fraction of oxygen along the axis of burner 2 (z=4.662 m)

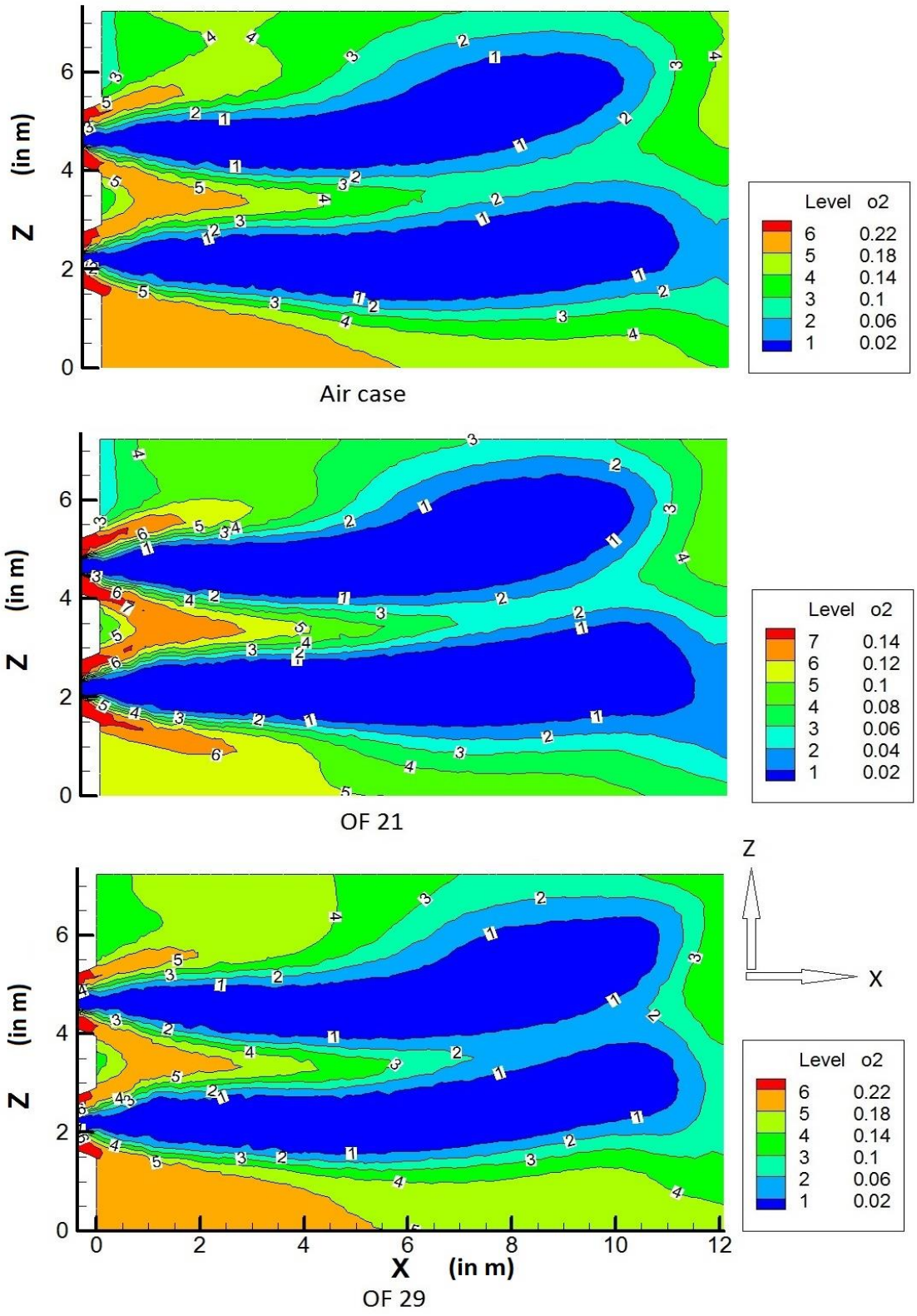

Figure 64. Mass fraction of oxygen for vertical plane at y=-2.24 m

As we have seen that carbon dioxide plays an important role in the combustion chemistry and affects the reaction chains and intermediate compounds. Similarly, formation of soot is also greatly affected by the percentage of carbon dioxide present in the combustion environment. Figure 65 and Figure 66 show the axial profile of logarithmic (base 10) mole fraction of soot along the lower and upper burners, respectively and Figure 67 represents the molar concentration of soot for the vertical plane containing the two burners. We can see that the soot formation is greatly reduced by increasing the CO_2 percentage in the reactor. Thus, soot concentration is highest for the air case while it reduces significantly for OF29 case because of the replacement of nitrogen with the carbon dioxide. Soot formation is further reduced for OF21 case because of increased carbon dioxide percentage in the combustion chamber. This trend has also been found by Andersson et al. [50] in their investigation on radiation intensity of propane fired oxy-combustion flames.

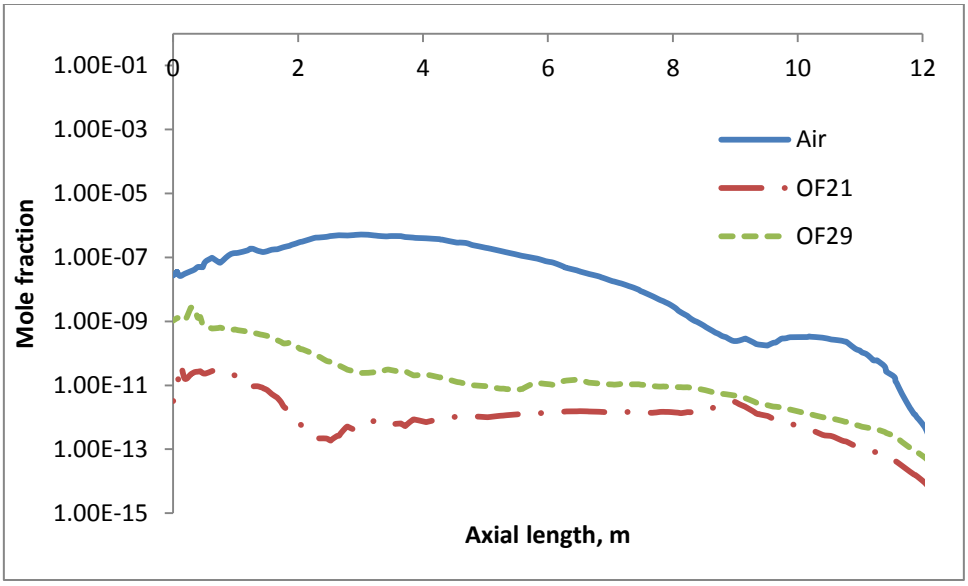

Figure 65. Mole fraction of soot along the axis of burner 1 (z=2.198 m)

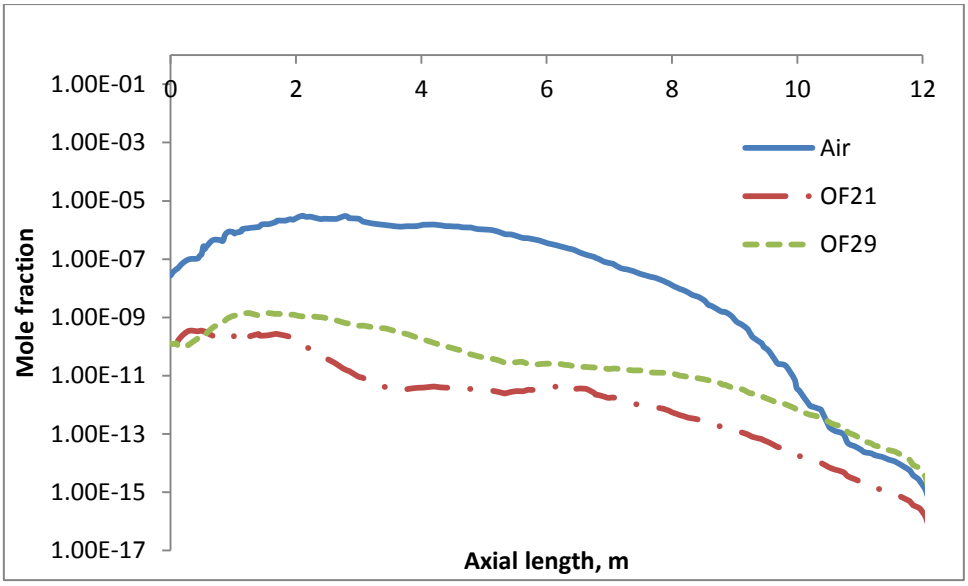

Figure 66. Mole fraction of soot along the axis of burner 2 (z=4.662 m)

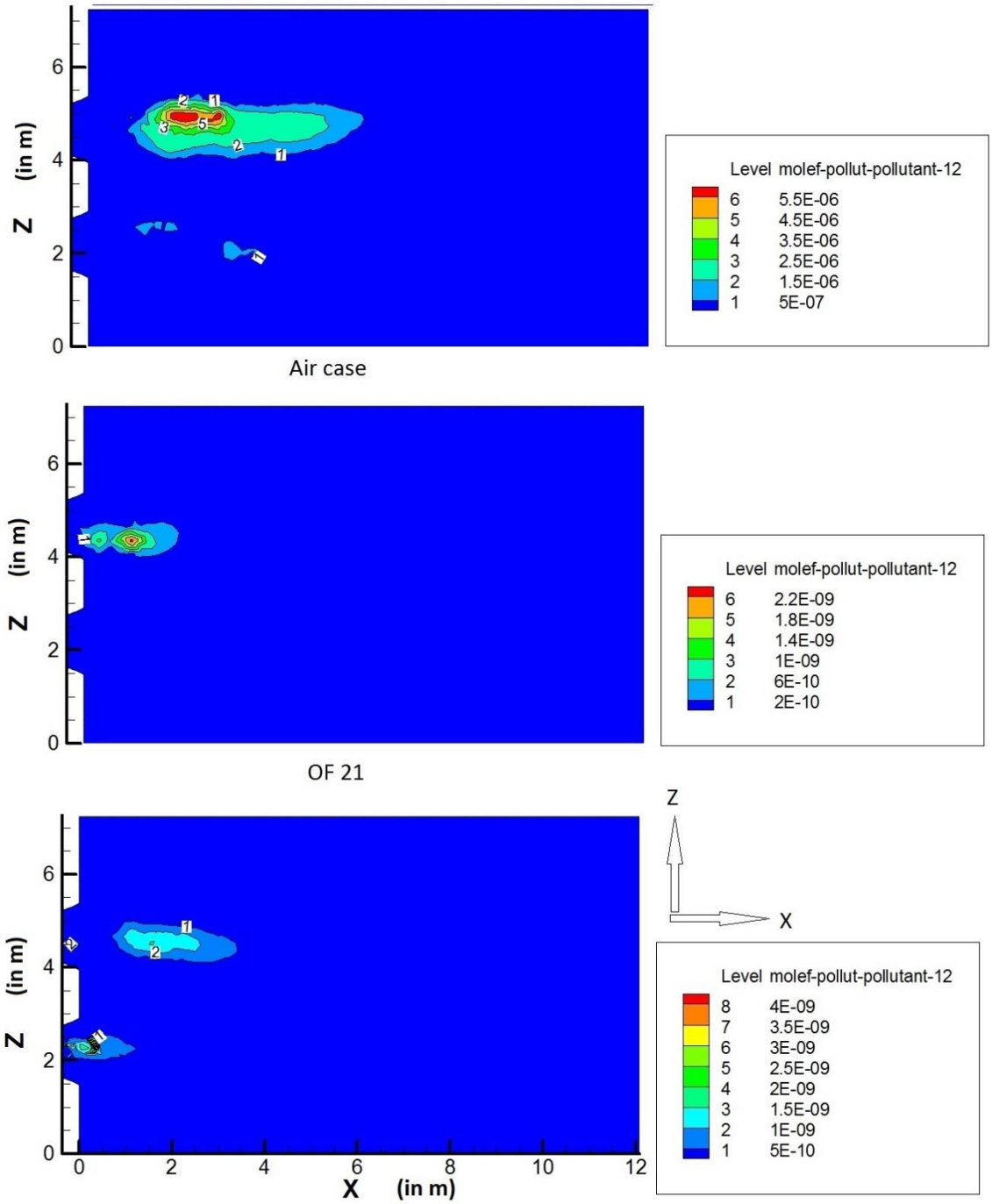

Figure 67. Mole fraction of soot for vertical plane at y=-2.24 m

Figure 68 and Figure 69 show total heat transfer rate and radiative heat transfer rate along the furnace top, respectively. Top of the furnace is divided into four sections such that part 1 represents the first section near the burner and part 4 represents the end section of the furnace. Similarly, side wall on the left and side wall on the right (near tube bank) are divided into four sections and numbered just as the top wall. Figure 70 to Figure 71 show total heat transfer rate and radiative heat transfer rate along the left side wall and right side wall, respectively. We can see that total heat transfer is the highest for the air case while the lowest for OF21. In the furnace part, radiative heat transfer is very significant and constitutes around 80-90% of the total heat transfer. This is because of very high flame temperature in this region. However, for the tube bank part radiative heat transfer constitutes around 30-40% of the total heat transfer which means convection is significant in this region.

Figure 74 and Figure 75 total heat transfer and radiative heat transfer along the boiler tube bank, respectively. Bank 1 corresponds to the water jackets nearest to the furnace and the bank number increases along the downstream. We can see that both total heat flux and radiation heat transfer is highest for the air case and lowest for the OF21 case. This is obvious because of much lower temperature level for OF21 case in comparison to the air case. Due to high mass fraction of CO_2 present in OF21 case most of the heat evolved is absorbed by carbon dioxide, remember high thermal capacity of CO_2 compared to N_2. Reducing the percentage of carbon dioxide in the oxidizer stream increases the heat transfer rate as we can see in OF29 case, however, the value is still than that of air case. This is because of lower temperature level and non-uniform distribution of temperature in OF29 case. Further, due to higher molecular mass of CO_2 compared to

N_2, volume flow rate in OF29 case is too low. This reduces the convective heat transfer efficiency inside the boiler. Apart from that, we see that presence of CO_2 has drastic influence on the formation of soot. Figure 67 shows that soot formation in OF21 and OF29 cases are negligible. Presence of significant amount of soot in the air case increases the radiation intensity of the flame and thus, the radiation heat transfer as has also been found experimentally [50].

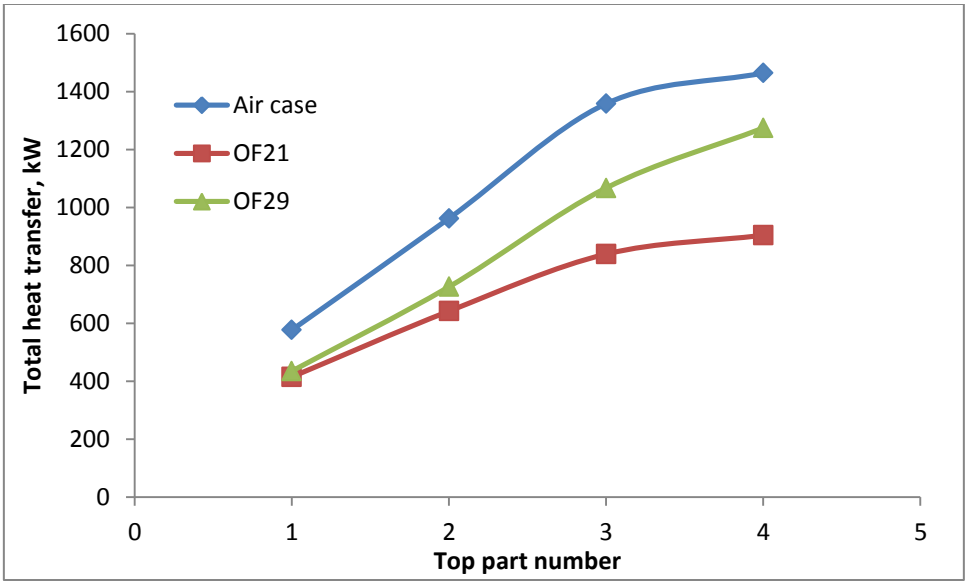

Figure 68. Distribution of total heat transfer rate (kW) along the furnace top

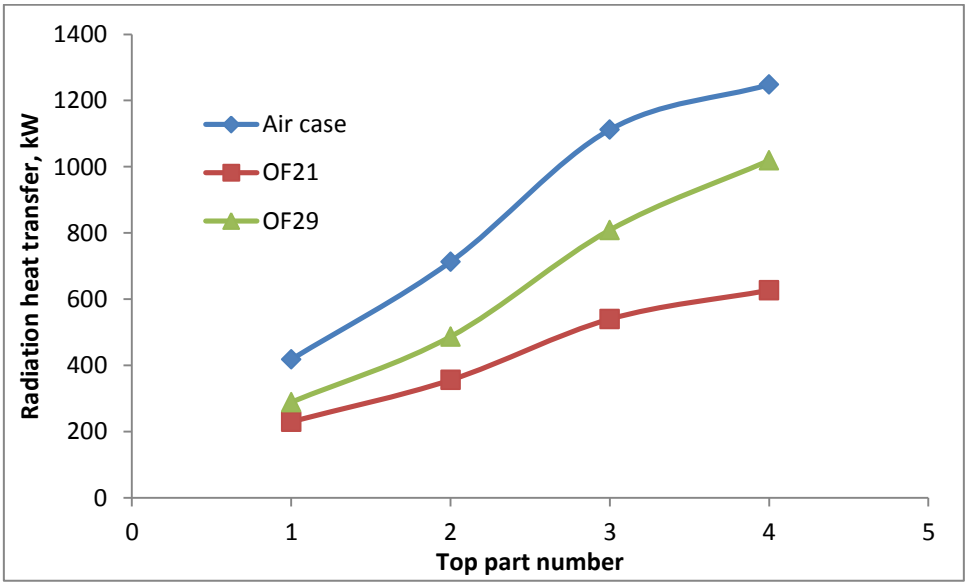

Figure 69. Distribution of radiation heat transfer rate (kW) along the furnace top

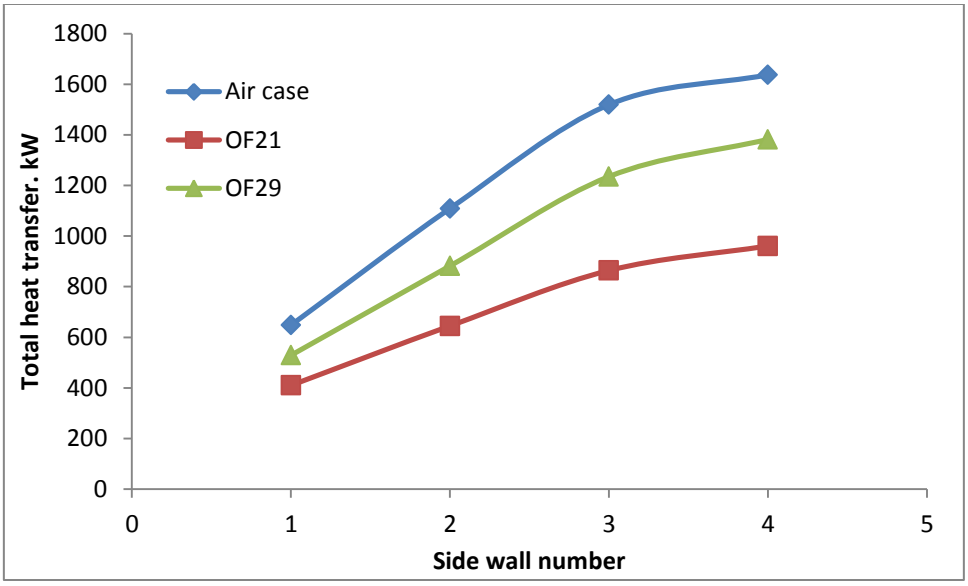

Figure 70. Distribution of total heat transfer rate (kW) along the side wall (left)

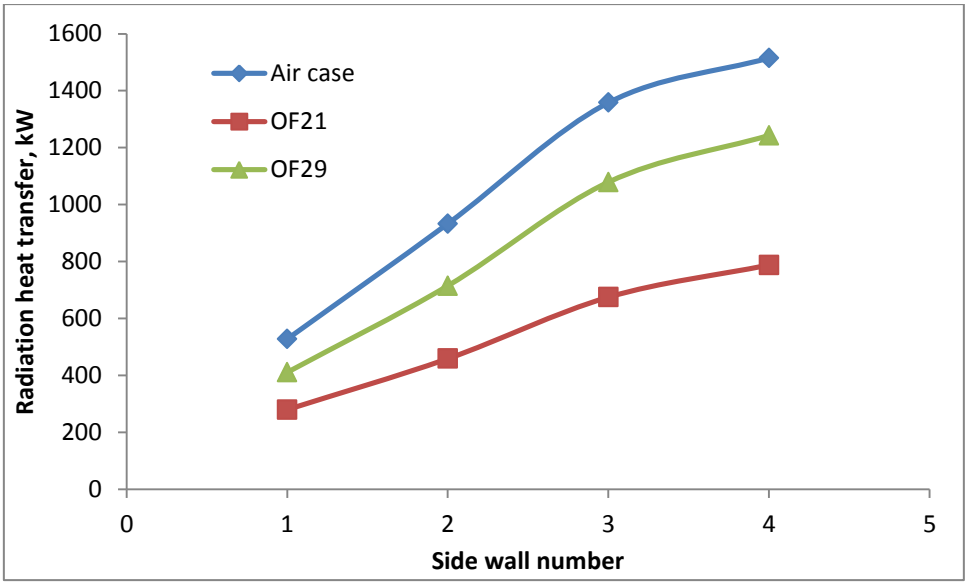

Figure 71. Distribution of radiation heat transfer rate (kW) along the side wall (right)

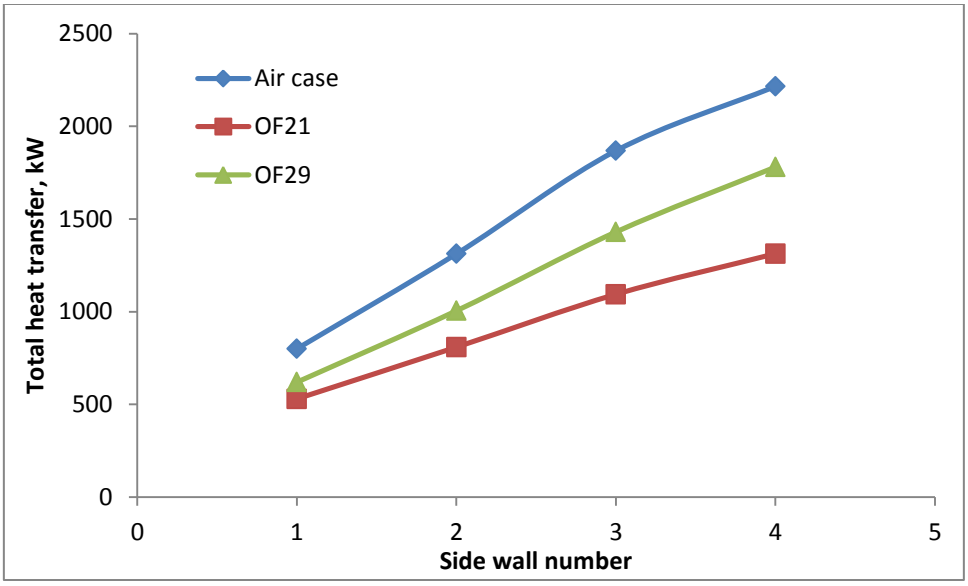

Figure 72. Distribution of total heat transfer rate (kW) along the side wall (left)

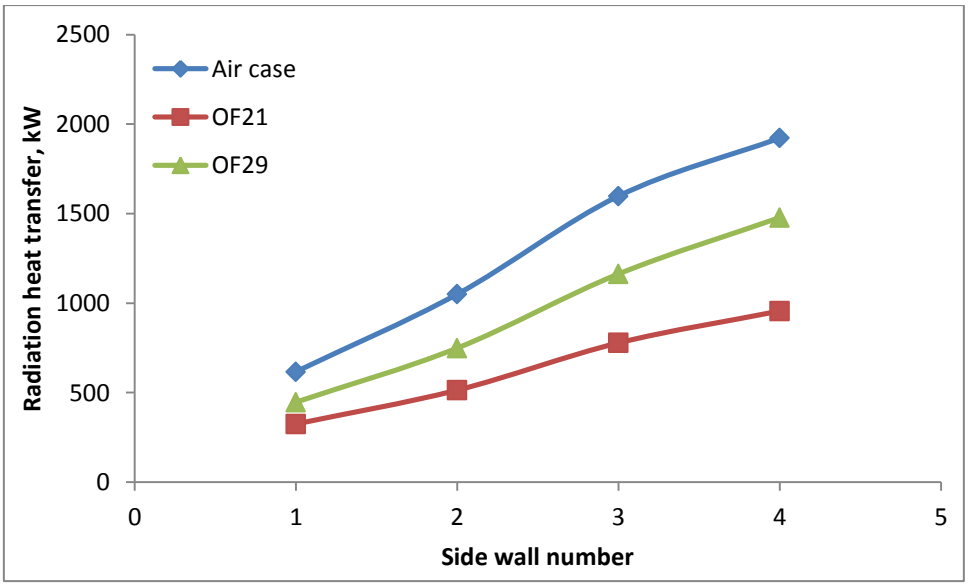

Figure 73. Distribution of radiation heat transfer rate (kW) along the side wall (right)

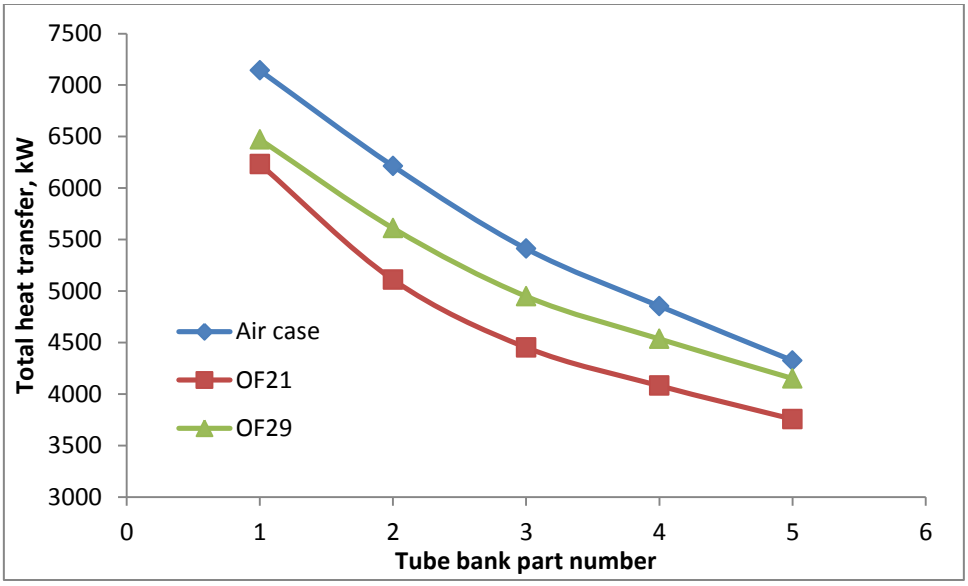

Figure 74. Distribution of total heat transfer rate (kW) along the boiler tube bank

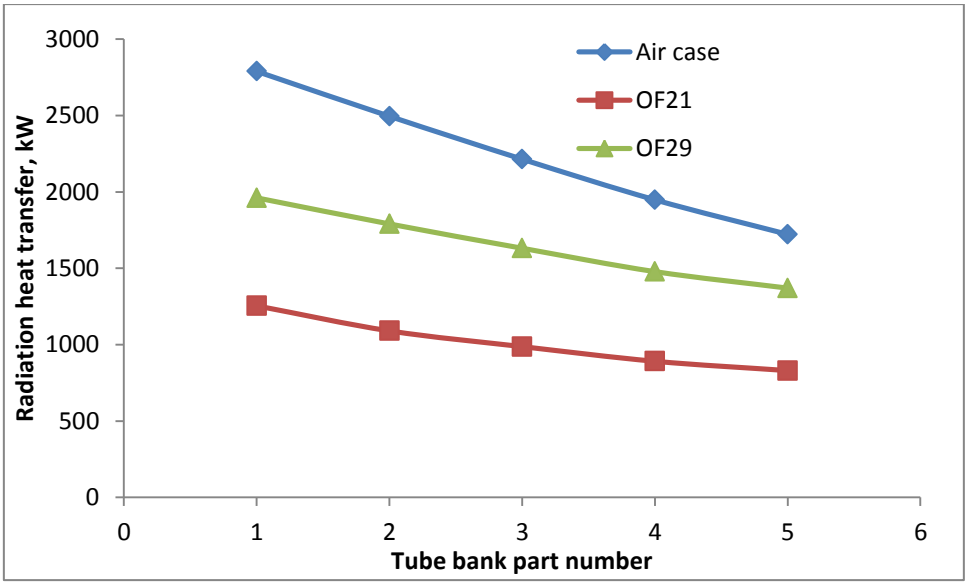

Figure 75. Distribution of radiation heat transfer rate (kW) along the boiler tube bank

4.2.2 Effect of Droplet Size on the Combustion Characteristics

Droplet size is one of the most important factors in the evaporation and combustion of liquid fuels as has been discussed in the earlier section. Evaporation of droplet is drastically influenced by the size of droplets and hence it is a very important parameter in the liquid fuel combustion. In this section, OF29 case has been simulated for three different sizes of the liquid fuel droplets. The three cases have been taken with droplet size of 10 microns, 7 microns and 4 microns. Figure 76 shows the temperature contours for the three cases for the vertical plane passing through both the burners. We can see that reducing the droplet size from 10 microns to 7 microns has very little effect on the combustion pattern and the flame shifts only slightly towards the burner. However, further reduction of droplet diameter to 4 microns has apparently no influence on the combustion. Figure 77 and Figure 78 show the temperature profile along the x-axis for the three cases at burner 1 (the lower burner) and burner 2 (the upper burner) respectively. It can be seen that droplet size does not have any effect on the maximum temperature of the flame. The liquid fuel is introduced into the furnace at the temperature of 300 K and the vaporization temperature of the mixture is around 330 K. Thus, the fuel does not require substantial heat and time to evaporate and participate in the combustion. This means that the evaporation of the droplets is not the limiting factor in the reaction and thus reducing the droplet diameter does not influence the reaction rate. Thus, for this case a droplet size of 10 microns is well and good for the combustion and there is no need to further reduce the diameter.

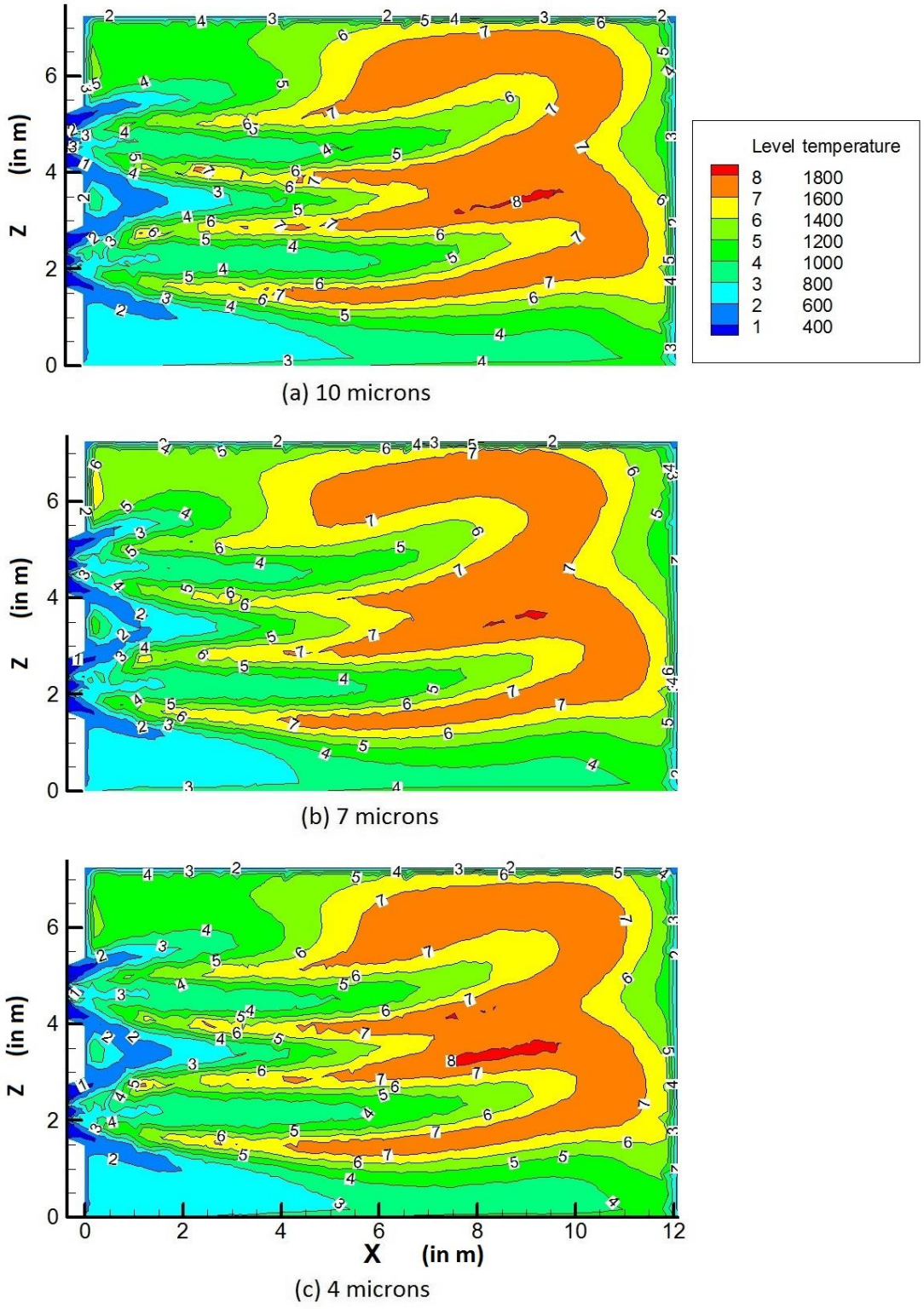

Figure 76. Temperature (K) contours for the vertical pane at y=-2.24 m

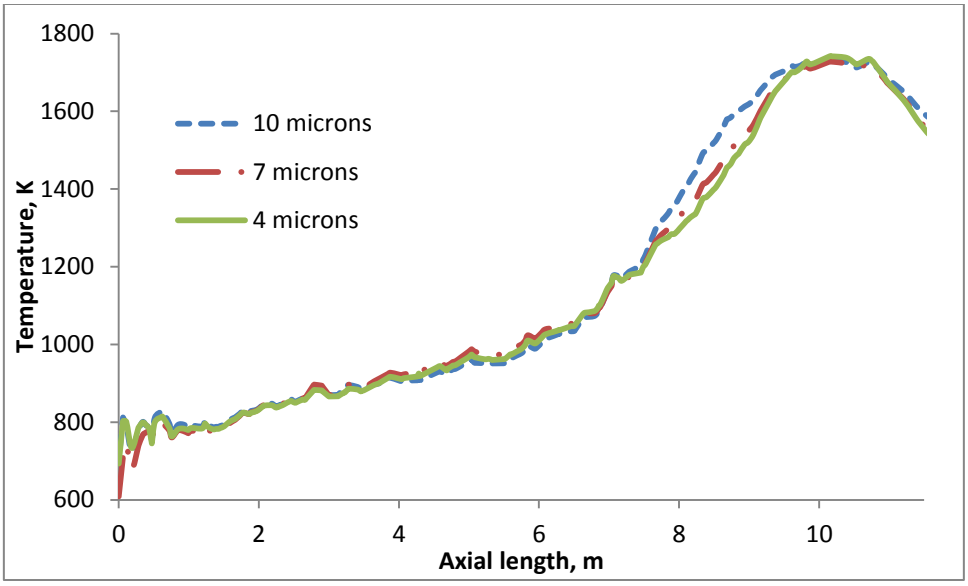

Figure 77. Temperature distribution along the axis of burner 1 (z=2.198 m)

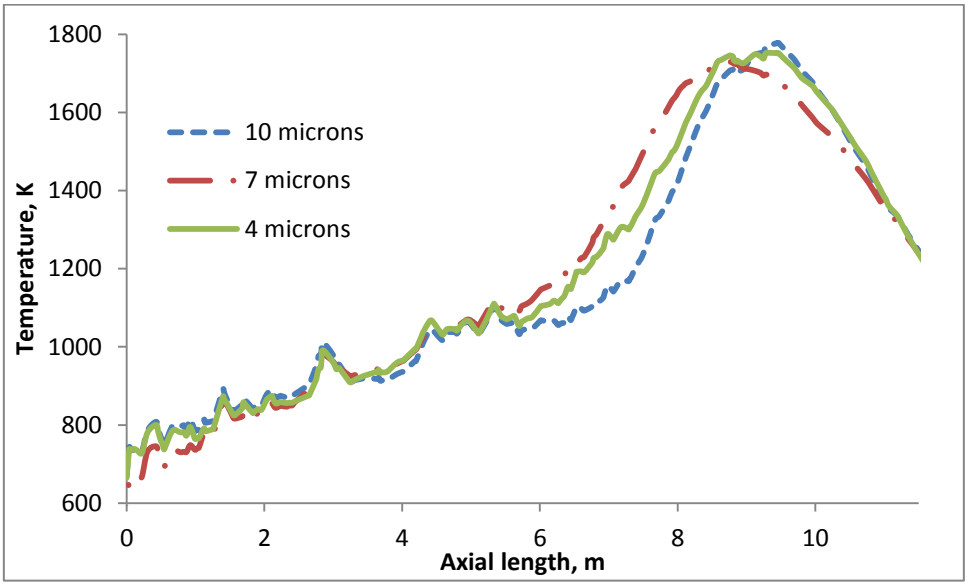

Figure 78. Temperature distribution along the axis of burner 2 (z=4.662 m)

4.2.3 Effect of Swirl Number on the Combustion Characteristics

Swirl number can be defined as the ratio of the axial flux of angular momentum to the axial flux of axial momentum. Swirl enhances the mixing of oxidizer and the fuel and thus increases the combustion rate in case chemical reaction is not the limiting factor. OF29 case was extended to study the effect of swirl number on the combustion characteristics of the liquid fuel for four different cases. Tangential velocity was gradually increased from 27.36 m/s to 41.03 m/s, 53.35 m/s, 65.66 m/s to obtain a swirl number of 0.67, 1.0, 1.3 and 1.6 respectively. Figure 79 shows the temperature contours for the vertical plane passing through both the burners for the four cases. It is evident that increasing swirl number significantly increases the combustion rate and the flame shifts towards the burners. This is because of better mixing of fuel and oxidizer inside the furnace with the increasing swirl. Also, we can see that the temperature distribution is more uniform for high swirl case because of high turbulence and better convection heat transfer. Figure 80 and Figure 81 show the temperature profiles for the four cases along the x-axis from the two burners. We can see that with increasing swirl in the reactor, not only the temperature distribution expands but the maximum temperature level also increases. Temperature contours for horizontal plane along the upper burner are presented in Figure 82. We can see that the increasing swirl number increases the temperature level and decreases the flame length.

Figure 83 shows the turbulent viscosity contours for the four cases and as expected, with the increasing swirl in the reactor the turbulent viscosity of the gases decreases. Thus, it can be concluded swirl has very significant effect on the combustion characteristics for

this case as the rate limiting step in this reaction is turbulence and not the chemical reactivity. Figure 84 and Figure 85 represents the total heat transfer and radiation heat transfer, respectively, for the tube bank section for different swirl numbers. Total heat transfer along the tubes increases with the increasing swirl number. Increasing swirl number from 0.67 to 1.6 increases the total heat transfer by around 4 %.

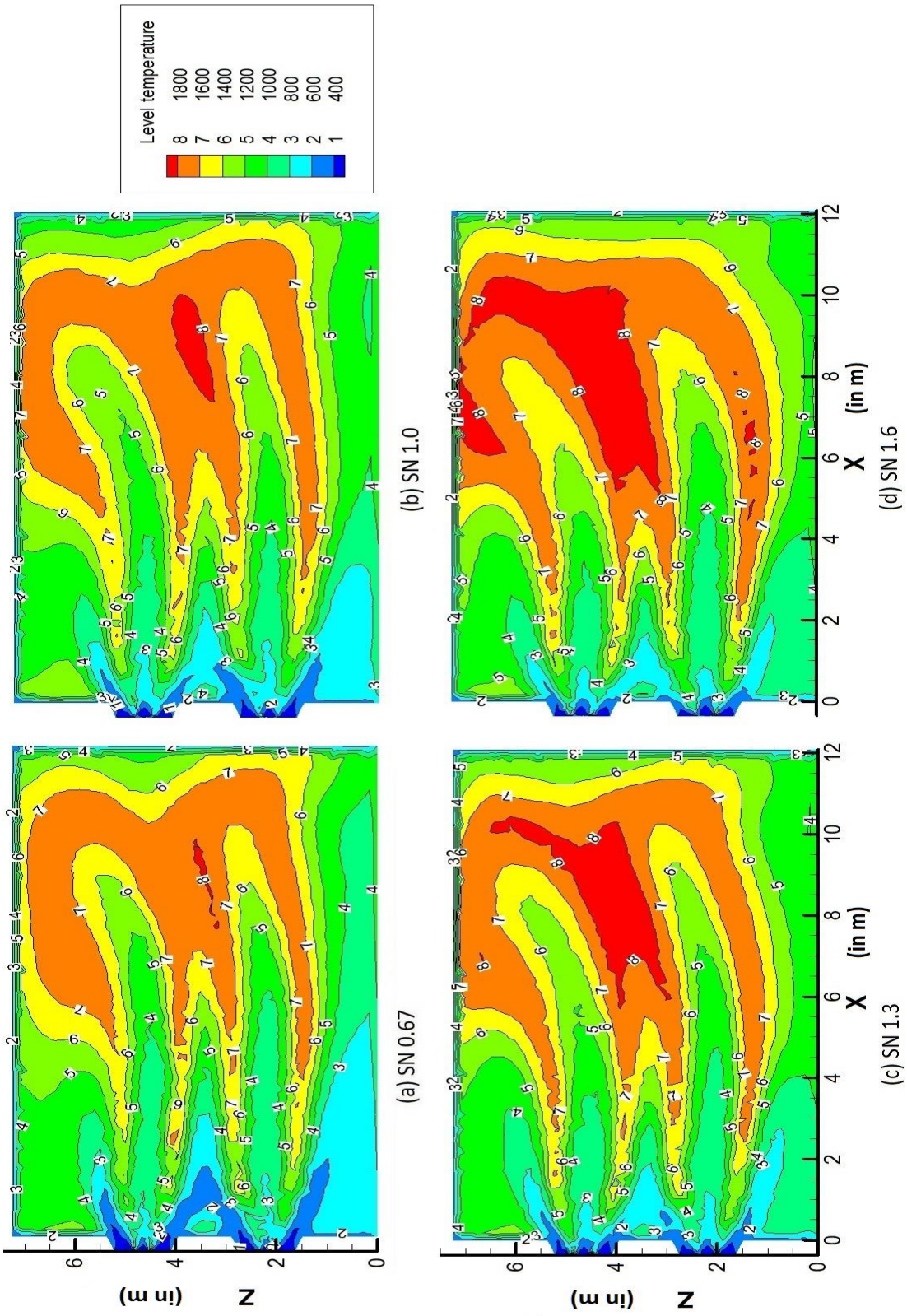

Figure 79. Temperature (K) contours for vertical pane at y=-2.24 m

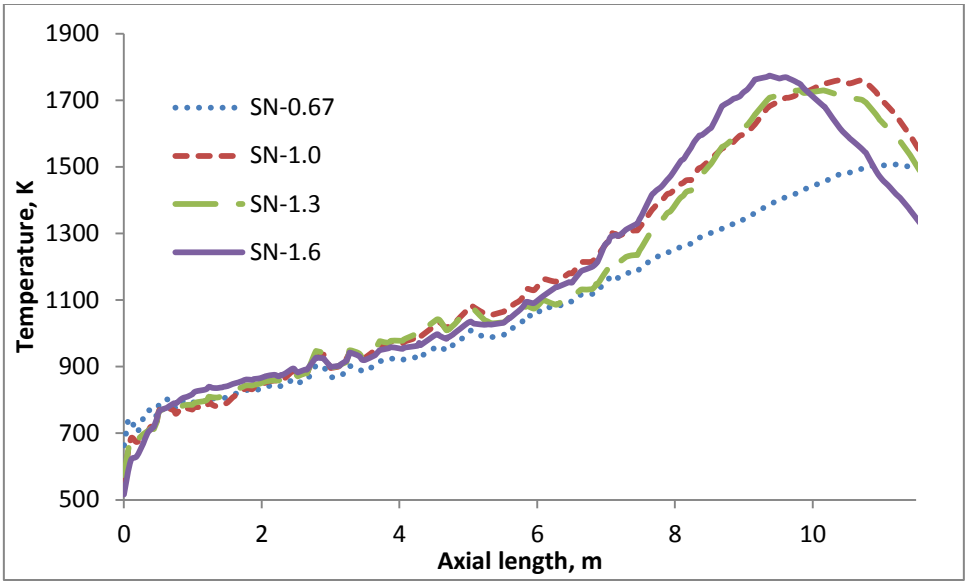

Figure 80. Temperature distribution along the axis of burner 1 (z=2.198 m)

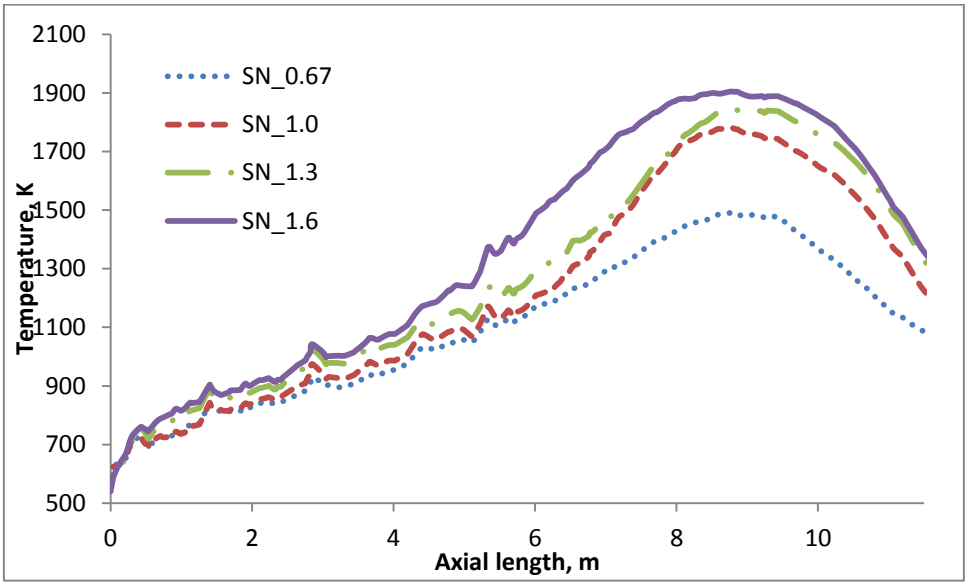

Figure 81. Temperature distribution along the axis of burner 2 (z=4.662 m)

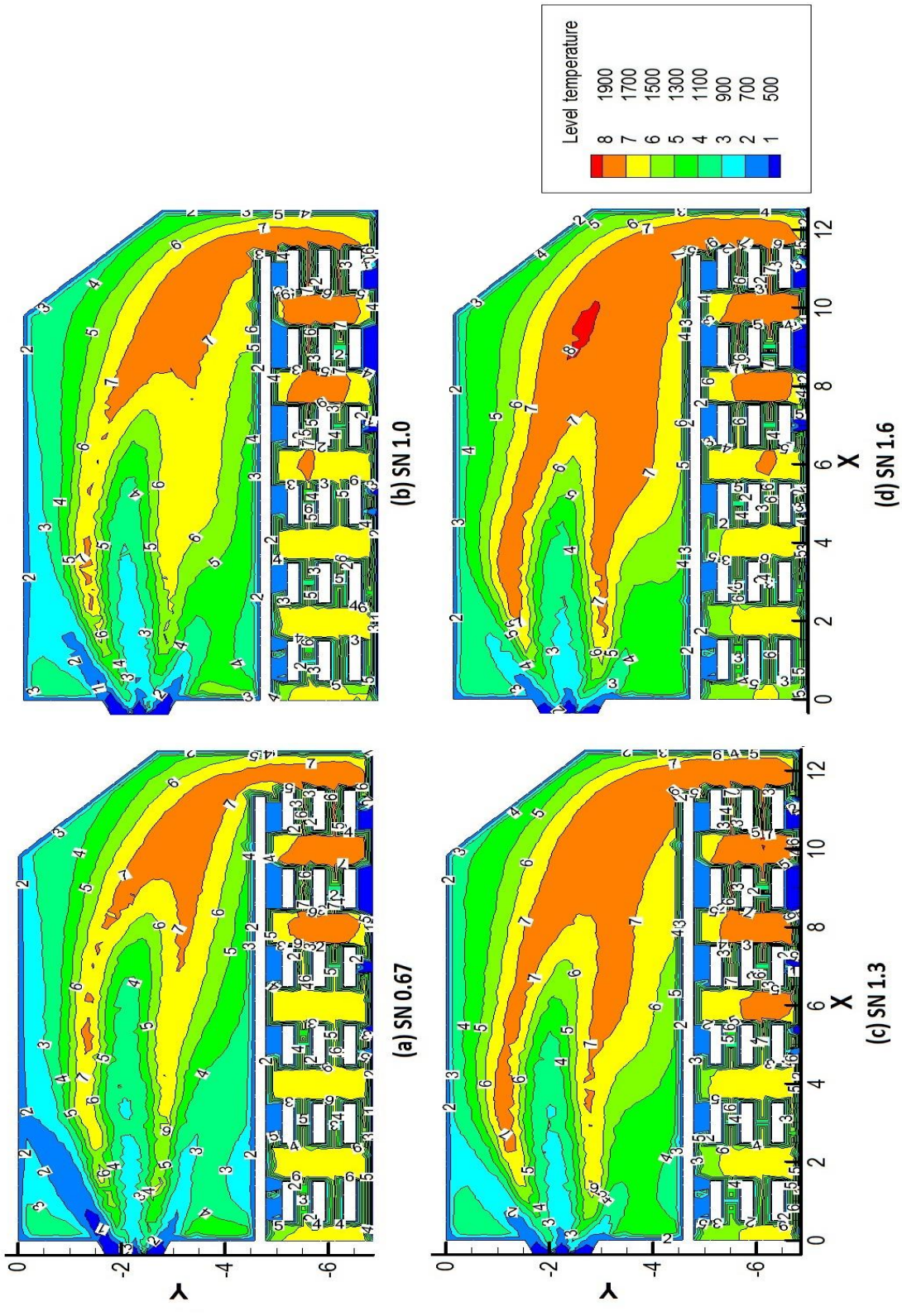

Figure 82. Temperature (K) contours for horizontal plane at z=4.662 m

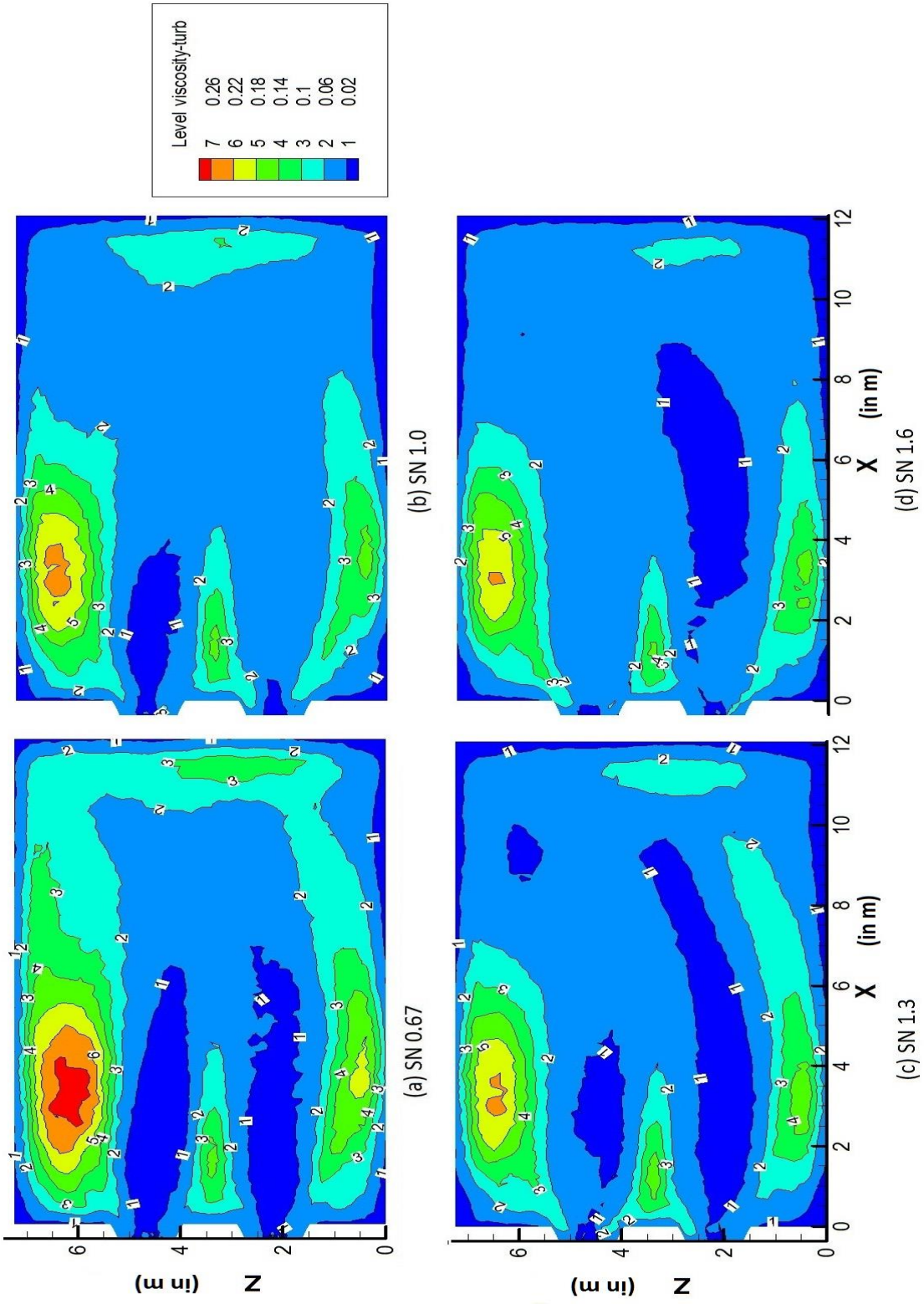

Figure 83. Turbulent viscosity (kg/m-s) contours for the vertical plane at y = 2.24 m

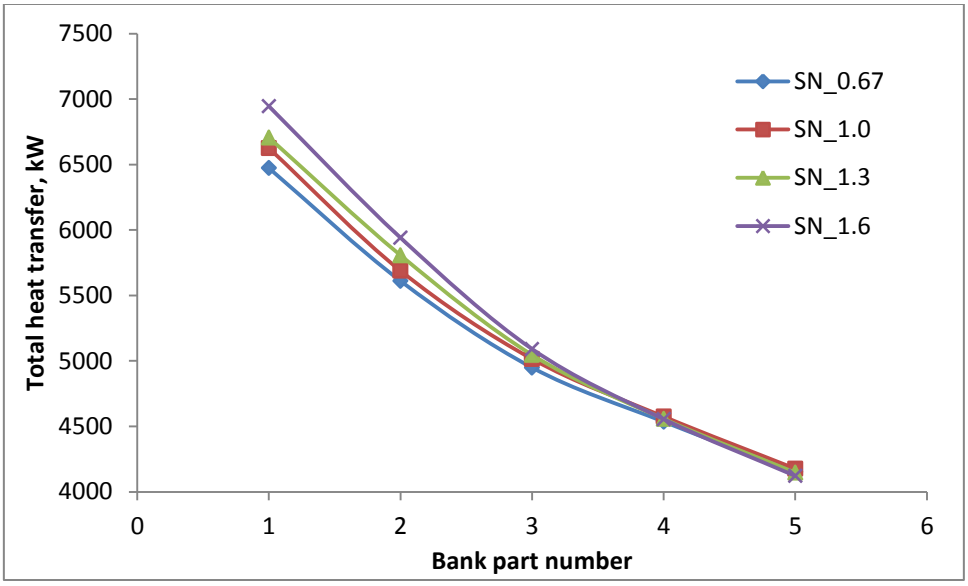

Figure 84. Distribution of total heat transfer rate (kW) along the boiler tube bank

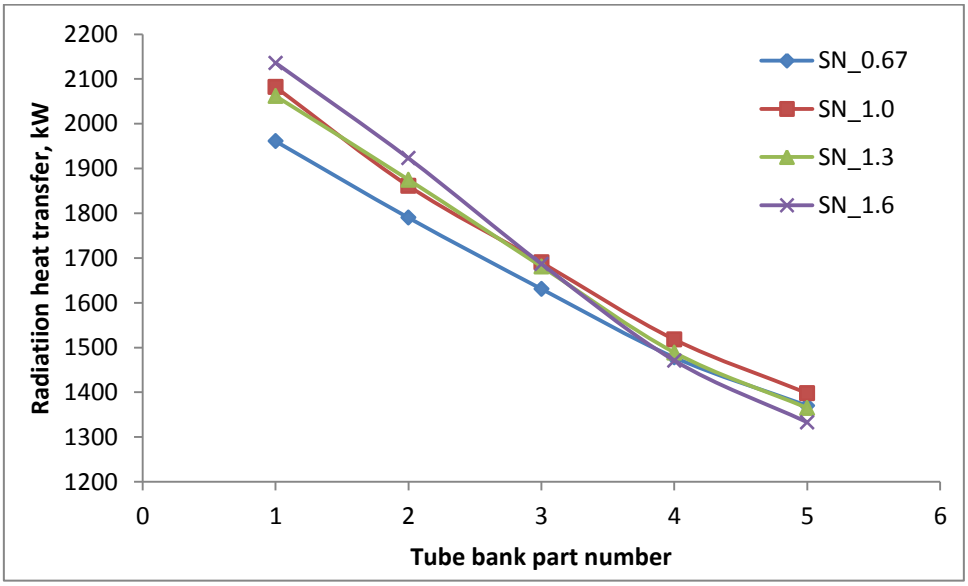

Figure 85. Distribution of radiation heat transfer rate (kW) along the boiler tube bank

CHAPTER 5

CONCLUSIONS AND RECOMMENDATIONS

In the present thesis work a computational fluid dynamics (CFD) model has been developed to predict the combustion characteristics of liquid fuel in oxygen-carbon dioxide environment. The numerical solution of the conservation of mass and momentum equations coupled with probability density function was used to predict the temperature, flow pattern and species distribution in the reactor. The model has been validated against the experimental results available in the literature and was found to be in good agreement with it. The model was extended to study the ethanol combustion characteristics in a 2-D vertical reactor and heavy fuel oil combustion in a 3-D boiler geometry.

5.1 Oxy-combustion of Ethanol in a Vertical Reactor

Combustion of ethanol in a 25 kW vertical reactor has been modelled numerically under different oxidizer environments including pure air, oxygen enriched air, OF21 (oxygen 21 % by volume and CO_2 79 % by volume) and OF29 (oxygen 29 % by volume and CO_2 71 % by volume). Realizable k-ε (RKE) model and Reynolds Stress Model (RSM) were employed to solve the turbulence and the results were compared. In addition to that, soot model was introduced and its effect on radiation and temperature levels were compared.

- It was found that RKE model is successful in predicting more accurate results for this case than RSM as there is no swirl involve.
- Replacement of N_2 by CO_2 in the oxidizer stream has significant effect on the flame shape and combustion characteristics.
- As the CO_2 percentage is increased in the environment, the temperature level falls because of high thermal capacity of CO_2 compared to N_2 as in case of OF21.
- OF29 case is much similar to pure air case yet reaction rate was found to be slower in the former case.
- Slower reaction rate and lower temperature levels were attributed to lower turbulent intensity and higher heat capacity of oxygen-carbon dioxide environment.
- Soot formation in ethanol combustion is negligible and soot model can satisfactorily be neglected without affecting the combustion results.

5.2 Liquid Fuel Oxy-combustion in the Furnace of a Water Tube Boiler

Oxy-combustion of liquid fuel has been modeled with two different percentages of carbon dioxide in the oxidizer stream and the results were compared with the pure air case. Effect of droplet size on the evaporation and combustion of the liquid were studied. OF29 case was extended to study the effect of swirl on the combustion characteristics.

- Introduction of CO_2 in the oxidizer stream affects flame characteristics, temperature level and heat transfer.

- OF21 case has lowest temperature level because of high carbon dioxide percentage in the oxidizer stream.
- Temperature level in OF29 case is similar to that of pure air case, however, combustion is delayed in carbon dioxide environment due lower turbulent intensity.
- For flames in carbon dioxide environment buoyancy effects are more prominent and temperature distribution is non-uniform in OF29 and OF21 cases.
- Soot formation is greatly suppressed by the presence of carbon dioxide in the combustion environment.
- Evaporation of the fuel is not the limiting factor in the reaction and hence effect of droplet size was not significant in the combustion.
- Swirl enhances the mixing of oxidizer with the fuel. It was found that increasing the swirl number from 0.67 to 1.6 significantly increases the combustion efficiency and temperature levels in the boiler.

5.3 Recommendations

Oxy-combustion is a promising carbon capturing technology, however, it is constrained by some disadvantages like longer flames, delayed ignition and lower flame temperature in the upstream region, non-uniform heat distribution and low convective heat transfer. Incorporation of oxy-combustion with Moderate or Intense Low-oxygen Dilution (MILD) technology can be an effective tool to overcome the disadvantages of oxy-combustion and increase the combustion efficiency. In the present work, multi-component nature of

the fuel has been neglected which means the fuel droplet was considered as composed of a single entity and an average of the properties of all the components has been considered. However, difference in volatility of the components can significantly affect the chemistry of reactions. Thus, a model considering the multi-component nature of the fuel should be employed to solve a more realistic problem.

NOMENCLATURE

A_p	Surface area of the particle
c	Heat capacity
$C_{i,D}$	Vapor concentration at the droplet surface
$C_{i,\infty}$	Vapor concentration in the bulk gas
f	Mixture fraction
g	Acceleration due to gravity
h	Heat transfer co-efficient
k	Turbulent dissipation
m	Mass
n	Refractive index
N_i	Molar flux of vapor
$p(f)$	Probably Density Function
s	Ratio of oxidizer mass to fuel mass
$\vec{s}$	Length scale
S	Source term
T	Temperature
T_∞	Local Temperature of the continuous phase
T_p	Droplet Temperature
$\overline{U}$	Velocity component

$\bar{u}$	Turbulent velocity component
u_p	Velocity of the droplet
Y	Mass fraction

Greek Symbols

ε	Turbulence kinetic energy
ε_p	Particle emissivity
θ_R	Radiation Temperature
κ_c	Mass transfer coefficient
μ_t	Turbulent viscosity
ρ	Density
σ	Stefan-Boltzman Constant

REFERENCES

[1] Solomon S., Qin D., Manning M., Chen Z., Marquis M., Averyt K. B., Miller H. L., and Tignor M., 2007, Climate Change 2007 - The Physical Science Basis: Working Group I Contribution to the Fourth Assessment Report of the IPCC, Cambridge University Press.

[2] Advancing the Science of Climate Change, National Research Council-2010.

[3] Commonwealth Scientific and Industrial Research Organization.

[4] Boden, T.A., G. Marland, and R.J. Andres. 2010. Global, Regional, and National Fossil-Fuel CO_2 Emissions. Carbon Dioxide Information Analysis Center, Oak Ridge National Laboratory, U.S. Department of Energy, Oak Ridge, Tenn., U.S.A. doi 10.3334/CDIAC/00001_V2010.

[5] Armor J. N., 2007, "Addressing the CO_2 dilemma," Catal. Letters, **114**(3-4), pp. 115–121.

[6] Lupion M., Diego R., Loubeau L., and Navarrete B., 2011, "CIUDEN CCS Project: Status of the CO_2 capture technology development plant in power generation," Energy Procedia, **4**, pp. 5639–5646.

[7] Wall T. F., 2007, "Combustion processes for carbon capture," Proc. Combust. Inst., **31**(1), pp. 31–47.

[8] Simpson A. P., and Simon A. J., 2007, "Second law comparison of oxy-fuel combustion and post-combustion carbon dioxide separation," Energy Convers. Manag., **48**, pp. 3034–45.

[9] Eide L., and Bailey D., 2005, "Pre-combustion decarbonisation process," Oil gas Sci. Technol., **60**, pp. 475–484.

[10] "http://www.globalccsinstitute.com/."

[11] Dyer P., Richards R., Russek S., and Taylor D., 2000, "Ion transport membrane technology for oxygen separation and syngas production," Solid State Ionics, **134**, pp. 21–33.

[12] Zhang N., and Lior N., 2008, "Two novel oxy-fuel power cycles integrated with natural gas reforming and CO 2 capture," Energy, **33**(2), pp. 340–351.

[13] Bailey D., and Feron P., 2005, "Post-combustion Decarbonisation Process," Oil gas Sci. Technol., **60**, pp. 461–474.

[14] Rubin E., Meyer L., and Coninck H., 2005, Carbon Dioxide Capture and Storage, Technical Summary.

[15] Singh D., Croiset E., Douglas P., and Douglas M., 2003, "Techno-economic study of CO_2 capture from an existing coal-fired power plant: MEA scrubbing vs. O2/CO_2 recycle combustion," Energy Convers. Manag., **44**, pp. 3073–3091.

[16] Li J.-R., Ma Y., McCarthy M. C., Sculley J., Yu J., Jeong H.-K., Balbuena P. B., and Zhou H.-C., 2011, "Carbon dioxide capture-related gas adsorption and separation in metal-organic frameworks," Coord. Chem. Rev., **255**(15-16), pp. 1791–1823.

[17] Li T., Nishida K., and Hiroyasu H., 2011, "Droplet size distribution and evaporation characteristics of fuel spray by a swirl type atomizer," Fuel, **90**(7), pp. 2367–2376.

[18] Ghassemi H., Baek S. W., and Khan Q. S., 2006, "Experimental Study on Evaporation of Kerosene Droplets At Elevated Pressures and Temperatures," Combust. Sci. Technol., **178**(9), pp. 1669–1684.

[19] Negeed E.-S. R., Ishihara N., Tagashira K., Hidaka S., Kohno M., and Takata Y., 2010, "Experimental study on the effect of surface conditions on evaporation of sprayed liquid droplet," Int. J. Therm. Sci., **49**(12), pp. 2250–2271.

[20] Abramzon B., and Sirignano W., 1989, "Droplet vaporization model for spray combustion calculations," Int. J. Heat Mass Transf., **32**(9), pp. 1605–1618.

[21] Daıf A., Bouaziz M., Chesneau X., and Chérif A. A., 1998, "Comparison of multicomponent fuel droplet vaporization experiments in forced convection with the Sirignano model," Exp. Therm. Fluid Sci., **18**, pp. 282–290.

[22] Kitano T., Nishio J., Kurose R., and Komori S., 2014, "Evaporation and combustion of multicomponent fuel droplets," Fuel, **136**, pp. 219–225.

[23] Mohd Yasin M. F., Cant R. S., Chong C. T., and Hochgreb S., 2014, "Discrete multicomponent model for biodiesel spray combustion simulation," Fuel, **126**, pp. 44–54.

[24] Bhattacharya P., Ghosal S., and Som S. K., 1996, "Evaporation of multicomponent liquid fuel droplets," Int. J. Energy Res., **20**(May 1994), pp. 385–398.

[25] Gogos G., Soh S., and Pope D. N., 2003, "Effects of gravity and ambient pressure on liquid fuel droplet evaporation," Int. J. Heat Mass Transf., **46**(2), pp. 283–296.

[26] Kamal M. M., and Mohamad A. A., 2007, "Investigation of liquid fuel combustion in a cross-flow burner," Proc. Inst. Mech. Eng. Part A J. Power Energy, **221**(3), pp. 371–385.

[27] Seiser R., Humer S., Seshadri K., and Pucher E., 2007, "Experimental investigation of methanol and ethanol flames in nonuniform flows," Proc. Combustion Institute, **31**(1), pp. 1173–1180.

[28] Yang F., Li J., Zhou Z., Zhang X., and Wang N., 2013, "Experimental Research On Combustion Characteristics Of Liquid Fuel In Straight Tubes," Cleaner Combustion and Sustainable World, Springer Berlin Heidelberg, pp. 245–251.

[29] Lacas F., Leroux B., and Darabiha N., 2005, "Experimental study of air dilution in oxy-liquid fuel flames," Proc. Combust. Inst., **30**(2), pp. 2037–2045.

[30] Heyes A. L., Jelercic D., and Whitelaw J. H., 1998, "Experiments in a small gas-turbine combustor with gas and liquid fuels," RTO MP, **14**(October), pp. 12–16.

[31] Nejati V., Khazraii Y., Daneshvar K., and Khazraii S., 2011, "Experimantal and numerical simulation on NOx emission in Liquid fuel spray flames," Chia Laguna, Cagliari, Sardinia, Italy, September 11-15.

[32] Eisazadeh-Far K., Moghaddas A., Al-Mulki J., and Metghalchi H., 2011, "Laminar burning speeds of ethanol/air/diluent mixtures," Proc. Combust. Inst., **33**(1), pp. 1021–1027.

[33] Askari O., Metghalchi H., Kazemzadeh Hannani S., Moghaddas A., Ebrahimi R., and Hemmati H., 2012, "Fundamental Study of Spray and Partially Premixed Combustion of Methane/Air Mixture," J. Energy Resour. Technol., **135(**2), p. 021001.

[34] Barajas P. E., Parthasarathy R. N., and Gollahalli S. R., 2012, "Combustion Characteristics of Biofuels in Porous-Media Burners at an Equivalence Ratio of 0.8," J. Energy Resour. Technol., **134**(2), p. 021004.

[35] Greenberg J., 2007, "Finite-rate evaporation and droplet drag effects in spherical flame front propagation through a liquid fuel mist," Combust. Flame, **148**(4), pp. 187–197.

[36] Patel N., and Menon S., 2008, "Simulation of spray–turbulence–flame interactions in a lean direct injection combustor," Combust. Flame, **153**(1-2), pp. 228–257.

[37] Okasha F., 2007, "Modeling of liquid fuel combustion in fluidized bed," Fuel, **86**(15), pp. 2241–2253.

[38] Pang K. M., Ng H. K., and Gan S., 2011, "Development of an integrated reduced fuel oxidation and soot precursor formation mechanism for CFD simulations of diesel combustion," Fuel, **90**(9), pp. 2902–2914.

[39] Wang F., Hu B., and Huang Y., 2013, "A two-phase turbulent combustion model and its validation for spray flames," Fuel, **113**, pp. 280–286.

[40] Saario A., Rebola A., Coelho P. J., Costa M., and Oksanen A., 2005, "Heavy fuel oil combustion in a cylindrical laboratory furnace: measurements and modeling," Fuel, **84**(4), pp. 359–369.

[41] Eaton A. M., Smoot L. D., Hill S. C., and Eatough C. N., 1999, "Components, formulations, solutions, evaluation, and application of comprehensive combustion models," Prog. Energy Combust. Sci., **25**(4), pp. 387–436.

[42] Rohani B., Wahid M. a., Sies M. M., and Saqr K. M., 2012, "Comparison of eddy dissipation model and presumed probability density function model for temperature prediction in a non-premixed turbulent methane flame," AIP Conf. Proc., **1440**, pp. 384–391.

[43] Ilamathi P., Selladurai V., and Balamurugan K., 2013, "Modeling and Optimization of Unburned Carbon in Coal-Fired Boiler Using Artificial Neural Network and Genetic Algorithm," J. Energy Resour. Technol., **135**(3), p. 032201.

[44] Habib M. A., Ben-Mansour R., Badr H. M., Ahmed S. F., and Ghoniem A. F., 2012, "Computational fluid dynamic simulation of oxyfuel combustion in gas-fired water tube boilers," Comput. Fluids, **56**, pp. 152–165.

[45] Croiset E., and Thambimuthu K. V., 2001, "NOx and SO_2 emissions from O_2/CO_2 recycle coal combustion," Fuel, **80**(14), pp. 2117–2121.

[46] Andersson K., and Johnsson F., 2007, "Flame and radiation characteristics of gas-fired O_2/CO_2 combustion," Fuel, **86**(5-6), pp. 656–668.

[47] Park S., Kim T., Sohn J., and Lee Y., 2011, "An integrated power generation system combining solid oxide fuel cell and oxy-fuel combustion for high performance and CO_2 capture," Appl. Energy, **88**(4), pp. 1187–1196.

[48] Habib M. A., Nemitallah M., and Ben-Mansour R., 2013, "Recent Development in Oxy-Combustion Technology and Its Applications to Gas Turbine Combustors and ITM Reactors," Energy & Fuels, **27**(1), pp. 2–19.

[49] Liu F., Guo H., and Smallwood G. J., 2003, "The chemical effect of CO_2 replacement of N_2 in air on the burning velocity of CH_4 and H_2 premixed flames," Combust. Flame, **133**(4), pp. 495–497.

[50] Andersson K., Johansson R., Johnsson F., and Leckner B., 2008, "Radiation Intensity of Propane-Fired Oxy-Fuel Flames: Implications for Soot Formation," Energy & Fuels, **22**(3), pp. 1535–1541.

[51] Van Blarigan A., Kozarac D., Seiser R., Cattolica R., Chen J.-Y., and Dibble R., 2013, "Experimental Study of Methane Fuel Oxycombustion in a Spark-Ignited Engine," J. Energy Resour. Technol., **136**(1), p. 012203.

[52] Quesito F., Santarelli M., Leone P., and Aggarwal S. K., 2013, "Biogas Combustion in Premixed Flames or Electrochemical Oxidation in SOFC: Exergy and Emission Comparison," J. Energy Resour. Technol., **135**(2), p. 021201.

[53] Abdul-Sater H., and Krishnamoorthy G., 2013, "An assessment of radiation modeling strategies in simulations of laminar to transitional, oxy-methane, diffusion flames," Appl. Therm. Eng., **61**(2), pp. 507–518.

[54] Krishnamoorthy G., 2013, "A new weighted-sum-of-gray-gases model for oxy-combustion scenarios," International Journal of Energy Research, 37 pp. 1752–1763.

[55] Yin C., Johansen L. C. R., Rosendahl L. a., and Kær S. K., 2010, "New Weighted Sum of Gray Gases Model Applicable to Computational Fluid Dynamics (CFD) Modeling of Oxy−Fuel Combustion: Derivation, Validation, and Implementation," Energy & Fuels, **24**(12), pp. 6275–6282.

[56] Johansson R., Andersson K., Leckner B., and Thunman H., 2010, "Models for gaseous radiative heat transfer applied to oxy-fuel conditions in boilers," Int. J. Heat Mass Transf., **53**(1-3), pp. 220–230.

[57] Kangwanpongpan T., França F. H. R., Corrêa da Silva R., Schneider P. S., and Krautz H. J., 2012, "New correlations for the weighted-sum-of-gray-gases model in oxy-fuel conditions based on HITEMP 2010 database," Int. J. Heat Mass Transf., **55**(25-26), pp. 7419–7433.

[58] Yin C., 2012, "Nongray-Gas Effects in Modeling of Large-Scale Oxy−Fuel Combustion Processes."

[59] Nakod P., Krishnamoorthy G., Sami M., and Orsino S., 2013, "A comparative evaluation of gray and non-gray radiation modeling strategies in oxy-coal combustion simulations," Appl. Therm. Eng., **54**(2), pp. 422–432.

[60] Kangwanpongpan T., Corrêa da Silva R., and Krautz H. J., 2012, "Prediction of oxy-coal combustion through an optimized weighted sum of gray gases model," Energy, **41**(1), pp. 244–251.

[61] Hjartstam S., Johansson R., Andersson K., and Johnsson F., 2012, "Computational Fluid Dynamics Modeling of Oxy-Fuel Flames: The Role of Soot and Gas Radiation."

[62] P. Edge, S.R. Gubba, L. Ma, R. Porter, M. Pourkashanian A. W., 2011, "LES modelling of air and oxy-fuel pulverised coal combustion-impact on flame properties," Proc. Combust. Inst., **33**, pp. 2709–2716.

[63] Becher V., Bohn J.-P., Dias P., and Spliethoff H., 2011, "Validation of spectral gas radiation models under oxyfuel conditions—Part B: Natural gas flame experiments," Int. J. Greenh. Gas Control, **5**, pp. S66–S75.

[64] Chen L., Yong S. Z., and Ghoniem A. F., 2012, "Oxy-fuel combustion of pulverized coal: Characterization, fundamentals, stabilization and CFD modeling," Prog. Energy Combust. Sci., **38**(2), pp. 156–214.

[65] Nozaki T., Takano S., and Kiga T., 1997, "Analysis of the flame formed during oxidation of pulverized coal by an O_2-CO_2 mixture," Energy, **22**(2), pp. 199–205.

[66] Kimura N., Omata K., Kjga T., Takano S., and Shikisima S., 1995, "The characteristics of pulverized coal combustion in O_2/CO_2 mixtures for CO_2 recovery" Energy Conversion and Management, **36**(6), pp. 805–808.

[67] Suda T., Masuko K., Sato J., Yamamoto A., and Okazaki K., 2007, "Effect of carbon dioxide on flame propagation of pulverized coal clouds in CO_2/O_2 combustion," Fuel, **86**(12-13), pp. 2008–2015.

[68] Li P., Dally B. B., Mi J., and Wang F., 2013, "MILD oxy-combustion of gaseous fuels in a laboratory-scale furnace," Combust. Flame, **160**(5), pp. 933–946.

[69] Blasiak W., Yang W. H., Narayanan K., and von Schéele J., 2007, "Flameless oxyfuel combustion for fuel consumption and nitrogen oxides emissions reductions and productivity increase," J. Energy Inst., **80**(1), pp. 3–11.

[70] Krishnamurthy N., Paul P. J., and Blasiak W., 2009, "Studies on low-intensity oxy-fuel burner," Proc. Combust. Inst., **32**(2), pp. 3139–3146.

[71] Veynante D., and Vervisch L., 2002, "Turbulent combustion modeling," Prog. Energy Combust. Sci., **28**(3), pp. 193–266.

[72] Versteeg H. K., and Malasekara W., 1995, An introduction to computational fluid dynamics, the finite volume method, Longman Group Ltd, Essex.

[73] Chen L., and Ghoniem A. F., 2012, "Simulation of Oxy-Coal Combustion in a 100 kW th Test Facility Using RANS and LES: A Validation Study," Energy & Fuels, **26**(8), pp. 4783–4798.

[74] Bonefačić I., Blecich P., and Wolf I., 2011, "Thermodynamic analysis of heat and mass transfer in the combustion chamber of an industrial furnace," Stroj. časopis za Teor. i praksu u, **53**(3), pp. 179–189.

[75] 2010, Ansys Fluent Theory Guide, Ansys Inc., Canonsburg.

[76] Morsi S. a., and Alexander a. J., 2006, "An investigation of particle trajectories in two-phase flow systems," J. Fluid Mech., **55**(02), p. 193.

[77] Ranz W., and Marshall W., 1952, "Evaporation from drops," Chem. Eng. Prog, **48**(3), pp. 141–146.

[78] Magnussen B. F. F., and Hjertager B. H. H., 1977, "On mathematical modeling of turbulent combustion with special emphasis on soot formation and combustion," Symp. Combust., **16**(1), pp. 719–729.

[79] Nemitallah M. A., and Habib M. A., 2013, "Experimental and numerical investigations of an atmospheric diffusion oxy-combustion flame in a gas turbine model combustor," Appl. Energy, **111**, pp. 401–415.

[80] Shih T.-H., Liou W. W., Shabbir A., Yang Z., and Zhu J., 1995, "A new k-ϵ eddy viscosity model for high reynolds number turbulent flows," Comput. Fluids, **24**(3), pp. 227–238.

[81] Kazakov A., Dryer F. L., and Manzello S. L., 2003, "Ethanol Droplet Combustion at Elevated Pressures and Enhanced oxygen," American Institute of Aeronautics and Astronautics (AIAA) Aerospace Sciences Meeting and Exhibit, pp. 1–7.

VITAE

Name	:	Binash Imteyaz
Nationality	:	Indian
Date of Birth	:	02-Feb-1990
Email	:	binash_ahmad@.yahoo.co.in
		binashahmad@kfupm.edu.sa
Address	:	202-Manjushree Aptt. - C,
		Near PNB, Bank Road,
		Patna, Bihar, India.
Academic background	:	Master of Science (M.S.) Dec, 2014
		Mechanical Engineering Department
		King Fahd University of Petroleum & Minerals,
		Dhahran, Saudi Arabia.
		Bachelors of Engineering (B.E.) Dec, 2012
		Production Engineering Department,
		Birla Institute of Technology, Mesra,
		Ranchi, India.

Papers :

1. Study of Combustion Characteristics of Ethanol at Different Dilution With the Carrier Gas, J. Energy Resour. Technol., 137(3), p. 032205.

2. Performance of Spark Ignition Engine using Gasoline-91 and Gasoline-95. International Journal of Innovative Science, Engineering & Technology, 1(6), 464–469
3. Investigation of Liquid Ethanol Evaporation and Combustion in Air and Oxygen Environments Inside a 25 kW Vertical Reactor" – submitted – Journal of Power and Energy
4. The Characteristics of Oxy-combustion of Liquid Fuel in a Typical Water-tube Boiler" – Submitted -- Fuel